Remote sensing of the terrestrial carbon cycle: A review of advances over 50 years

Jingfeng Xiao, Frédéric Chevallier, Cécile Gomez, Luis Guanter, Jeffrey A. Hicke, Alfredo R. Huete, Kazuhito Ichii, Wenjian Ni, Yong Pang, Abdullah F. Rahman, et al.

Remote sensing of the terrestrial carbon cycle: A review on 50 years of advances

Jingfeng Xiao[1*], Frederic Chevallier[2], Cecile Gomez[3], Luis Guanter[4], Jeffrey A. Hicke[5], Alfredo R. Huete[6], Kazuhito Ichii[7], Wenjian Ni[8], Yong Pang[9], Abdullah F. Rahman[10], Guoqing Sun[11], Wenping Yuan[12], Li Zhang[13], Xiaoyang Zhang[14]

[1]Earth Systems Research Center, Institute for the Study of Earth, Oceans, and Space, University of New Hampshire, Durham, NH 03824, USA; [2]Laboratoire des Sciences du Climat et de l'Environnement, CEA, CNRS, UVSQ/ IPSL, Université Paris-Saclay, France ; [3]LISAH, Univ Montpellier, IRD, INRA, SupAgro, F-34060 Montpellier, France; [4]Centro de Tecnologías Físicas, Universitat Politècnica de València, Camí de Vera s/n, 46022 València, Spain; [5]Department of Geography, University of Idaho, Moscow, ID 83844, USA; [6]Climate Change Cluster, University of Technology Sydney, NSW 2007, Australia; [7]Center for Environmental Remote Sensing, Chiba University, Chiba, Japan; [8]State Key Laboratory of Remote Sensing Science, Institute of Remote Sensing and Digital Earth, Chinese Academy of Sciences, Beijing 100094, China; [9]Institute of Forest Resource Information Technique, Chinese Academy of Forestry, Beijing 100091, China; [10]Coastal Studies Lab, University of Texas Rio Grande Valley, TX 78597, USA; [11]Department of Geographical Sciences, University of Maryland, College Park, MD 20740, USA; [12]School of Atmospheric Sciences, Sun Yat-Sen University, Guangzhou 519082, China; [13]Key Laboratory of Digital Earth Science, Institute of Remote Sensing and Digital Earth (RADI),Chinese Academy of Sciences, Beijing 100094, China; [14]Geospatial Sciences Center of Excellence, South Dakota State University, Brookings, SD 57007, USA

[*]Corresponding author: j.xiao@unh.edu

Abstract Quantifying ecosystem carbon fluxes and stocks is essential for better understanding the global carbon cycle and improving projections of the carbon-climate feedbacks. Remote sensing has played a vital role in this endeavor during the last five decades by quantifying carbon fluxes and stocks. The availability of satellite observations of the land surface since the 1970s, particularly the early 1980s, has made it feasible to quantify ecosystem carbon fluxes and stocks at regional to global scales. Here we provide a review of the advances in remote sensing of the terrestrial carbon cycle from the early 1970s to present. First, we present an overview of the terrestrial carbon cycle and remote sensing of carbon fluxes and stocks. Remote sensing data acquired in a broad wavelength range (visible, infrared, and microwave) of the electromagnetic spectrum have been used to estimate carbon fluxes and/or stocks. Second, we provide a historical overview of the key milestones in remote sensing of the terrestrial carbon cycle. Third, we review the platforms/sensors, methods, findings, and challenges in remote sensing of carbon fluxes. The remote sensing data and techniques used to quantify carbon fluxes include vegetation indices, light use efficiency models, terrestrial biosphere models, data-driven (or machine learning) approaches, solar-induced chlorophyll fluorescence, land surface temperature, and atmospheric inversions. Fourth, we review the platforms/sensors, methods, findings, and challenges in passive optical, microwave, and lidar remote sensing of biomass carbon stocks as well as remote sensing of carbon stocks in soils. Fifth, we review the progresses in remote sensing of disturbance impacts on the carbon cycle. Sixth, we also discuss the uncertainty and validation of the resulting carbon flux and stock estimates. Finally, we offer a forward-looking perspective and insights for future research and directions in remote sensing of the terrestrial carbon cycle. Remote sensing is anticipated to play an increasingly important role in carbon cycling studies in the future. This comprehensive and insightful review on 50 years of remote

sensing of the terrestrial carbon cycle is timely and valuable and can benefit scientists in various research communities (e.g., carbon cycle, remote sensing, climate change, ecology) and inform ecosystem and carbon management, carbon-climate projections, and climate policymaking.

Keywords: Carbon fluxes; carbon stocks; optical remote sensing; microwave remote sensing; lidar; aboveground biomass; soil organic carbon; solar-induced chlorophyll fluorescence; terrestrial ecosystems; Landsat; AVHRR; MODIS; Sentinel; OCO-2; Synthetic Aperture Radar; carbon cycling; vegetation indices; light use efficiency; disturbance; carbon-climate feedbacks

1. Introduction

Terrestrial ecosystems "breathe" in carbon dioxide (CO_2) through photosynthesis and release carbon (C) into the atmosphere through respiration and therefore play an important role in the global C cycle and the Earth's climate (Schimel 1995). The terrestrial C cycle has received tremendous attention from the research community during the last several decades. Remote sensing has been widely used to study the terrestrial C cycle by quantifying ecosystem C fluxes and stocks (e.g., Running et al. 2004; Saatchi et al. 2011), examining the impacts of global change on C dynamics (e.g., Nemani et al. 2003; Smith et al. 2016; Li et al. 2018a), and the feedbacks to the climate (e.g., Ollinger et al. 2008; Xiao 2014). The availability of satellite observations of the land surface since the 1970s, particularly from the early 1980s, has made it feasible to assess the magnitude, spatial patterns, interannual variability, and long-term trends of ecosystem C dynamics at landscape, regional, and global scales.

Ecosystem C fluxes have been widely measured or quantified using remotely sensed data. For example, satellite-derived vegetation indices (VIs) (e.g., normalized difference vegetation index or NDVI, enhanced vegetation index or EVI) are traditionally used to approximate or

70 estimate gross primary production (GPP) directly (e.g., Zhou et al. 2001; Xiao and Moody 2004;
71 Rahman et al. 2005), and are also used in light use efficiency (LUE) models for quantifying GPP
72 and net primary production (NPP) (Potter et al. 1993; Running et al. 2004). The recent advent of
73 solar-induced chlorophyll fluorescence (SIF) has offered an innovative and independent
74 approach for estimating GPP (Frankenberg et al. 2011; Joiner et al. 2011; Li et al. 2018b). In
75 addition, satellite-derived land surface temperature (LST) has also been used to quantify
76 ecosystem respiration (ER) (e.g., Rahman et al. 2005). Moreover, the measurement of
77 atmospheric column CO_2 concentrations from the Greenhouse gases Observing SATellite
78 (GOSAT) and the Orbiting Carbon Observatory-2 (OCO-2) allows the estimation of net biome
79 production (NBP) (Kondo et al. 2015). Besides directly measuring C fluxes, remote sensing has
80 also been used to estimate leaf area index (LAI) that is in turn used to prescribe LAI in
81 diagnostic ecosystem models (Liu et al. 2018b) or to be assimilated into prognostic models
82 (Hazarika et al. 2005) for simulating ecosystem C fluxes.

83 Both optical and microwave remote sensing data have been widely used to quantify and
84 monitor C stocks during the last few decades. For example, surface reflectance and VIs derived
85 from optical sensors have been used to quantify biomass using empirical models (Myneni et al.
86 2001), allometric equations (Zhang and Kondragunta 2006), or machine learning approaches
87 (John et al. 2018). Active microwave remote sensing has also been traditionally used to estimate
88 biomass (Le Toan et al. 1992; Ni et al. 2016). Lidar (light detection and ranging) has emerged as
89 an effective technique for quantifying aboveground biomass (AGB) for forests and other
90 ecosystems and has been increasingly used over the last two decades (Lefsky et al. 1999; Lefsky
91 et al. 2005). Besides biomass C stocks, soil organic C (SOC) has also been estimated using

remotely sensed data using empirical or machine learning approaches (Gomez et al. 2008; Mishra et al. 2010; Chen, Chang, Xiao et al. 2019).

During the last five decades, a number of airborne and satellite sensors have observed the Earth's land surface, and a wide variety of techniques have been developed to quantify C fluxes and stocks using remotely sensed data. Several previous studies have reviewed the remote sensing of C fluxes or stocks (e.g., Roughgarden et al. 1991; Hilker et al. 2008; Ladoni et al. 2010; Goetz and Dubayah 2011; Schimel et al. 2015; Ryu et al. 2019; Mohammed et al. 2019). For example, Hilker et al. (2008) reviewed the status and future directions of simulating GPP via the use of remote sensing in LUE models. Turner et al. (2004) reviewed the integration of remotely sensed data (e.g., vegetation type, stand age, biomass, phenology, LAI, and tree height) with ecosystem process models for regional assessment of C fluxes. Ladoni et al. (2010) reviewed the potential and limitations of remotely sensed data for mapping SOC. Despite these review and overview efforts, to our knowledge, no study has systematically reviewed the remote sensing of the terrestrial C cycle over the last 50 years. Moreover, the last decade has witnessed more rapid advances in remote sensing and its extensive use for quantifying C fluxes and stocks. A comprehensive review on the history and advances in remote sensing of the terrestrial C cycle will be timely and useful.

Here we provide a review on 50 years of advances in remote sensing of the terrestrial C cycle. We conducted a comprehensive review of the achievements, challenges, and opportunities of remote sensing science and technology in terrestrial C cycle studies from the 1970s to present. Section 2 presents an overview of the terrestrial C cycle and remote sensing of C fluxes and stocks based on a broad wavelength region (visible, infrared, and microwave) on the electromagnetic spectrum. In Section 3, we provide a historical overview of the main milestones

115 in remote sensing of the terrestrial C cycle. In Section 4, we review the platforms/sensors,
116 methods, achievements, and challenges for quantifying ecosystem C fluxes. The remotely sensed
117 data and techniques used for quantifying C fluxes include vegetation indices, LUE models,
118 terrestrial biosphere models, data-driven (or machine learning) approaches, SIF, LST, and
119 atmospheric inversions. In Section 5, we review the platforms/sensors, methods, achievements,
120 and challenges in passive optical, microwave, and lidar remote sensing of biomass C stocks and
121 also in remote sensing of C stocks in soils. In Section 6, we review the methods and challenges
122 for assessing the impacts of disturbances on the terrestrial C cycle. In Section 7, we discuss the
123 uncertainty and validation of the resulting C fluxes and stock estimates. Finally, we offer a
124 forward looking perspective and insights for future research and directions in the terrestrial C
125 cycle area of environmental remote sensing in Section 8.
126

127 **2. Overview of the terrestrial carbon cycle and remote sensing**

128 The terrestrial C cycle encompasses the exchange of C among the terrestrial biosphere,
129 pedosphere, geosphere, and atmosphere of the Earth. Plants absorb C from the atmosphere
130 through photosynthesis and store the C in biomass (leaves, branches, trunks, and roots). GPP, the
131 amount of C fixed by terrestrial ecosystems through photosynthesis, constitutes the largest C flux
132 between the terrestrial biosphere and the atmosphere. GPP is the basis for the production of food,
133 wood, and fiber, and therefore has important implications for human welfare. A part of the C
134 absorbed is returned to the atmosphere through plant respiration (i.e., autotrophic respiration),
135 and the difference between GPP and autotrophic respiration is termed as NPP. Litterfall, plant
136 materials that fall to the ground (leaves, branches, flowers, and fruits), contributes to the buildup
137 of the soil C pool. The C input from litterfall and root mortality/exudation and the C release from

decomposition (i.e., heterotrophic respiration) determine the size of the SOC pool (Liu et al. 2011). GPP along with ER, the sum of autotrophic and heterotrophic respiration, determine the net ecosystem production (NEP). Other processes such as deforestation, harvest, and fire can also lead to the loss of C, and the net ecosystem C balance is NBP. Disturbances are critical ecosystem processes that influence C cycle dynamics. Direct emissions from one disturbance type, wildfire, transfer C from ecosystems to the atmosphere immediately (while burning). Major impacts to GPP and respiration can occur following fires as well as other disturbance types, which include natural disturbances (insect and disease outbreaks, drought, and severe storms) and harvesting, and these impacts can last for decades as ecosystems recover (Odum 1969). The C fluxes and stocks that are quantified using remote sensing data and methods are illustrated in **Figure 1**. Better understanding the terrestrial C cycle has important implications for climate projections. Remote sensing has played a critical role in quantifying C fluxes (e.g., GPP, NPP, ER, NEP, NBP) (Running et al. 2004; Xiao et al. 2011a) and stocks (biomass and SOC) (Saatchi et al. 2011) at various spatial and temporal scales during the last five decades.

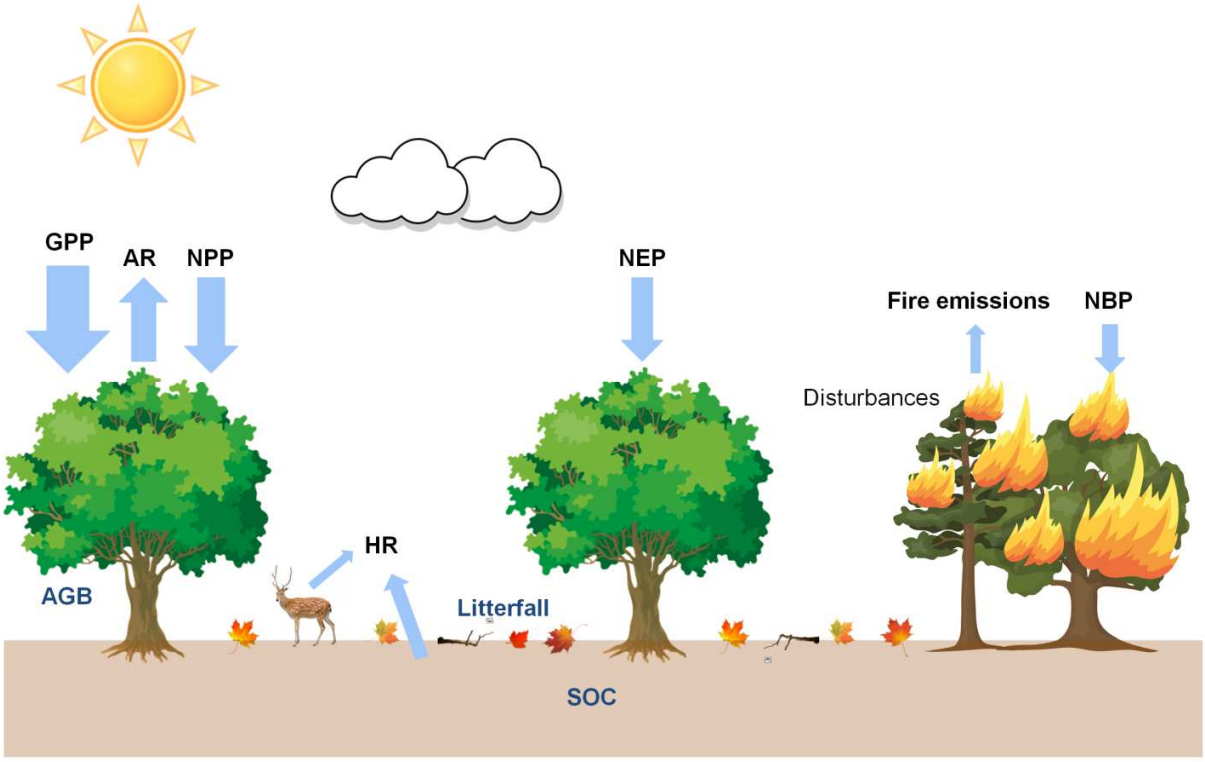

Figure 1. Carbon (C) fluxes and stocks that are quantified using remote sensing data and methods. The C fluxes that are estimated by remote sensing include gross primary production (GPP), ecosystem respiration (ER), net primary production (NPP), net ecosystem production (NEP), and net biome production (NBP). The C stocks that are quantified by remote sensing consist of aboveground biomass (AGB) and soil organic C (SOC). Fluxes contributing to NPP are GPP and autotrophic respiration (AR) (NPP=GPP-AR). Fluxes contributing to NEP are GPP, AR, and heterotrophic respiration (HR) (NEP = NPP-HR). The net ecosystem C balance, NBP, is mainly determined by NEP minus the loss of C by processes such as fire and harvest.

Ecosystem C fluxes and stocks are quantified with remotely sensed data acquired in the broad wavelength range of the electromagnetic spectrum from visible light to microwave (**Figure 2**). Ecosystem C flux components (e.g., GPP, NPP, ER, NEP, and NBP) are typically estimated using optical remote sensing data acquired in the visible, near-infrared (NIR), and

shortwave infrared (SWIR) wavelength. ER can also be estimated using LST observations from the thermal infrared (TIR) wavelength (Rahman et al. 2005; Kimball et al. 2009). Satellite-derived VIs (Rahman et al. 2005), LUE models (Running et al. 2004), and SIF (red and far red wavelength) (Li et al. 2018c) have been used to estimate GPP. Remotely sensed data have also been integrated with machine learning approaches (Xiao et al. 2008; Jung et al. 2009; Xiao et al. 2014a) and process-based models (Hazarika et al. 2005; Liu et al. 2018b) for quantifying C fluxes (e.g., GPP, NPP, ER, NEP, and NBP). NBP can also be estimated from total column CO_2 concentrations retrieved mainly in the SWIR wavelength (Rayner and O'Brien 2001). Both optical (Zhang and Kondragunta 2006; Blackard et al. 2008) and microwave (Dobson et al. 1992; Le Toan et al. 1992) remote sensing have been used to estimate biomass with allometric equations and/or empirical approaches. Optical remote sensing data have also been used to quantify SOC with empirical and machine learning approaches (Ben-Dor et al. 2002; Gomez et al. 2008). **Figure 2** illustrates the electromagnetic spectrum and the remote sensing of the terrestrial C cycle.

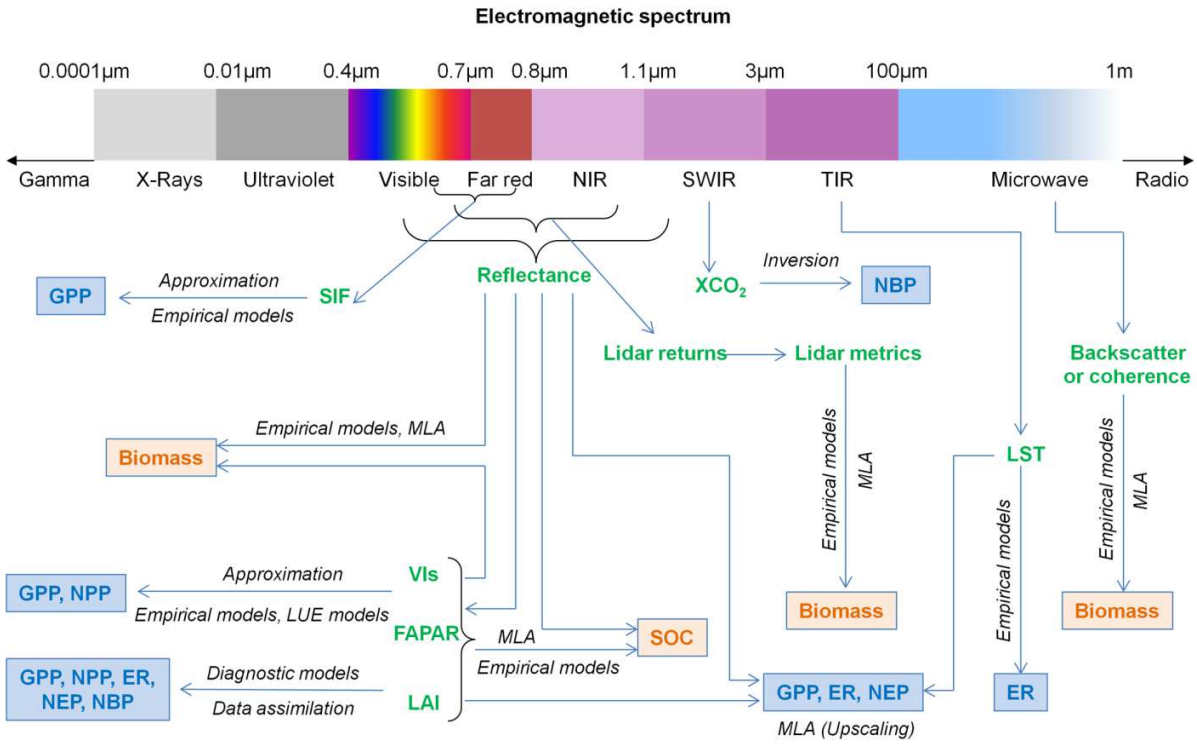

Figure 2. The electromagnetic spectrum and the remote sensing of the terrestrial carbon (C) cycle. The C flux components typically consist of gross primary productivity (GPP), net primary productivity (NPP), ecosystem respiration (ER), net ecosystem productivity (NEP), and net biome productivity (NBP). The C stocks consist of biomass and soil organic C (SOC). NIR, SWIR, and TIR stand for near-infrared, shortwave infrared, and thermal infrared wavelength, respectively, while MLA stands for machine learning approaches.

3. Milestones in remote sensing of the terrestrial carbon cycle

The development of the terrestrial C cycle area of environmental remote sensing during the last five decades is characterized by a series of milestones (**Figure 3**). The main milestones are briefly described below.

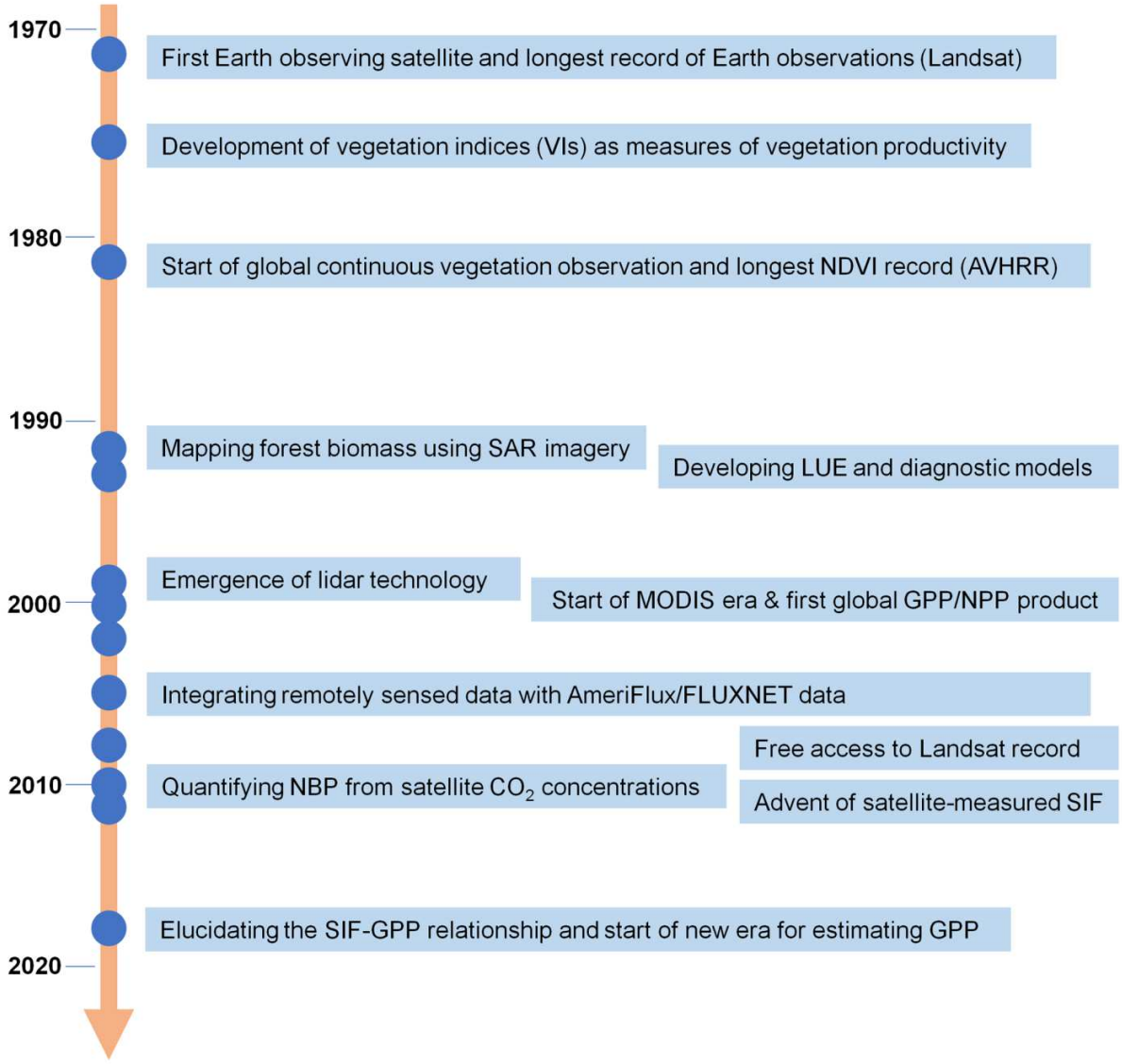

Figure 3. Milestones in remote sensing of the terrestrial C cycle.

3.1. First Earth observing satellite and longest record of Earth observations – the Landsat archive

Remote sensing of the terrestrial C cycle mainly started from the launch of the first Landsat satellite (Landsat 1) on July 23, 1972. The launch of Landsat 1 made the global land monitoring possible with optical measurements for the first time. The Landsat series of Earth-observing satellites (Landsat 1-8), co-managed by U.S. Geological Survey (USGS) and National

Aeronautics and Space Administration (NASA), provides the longest continuous observations of the Earth's surface from space (Wulder et al. 2016). Imagery from the Landsat series of satellites (Landsat 1-8) has been used to quantify C fluxes and stocks at regional to global scales (Foody et al. 2003; Masek and Collatz 2006). The Landsat archive now includes almost 50 years of observations globally, providing opportunities for investigating regional or global ecosystem C dynamics at multidecadal scales.

3.2. Start of global continuous vegetation observations and longest NDVI record – the AVHRR record

The advanced very high resolution radiometer (AVHRR), an instrument on board the National Oceanic and Atmospheric Administration's (NOAA) polar-orbiting meteorological satellites (NOAA 7, 9, 11, 14, 16-19), provides spatially and temporally continuous observations of global vegetation from 1981 to present (Pinzon and Tucker 2014). The AVHRR provides the longest, continuous surface reflectance and NDVI records globally at the spatial resolution of 8 km. The availability of the AVHRR observations since 1981 has made it feasible to monitor photosynthetic activity and GPP seamlessly over the globe. The most widely used AVHRR-derived NDVI records are perhaps the Global Inventory Monitoring and Modeling Studies (GIMMS) NDVI dataset and the GIMMS3g product (Pinzon and Tucker 2014). Other widely used AVHRR NDVI records include the Pathfinder NDVI dataset (James and Kalluri 1994) and AVHRR long term data record (LTDR) (Pedelty et al. 2007). The 30+ year AVHRR record allows the research community to examine C fluxes and/or stocks globally at annual and decadal times.

3.3. Mapping forest biomass using synthetic aperture radar (SAR) imagery

223 The availability of SIR-C/X-SAR and ERS-1/2 SAR imagery since the early 1990s greatly
224 facilitated the monitoring of forest biomass using SAR data (Dobson et al. 1992; Le Toan et al.
225 1992). They advanced studies of SAR interferometry on the estimation of forest AGB. The
226 JERS-1, PALSAR, and PALSAR2 provide multi-year global coverage of L-band SAR data
227 which enabled more studies on forest biomass estimation from SAR data. In addition, PolInSAR
228 and TomoSAR provide a new technique for estimating AGB by detecting the 3D structure of
229 forests. Microwave signals can penetrate clouds and therefore SAR can collect data continuously
230 in all weather conditions, allowing the estimation of biomass in large regions including areas
231 often covered by clouds.

232 **3.4. Start of the MODIS era and the first operational global GPP/NPP product**

233 The MODerate resolution Imaging Spectroradiometer (MODIS) on board two key satellites of
234 NASA's Earth Observing System (EOS) - Terra and Aqua provides observations of the Earth's
235 surface and atmosphere with daily coverage in 36 spectral bands and a spatial resolution from
236 250 m to 1 km. These two major EOS platforms have been providing global observations of the
237 atmosphere, land, and oceans since February 2000 and June 2002, respectively. Compared with
238 AVHRR, MODIS provides observations of the Earth's surface with better radiometric quality
239 and higher spatial resolution. In particular, the MODIS GPP/NPP product (Running et al. 2004)
240 provides spatially continuous GPP and NPP estimates globally. The MODIS data products have
241 also been used to develop continental scale forest biomass maps (Zhang and Kondragunta 2006;
242 Blackard et al. 2008), and also to enable the estimation of GPP, ER, and NEP with 1 km spatial
243 resolution at regional and continental scales (Xiao et al. 2014a). The availability of MODIS
244 ASCII subsets for a variety of MODIS data products (e.g., surface reflectance, NDVI/EVI, LAI,
245 the fraction of photosynthetically active radiation or FAPAR, GPP/NPP, albedo) (Cook et al.

2004) allows scientists to extract MODIS data for the grid cell or local area (e.g., 3 km × 3 km, 7 km × 7 km) surrounding specific research sites. This has greatly facilitated the calibration and evaluation of LUE models (Yuan et al. 2007; Mahadevan et al. 2008) and machine learning approaches (Xiao et al. 2008; Jung et al. 2009) and the data assimilation of terrestrial biosphere models (Stockli et al. 2008) for estimating C fluxes.

3.5. Emergence of lidar technology

Lidar can provide accurate information on the vertical structure of forests and therefore can be used to quantify forest AGB. Lidar data were first used to estimate AGB of temperate deciduous forests (Lefsky et al. 1999). Following this pioneering work, many studies have quantified forest AGB at landscape or regional scales using airborne lidar data (Drake et al. 2002; Naesset and Gobakken 2008). The availability of spaceborne lidar data in the 2000s made it feasible to map forest AGB over large regions or even over the globe using lidar data (Lefsky et al. 2005). Lidar data have also been used to estimate biomass for other ecosystems such as shrublands and grasslands (Wu et al. 2009; Li et al. 2017). The integration of spaceborne lidar data with other satellite data (e.g., MODIS, Landsat, SAR) can be used to map forest biomass seamlessly at regional to global scales (Saatchi et al. 2012).

3.6. Integrating remotely sensed data with AmeriFlux and FLUXNET measurements

The eddy covariance (EC) technique provides continuous measurements of C, water, and energy exchange at the ecosystem level at various timescales (e.g., diurnal, synoptic, seasonal, and interannual) (Nie et al. 1992; Wofsy et al. 1993; Baldocchi et al. 2001). The partitioning of the NEE measurements can lead to continuous GPP and ER estimates. The EC technique was pioneered in the late 1980s in field campaigns (e.g., FIFE grassland study) (Nie et al. 1992). A growing number of EC flux sites have been established across the globe since the early 1990s.

Regional flux networks (e.g., AmeriFlux) and FLUXNET coordinate analysis of EC flux measurements at regional and global scales, respectively, and have made standardized flux datasets available to the research community. The recently released FLUXNET2015 dataset (http://fluxnet.fluxdata.org/data/fluxnet2015-dataset/) provides standardized and high-quality flux and meteorological data for a total of 212 sites globally and has up to 15 years of overlap between flux data and MODIS data products. These flux datasets have been used to evaluate or calibrate C fluxes derived from remote sensing approaches. For example, AmeriFlux data have been used to evaluate the MODIS GPP product (Heinsch et al. 2006; Xiao et al. 2014a) and to estimate parameters in LUE models (Xiao et al. 2011b, 2014b). The release of the AmeriFlux and FLUXNET datasets also enabled the upscaling of flux observations and the generation of gridded GPP, ER, and NEP estimates at regional to global scales using machine learning approaches (Xiao et al. 2008; Jung et al. 2011). The National Ecological Observatory Network (NEON) has begun operations, and this continental-scale observation system will measure C, water, and energy fluxes through 47 terrestrial sites across the U.S. The integration of remote sensing with the measurements from AmeriFlux, FLUXNET, NEON, and other flux networks will greatly benefit carbon cycle studies.

3.7. Quantifying NBP from satellite observations of column CO_2 concentrations

The availability of column CO_2 concentrations retrievals from satellites in the 2000s and 2010s has made it feasible to quantify NEP from satellite observations. Column CO_2 concentrations data have been obtained from the SCanning Imaging Absorption spectroMeter for Atmospheric CartograpHY (SCIAMACHY) on board ESA's ENVIronment SATellite (EnviSat) (2002-2012) (Barkley et al. 2006), the Thermal and Near Infrared Sensor for Carbon Observation-Fourier Transform Spectrometer (TANSO-FTS) on board GOSAT (launched in 2009) (Wunch et al.

292 2011), NASA's OCO-2 (2014-present), and the Atmospheric Carbon Dioxide Grating
293 Spectrometer (ACGS) on board the Chinese Carbon Dioxide Observation Satellite (TanSat)
294 (2016-present). For example, Basu et al. (2013) estimated the distribution of CO_2 fluxes globally
295 using column CO_2 measurements from GOSAT. Inversions of satellite CO_2 observations provide
296 useful constraints on terrestrial C sinks/sources, although significant biases exist for fluxes even
297 aggregated over continental scales (Basu et al. 2013; Reuter et al. 2014).

298 **3.8. Free access to the Landsat record**

299 Prior to 2008, the cost and access to Landsat imagery had always limited our ability to monitor
300 the Earth's land surface (Woodcock et al. 2008). On April 21, 2008, the USGS announced plans
301 to make all archived Landsat scenes available to all users at no charge. The research community
302 has had "Web-enabled" access to the entire Landsat record since then. This new data policy has
303 revolutionized the use of the Landsat archive in creating new science, methods, and data
304 products (Wulder et al. 2012). The Landsat archive is also readily available on the Google Earth
305 Engine (Gorelick et al. 2017) for scientific analysis. The free-access policy of the Landsat
306 archive and its availability on Google Earth Engine are anticipated to promote the study of the
307 terrestrial C cycle.

308 **3.9. Advent of solar-induced chlorophyll fluorescence measurement from space**

309 The recent availability of satellite-based SIF measurements has provided great potential for
310 estimating terrestrial GPP regionally or globally (Frankenberg et al. 2011; Joiner et al. 2011).
311 Previous studies have demonstrated strong correlations between SIF and GPP by examining the
312 relationship of satellite-derived SIF with coarse-resolution, gridded GPP data products (Guanter
313 et al. 2012; Parazoo et al. 2014) or flux tower GPP more recently (Sun et al. 2017; Verma et al.
314 2017; Wood et al. 2017; Li et al. 2018b, 2018c). Previous studies showed that SIF predicted GPP

315 better than satellite-derived VIs and LUE models (Frankenberg et al. 2011; Li et al. 2018b,
316 2018c). SIF is also likely to be more sensitive to changes in plant photosynthetic status caused by
317 environmental stresses such as heat and water stresses than most VIs (Daumard et al. 2010;
318 Middleton et al. 2018; Zarco-Tejada et al. 2013; Joiner et al. 2014; Rascher et al. 2015) and has
319 been increasingly used to examine the dynamics of terrestrial photosynthesis and its responses to
320 drought (Sun et al. 2015; Yoshida et al. 2015; Li et al. 2018a). Satellite-based SIF observations
321 will likely bring revolutionary changes to the estimation of terrestrial photosynthesis from space.

322 **4. Remote sensing of carbon fluxes**

323 Carbon fluxes can be quantified using various remote sensing data and methods. This section is
324 divided into the following sub-sections: vegetation indices, light use efficiency models,
325 terrestrial biosphere models, data-driven (or machine learning) approaches, solar-induced
326 chlorophyll fluorescence, land surface temperature, and atmospheric inversions.

327 **4.1. Satellite-derived vegetation indices as proxies of GPP and NPP**

328 VIs derived from remote sensing spectral measurements are perhaps the most basic spectral
329 measures of plant biologic activity from space. They combine the chlorophyll-sensitive red
330 absorbing band with the leaf- and canopy structure-sensitive, NIR band, to represent a
331 community property of canopy “greenness” encompassing canopy structure, chlorophyll content,
332 plant phenology and leaf ontogeny. VIs aim to quantify the presence and extent of green
333 vegetation and enable intercomparisons of vegetation “greenness”" across space and time. The
334 earliest VIs, such as the NDVI (Rouse et al. 1974), the perpendicular vegetation index (PVI)
335 (Richardson and Wiegand 1977), and the tasselled cap green vegetation index (TC-GVI) (Kauth
336 and Thomas 1976), have been widely used for estimating plant productivity. More recently
337 developed greenness and chlorophyll indices include the EVI (Huete et al. 2002), the wide

338 dynamic range vegetation index (WDRVI) (Gitelson 2004), and the MERIS total chlorophyll
339 index (MTCI) (Dash and Curran 2004). The robustness of VIs and available long term time
340 series have generated a vast number of carbon-climate studies over northern latitudes, Africa,
341 and the Amazon (Tucker et al. 1986; Myneni et al. 1997a; Tucker et al. 2001; Zhou et al. 2001;
342 Xiao and Moody 2005; Saleska et al. 2016).

343 The phenological life cycle of plant species has large effects on photosynthesis rates and
344 annual productivity (Tucker et al. 1986), and VIs are able to provide seasonal and annual
345 growing season metrics of plant productivity. Previous studies found strong relationships
346 between aboveground NPP (ANPP) and growing season integrated NDVI for North American
347 biomes (Goward et al. 1985) and later between ANPP and EVI for U.S. arid grasslands to forests
348 (Ponce-Campos et al. 2013) and arid and mesic grasslands (Moran et al. 2014). In general, VIs
349 provide measures of the capacity of plants to absorb light energy and to reflect recent
350 environmental stresses with reductions in NDVI indicative of less chlorophyll and/or less foliage
351 (Running et al. 2004). Primary production is essentially an integrator of resource availability, and
352 according to the resource optimization theory (Field et al. 1995), plants can maximize
353 photosynthesis and growth with the adjustment plant characteristics by ecological processes to
354 match the environmental capacity at weekly to monthly timescales. Often in-situ ANPP-VI
355 uncertainties may arise due to discrepancies in timing of harvesting sampling periods. For
356 example, when EVI was only partially integrated from the beginning to the peak of the growing
357 season period (rather than the full season), significant improvements in productivity–EVI
358 relationships were found across grassland sites (Moran et al. 2014). The NDVI integral over the
359 early growing season was strongly related to in-situ measurements of tree diameter and ring

360 width in the central Great Plains (Wang et al. 2004). Continuous VI growing season productivity
361 profiles allow one to better synchronize VI temporal values with actual in-situ sampling periods.
362 VIs are used to estimate the rates of ecosystem processes (e.g., photosynthesis) that depend
363 on absorbed light (Monteith and Unsworth 1990). With the widespread use of VIs in large-scale
364 productivity assessments, there is great interest in learning how to best couple VIs with in-situ
365 productivity measures from flux towers. Further, the flux tower observations are top-of canopy
366 measurements that do not need details of canopy architecture or LAI, facilitating their
367 comparisons with VI measures that similarly involve community properties resulting from
368 integrative, top-of-canopy radiation interactions. VIs in combination with meteorological data
369 (e.g., temperature, vapor pressure deficit or VPD, solar radiation) have been used to estimate
370 GPP at various spatial scales using LUE models as described below in 3.2. There have also been
371 many attempts to estimate GPP based solely on remote sensing inputs, thereby minimizing or
372 eliminating the need for meteorological and LUE information. Spectral VIs were found to
373 accurately estimate GPP across a wide range of North American ecosystems (Wylie et al. 2003;
374 Rahman et al. 2005), African tropical savannas (Sjostrom et al. 2011), Australian mesic and xeric
375 tropical savannas (Ma et al. 2013), various terrestrial ecosystems in China (Xiao, Zhou, & Zhang
376 2015), and dry to humid tropical forests in Southeast Asia and the Amazon (Huete et al. 2006;
377 Huete et al. 2008). A more recent study examined the relationship between satellite-derived VIs
378 and flux tower GPP for 121 FLUXNET sites encompassing a wide range of biomes across the
379 globe and assessed how the VI-GPP relationship varies with indices, biomes, timescales, and the
380 bidirectional reflectance distribution function (BRDF) effect (Huang et al. 2019). These studies
381 indicated that VIs are able to estimate GPP with relatively high accuracy, thus potentially

382 simplifying C balance models and offering opportunities for region-wide upscaling of C fluxes
383 (Glenn et al. 2008).

384 The above studies, however, reported weaker relationships between VIs with tower GPP over
385 aseasonal evergreen forests compared to seasonally contrasting deciduous forests. This may
386 simply be due to the low seasonal signal range of VI values from which to statistically fit good
387 relationships, although significant differences in VI relationships with tower GPP were found
388 between biologically driven and meteorologically driven ecosystems (Restrepo-Coupe et al.
389 2016). No significant relationships between GPP and VIs were observed for primarily
390 meteorological-driven and relatively aseasonal ecosystems (e.g., tropical forests). On the other
391 hand, for phenology-driven ecosystems, GPP is driven by changes in the vegetation status and
392 can be well represented by VIs. The highest VI-GPP correlations were found in ecosystems with
393 synchronous meteorology and phenology, while low correlations were observed in locations with
394 asynchronous meteorology and phenology (e.g., Mediterranean ecosystems). When successful,
395 satellite-derived VIs constitute measurements of ecosystem structure and function, and are more
396 related to measures of photosynthetic capacity (the maximum photosynthesis rate under ideal
397 conditions of light, moisture, temperature, and nutrient availability) rather than GPP. Besides VIs,
398 biophysical variables (e.g., canopy nitrogen content, chlorophyll content) derived from remote
399 sensing data have also been used to estimate C fluxes. For example, canopy nitrogen content
400 retrieved from hyperspectral airborne (e.g., the Airborne Visible/Infrared Imaging Spectrometer
401 or AVIRIS) and broad-band satellite (e.g., MODIS) imagery has been used to estimate
402 photosynthetic capacity (Ollinger et al. 2008) and NPP (Smith et al. 2002). These studies are
403 mainly limited to landscapes and small regions due to the limited availability of hyperspectral
404 data.

405 **4.2. Estimating GPP and NPP with light use efficiency models**

406 The LUE models (i.e., production efficiency models) are widely used to quantify GPP and NPP
407 from remotely sensed data. LUE models are based on the original radiation use efficiency logic
408 of Monteith (1972) that under well-watered and fertilized conditions the productivity of a
409 cropland exhibits a linear relationship with the absorbed photosynthetically active radiation
410 (APAR) by the canopies. Under actual environmental conditions, potential optical energy
411 utilization rate is affected by water, temperature and other environmental factors. Therefore, GPP
412 (or NPP) can be simulated in the LUE logic as APAR multiplied by maximum LUE and
413 environmental stresses. The LUE approach has been one of the most important methods to map
414 GPP and NPP regionally or globally (Potter et al. 1993; Running et al. 2004).

415 Remote sensing data play a significant role in the LUE approach by providing information on
416 vegetation type, growth status and environment conditions. FAPAR is derived through spectral
417 VI relationships (Asrar et al. 1984; Sellers 1985; Goward and Huemmrich 1992) or based on
418 FAPAR products (e.g., MODIS FAPAR) (Zhao et al. 2005). Asrar et al. (1984) demonstrated the
419 NDVI was linearly related with vegetation absorption of light energy (APAR) or FAPAR, and
420 thereby related to productivity through the potential capacity of vegetation to absorb light for
421 photosynthesis. The linear relationship between NDVI and FAPAR has been documented
422 through field measurements (Ruimy et al. 1995; Fensholt et al. 2004) and theoretical analyses
423 (Sellers 1985; Goward and Huemmrich 1992; Myneni and Williams 1994), although their
424 relationship differs with canopy type, structure, soil, and sun-view orientation and saturates at
425 high values (e.g., NDVI>0.7). AVHRR-FAPAR (Zhu et al. 2013) and GLASS-FAPAR products
426 (Xiao, Liang, Sun et al. 2015) extend the temporal coverage of FAPAR back to 1982 and benefit
427 to generate long-term GPP products. A previous study suggested that the fraction of PAR

absorbed by chlorophyll throughout the canopy (fAPARchl) could lead to more accurate cropland GPP estimates than the MODIS FAPAR (Zhang et al. 2014b). Remote sensing also provides measures of two other inputs of LUE models: water stress (Jones et al. 2017) and incident radiation (Zhang et al. 2014c). The photochemical reflectance index (PRI) (Gamon et al. 1997) derived from tower-based spectral measurements (Middleton et al. 2009) and MODIS data (Middleton et al. 2016) has been shown to be a good proxy for LUE. In addition, remote sensing also provides spatially explicit information on land cover type (Loveland et al. 2000; Friedl et al. 2010) that determines maximum LUE and other model parameters.

A number of LUE models have been developed and widely used for quantifying GPP (or NPP) (Potter et al. 1993; Running et al. 2004; Xiao et al. 2004; Yuan et al. 2007). In particular, a LUE approach along with NDVI (or EVI) was implemented in the Carnegie Ames Stanford Approach (CASA) Biosphere model for simulating NPP (Potter et al. 1993). CASA has been widely used to simulate C dynamics at regional to global scales although it could lead to large biases in simulated C fluxes (Randerson et al. 2009). Moreover, a LUE approach along with MODIS data were used to develop the standard MODIS GPP/NPP product, the first operational and most widely used GPP/NPP product (Running et al. 2004) (**Figure 4**). All LUE models integrate the physiological regulations of temperature and water demand (soil moisture or atmospheric VPD). Some models also incorporate the enhancement effects of atmospheric CO_2 fertilization (Veroustraete et al. 2002). In addition, some models (e.g., CFlux, TL-Model) explicitly simulate the differential effects of diffuse and direct radiation on photosynthesis (Gu et al. 2002) using an empirical equation or a two-leaf model (King et al. 2011; Zhou et al. 2016). LUE models with the addition of a linear or nonlinear function of air temperature have also been used to estimate NEE (Mahadevan et al. 2008; Xiao et al. 2011b). Different LUE models differed

in algorithms describing the regulations of environmental stresses particularly water stress on GPP (Yuan et al. 2014). Different model structures and parameterization schemes can result in marked discrepancies in GPP estimates (Xiao et al. 2011b; Cai et al. 2014; Yuan et al. 2014). Having proper model structure that accurately represents the regulation of all driving factors on GPP is essential for improving the GPP estimates (Zheng et al. 2018). Uncertainty in model parameters could lead to substantial uncertainty in flux estimates at regional scales (Xiao et al. 2014b).

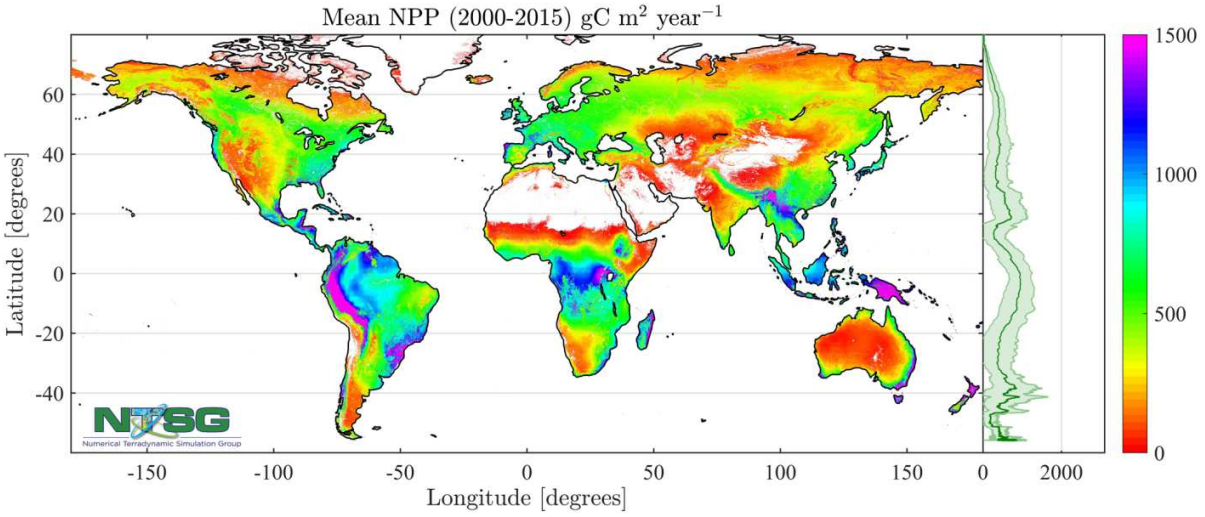

Figure 4. Global mean annual NPP (gC m^{-2} $year^{-1}$) over the period 2000-2015 based on the MODIS GPP/NPP product. (Courtesy of Steven W. Running)

Reducing uncertainty in the GPP (or NPP) estimates is one of the challenges of LUE models. A model-data comparison study showed most LUE models underestimated GPP at cloudy or overcast days because the effects of diffuse radiation from cloud cover on LUE were ignored (Yuan et al. 2014). A recent study revealed that soil moisture stress alone reduced GPP at semi-humid, semi-arid, or arid sites by up to 40%, but most LUE models only integrate the effects of atmospheric water demand that cannot account for the limitation of soil moisture on GPP

(Stocker et al. 2018). A second challenge revolves around the fact that the uncertainty of remote sensing data would further lead to uncertainty in vegetation productivity estimates. For instance, the saturation problem of satellite-derived VIs generally results in underestimation of GPP or NPP in areas with dense vegetation. In addition, the global GPP products based on LUE models are at medium spatial resolution (e.g., 1 km), limiting their use in some applications (e.g., estimating regional crop yield, quantifying GPP in urban areas) that require GPP products with finer spatial resolution. The fusion of temporally dense satellite data (e.g., MODIS) and spatially finer observations (e.g., Landsat) can allow the estimation of GPP at finer spatial resolution (e.g., 30 m) (He et al. 2018), overcoming the limitations of current GPP products due to coarse resolution.

4.3. Quantifying carbon fluxes using terrestrial biosphere models

Process-based terrestrial ecosystem models describe terrestrial C, water, and energy fluxes in a mechanistic way to quantify these terrestrial cycles. The process-based representation of ecosystem processes allows us to understand terrestrial ecosystem status and changes in mechanistic ways. These models can be divided into two categories: diagnostic models and prognostic models. Diagnostic models use remotely sensed data (e.g., LAI, FAPAR) as temporally-variant input data to capture spatial and temporal variations in terrestrial vegetation in a more realistic way, and therefore their simulations are limited to the period when remotely sensed data are available. Prognostic models, in general, use climate data as temporally-variant input data and can simulate past-present-future changes in terrestrial ecosystem status. Many terrestrial model intercomparison studies revealed large uncertainties in simulated CO_2 fluxes at both site (Ichii et al. 2013) and regional (Huntzinger et al. 2012) scales. Therefore, refinements

490 of these models are strongly required. Both diagnostic models and prognostic models can make
491 use of remotely sensed data to improve their performance in quantifying C fluxes.
492 Diagnostic models generally adopted process-based photosynthesis sub-models (Farquhar et
493 al. 1980; Collatz et al. 1991). With temporally-variant inputs of satellite-based LAI and/or
494 FAPAR, photosynthesis is simulated and GPP is then calculated. These models are designed to
495 estimate GPP in a more realistic way by considering mechanistic behaviors of photosynthesis
496 responding to environmental conditions (e.g., climate and atmospheric CO_2 concentration) and
497 incorporating actual spatial and temporal variations in LAI and/or FAPAR. Most diagnostic
498 models, such as SiB2 (Sellers et al. 1996), BEPS (Liu et al. 1997), InTEC (Chen et al. 2000), and
499 BEAMS (Sasai et al. 2005), contain biomass and soil C pools. Therefore, these models can
500 simulate not only GPP but also other C fluxes (e.g., NPP, ER, NEP, and NBP). In general, these
501 process-based models use a similar approach to calculate autotrophic respiration and
502 heterotrophic respiration based on the first-order decay with the responses to the environmental
503 factors. NEP is calculated as the difference of GPP and ER. Some diagnostic models like the
504 Breathing Earth System Simulator (Ryu et al. 2011) can only explicitly simulate GPP.
505 Remotely sensed data are also integrated with prognostic models for quantifying ecosystem
506 C fluxes. Prognostic models internally simulate LAI based on climate and soil data, C allocation,
507 and specific leaf area. The data assimilation is an effective approach to constrain and improve
508 prognostic models and to reproduce more realistic ecosystem status using remotely sensed data
509 (e.g., LAI). For example, satellite-based LAI data were used to nudge the Sim-CYCLE model
510 (Hazarika et al. 2005). If the simulated LAI did not converge with the MODIS-LAI, the
511 simulated LAI was replaced with the MODIS-LAI and then C fluxes were re-simulated. The
512 assimilation of the MODIS LAI improved the simulation of NPP. Similarly, the assimilation of

MODIS LAI retrievals into a Dynamic Global Vegetation Model (DGVM) reduced the growing season length and improved the estimates of GPP and NPP globally (Demarty et al. 2007). Kleidon (2004) and Ichii et al. (2009) improved NPP and GPP simulations by inversely estimating rooting depths using simple diagnostic ecosystem models and satellite-derived APAR and evapotranspiration. Satellite data have also been used to optimize parameters of terrestrial biosphere models. For example, satellite-derived FAPAR was used to reduce the uncertainty in parameters in a terrestrial ecosystem model – BETHY, and the parameter optimization improved the performance of the model for simulating C fluxes (Kato et al. 2013). A more recent study used satellite NDVI observations together with EC data and atmospheric measurements to optimize ~180 parameters of the ORCHIDEE model (Peylin et al. 2016).

Satellite-derived data products can have significant uncertainty that in turn can propagate through model simulations and result in uncertainty in simulated fluxes. For example, a recent modeling study showed that the significant uncertainty in satellite-derived LAI products led to substantial uncertainty in GPP simulated by BEPS, a prognostic process-based model (Liu et al. 2018b). The uncertainty in satellite data products (e.g., LAI) will also lead to uncertainty in C fluxes simulated by prognostic models assimilating these products. Moreover, additional remotely sensed data that process-based models require may not be readily available. For example, historical disturbance information (e.g., land cover change, forest age, fire) are key inputs to process-based models for simulating the terrestrial C cycle. Forest age maps have been generated at regional to continental scales using inventory and remote sensing information (Pan et al. 2011; Zhang et al. 2014a), although it still remains a challenge to develop forest age maps at the global scale. Diagnostic process-based models typically contain a number of processes and parameters and are much more complex than LUE models. Unlike LUE models, diagnostic

models also require model initialization (model spinup), and therefore powerful computation resources are often required to run these models at regional or global scales. In addition, the required spinup process to create initial state of terrestrial biosphere pools sometimes makes the model simulation difficult in the case of diagnostic process based models. In general, time-series inputs of remotely sensed products (e.g. LAI, FAPAR, NDVI) are limited to the satellite observation periods, and therefore it is sometimes difficult to create reasonable initial spinup outputs.

4.4. Quantifying GPP, ER, and NEP using data-driven approaches

Remote sensing has been widely used to scale flux observations from EC flux towers to broad regions during the last decade or so. The growing network of flux towers provides continuous observations of the exchange of C, water, and energy between ecosystems and the atmosphere. Despite the large number of flux towers across the globe, they are not uniformly distributed and the tower measurements only represent the fluxes at the small tower footprint. The quantification of C fluxes at regional to global scales require the upscaling of the flux observations to these broad regions (Xiao et al. 2008; Jung et al. 2011).

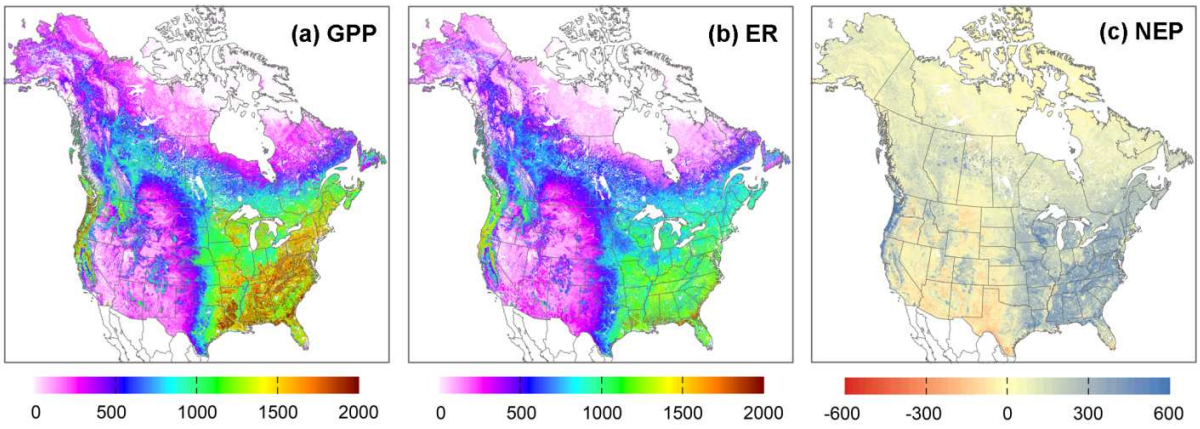

552 **Figure 5**. Mean annual carbon fluxes over North America for the period 2001-2012: (a) GPP); (b) ER;
553 and (c) NEP derived from a data-driven approach. The units for carbon fluxes are g C m^{-2} yr^{-1}. (Adapted
554 from Xiao et al., 2014b)
555
556 Data-driven (or machine learning) approaches have been used to upscale C fluxes (GPP, ER,
557 NEE) from sites to regional or global scales (Zhang et al. 2007; Xiao et al. 2008; Jung et al. 2011;
558 Ichii et al. 2017). A special issue published in Journal of Geophysical Research: Biogeosciences
559 (Xiao et al. 2012) reflected the progress in the upscaling of carbon and water fluxes form towers
560 to broad regions prior to 2012, and significant advances have been made since then. The machine
561 learning approaches used include artificial neural network (Papale and Valentini 2003), support
562 vector machine (Yang et al. 2007), piecewise regression models (Zhang et al. 2007; Xiao et al.
563 2008), model tree ensemble (Jung et al. 2009), and random forest (Bodesheim et al. 2018). For
564 example, a data-driven approach based on piecewise regression models were used map GPP, ER,
565 and NEE for North America from MODIS and meteorological data (Xiao et al. 2014a) (**Figure**
566 **5**). A recent study showed that four different data-driven techniques, including the adaptive
567 neuro-fuzzy inference system, artificial neural network, extreme learning machine, and support
568 vector machine, had almost identical performance in estimating forest C fluxes (Dou and Yang
569 2018). Although machine learning approaches differ from mechanistic models and do not
570 explicitly incorporate biogeochemical processes, the machine learning methods can effectively
571 estimate C dynamics through time and space and also reveal plant responses to environmental
572 controls.
573 A variety of remotely sensed datasets such as VIs (e.g., NDVI, EVI), LAI, FAPAR, and land
574 cover type have been used in data-driven approaches for the upscaling of C fluxes. Both daytime
575 and nighttime LST data from MODIS have been incorporated to provide temperature estimates

with finer spatial resolution than meteorological reanalysis data (Xiao et al. 2008; Xiao et al. 2010; Xiao et al. 2014a). Satellite-derived measures of water availability such as the normalized difference water index (NDWI) (Gao 1996) have also been incorporated as explanatory variables in upscaling efforts (Xiao et al. 2008; Xiao et al. 2010; Xiao et al. 2014a). Some studies used additional remotely sensed variables. For example, the incorporation of stand age and AGB improved the estimation of C fluxes for forests, and the addition of the proxy for canopy nitrogen content (i.e., the NIR reflectance integrated over the peak portion of the growing season) reduced the uncertainty in C fluxes for both forests and non-forests (Xiao et al. 2014a). A more recent study integrated satellite-derived SIF into the artificial neural network model for global GPP estimation, and indicated that SIF could improve the estimation of GPP in regions where flux variability is not mainly driven by phenology and incident radiation (Alemohammad et al. 2017).

Machine learning approaches have been used to estimate C fluxes with reasonable accuracy (Zhang et al. 2007; Xiao et al. 2008; Jung et al. 2009; Xiao et al. 2010). The accuracy of the resulting GPP estimates is generally comparable to or slightly better than that of other approaches (e.g., LUE models) (Zhang et al. 2007; Ichii et al. 2017). The accuracy of ER was generally lower than that of GPP (Xiao et al. 2014a; Boyte et al. 2018) partly because the spatially explicit information on C pools and soil conditions is not readily available (Xiao et al. 2014a) and the regulation of soil respiration by temperature and precipitation is not well understood (Boyte et al. 2018). In general, the NEP estimation accuracy was lower than that of GPP and ER (Jung et al. 2011; Tramontana et al. 2016; Ichii et al. 2017; Bodesheim et al. 2018). Tramontana et al. (2016) compared 11 regression algorithms for estimating global ecosystem C fluxes, indicating that the accuracy of ER was slightly lower than that of GPP but higher than that of NEP. The lower accuracy in NEP estimates can be attributed to the lack of information on

599 disturbance history, stand age, biomass, SOC, and management practices (Xiao et al. 2014a;
600 Papale et al. 2015). Based on the inter-comparison of models, a previous study showed that the
601 Support Vector Machine was comparable to eight process-based models (Ichii et al. 2010).
602 Another multi-model comparison study showed that the upscaling approaches based on machine
603 learning methods were comparable to, or slightly better than, most ecosystem models (Raczka et
604 al. 2013).

605 Despite their simplicity and effectiveness, the machine learning approaches face challenges
606 and the resulting flux estimates have various sources of uncertainty. First, the number of EC flux
607 sites and their distribution can significantly affect the accuracy and interannual variability of the
608 regional flux estimates based on machine learning methods (Papale et al. 2015). A recent study
609 based on multiple machine learning algorithms found that fluxes were better predicted in
610 temperate regions than under-represented regions (e.g., the tropics) (Tramontana et al. 2016). In
611 addition, the errors or uncertainty of satellite data and other explanatory variables (e.g.,
612 meteorological data) could propagate and lead to biases in the gridded flux estimates. The NEE
613 estimates could have substantial uncertainty, particularly in productive regions, which makes it
614 challenging to quantify the sizes of C sinks and sources. Explicitly incorporating information on
615 management and disturbance into the machine learning approaches is anticipated to improve the
616 accuracy of the resulting flux estimates.

617 **4.5. Estimating GPP with solar-induced chlorophyll fluorescence**

618 SIF is an electromagnetic signal emitted in the red and far-red portions of the spectrum by green
619 leaves after excitation by solar radiation. SIF originates at the core of the photosynthetic
620 apparatus and holds a mechanistic link to photosynthesis and is thus a better proxy of GPP than
621 other biophysical parameters or VIs (Porcar-Castell et al. 2014). The relationship between SIF

and GPP has been examined by a growing number of field studies (Flexas et al. 2000; Meroni et al. 2008; Rascher et al. 2009; Daumard et al. 2010; Damm et al. 2015; Rossini et al. 2015; Yang et al. 2015b; Migliavacca et al. 2017; Yang et al. 2017; Miao et al. 2018; Yang et al. 2018; Gu et al. 2019). These studies have shown that SIF has the potential to indicate actual (as opposed to potential) plant photosynthetic activity, but at the same time have revealed the complexity of the link between top-of-canopy SIF measurements and GPP for the whole canopy.

At regional to global scales, an important breakthrough was made in 2011 with the development of global SIF maps (Frankenberg et al. 2011; Joiner et al. 2011) (**Figure 6**) based on measurements from the Japanese GOSAT mission. The SIF was retrieved by evaluating the in-filling of the solar Fraunhofer lines by SIF present in the 755–775 nm window. Following these two pioneering studies, several global SIF datasets have been produced from other space-borne spectrometers, including GOME-2 (the Global Monitoring Ozone Experiment 2) and SCIAMACHY (the SCanning Imaging Absorption spectroMeter for Atmospheric CartograpHY) (Joiner et al. 2012; Joiner et al. 2013; Kohler et al. 2015; Wolanin et al. 2015) and more recently from OCO-2 (Sun et al. 2018) and TROPOMI (the TROPOspheric Monitoring Instrument) (Kohler et al. 2018). The GOME-2 SIF dataset has been the most widely used SIF product because of its continuous spatial sampling, global coverage, and long time series despite its coarse spatial resolution (40 km × 40 km in the best case). OCO-2, in turn, samples only a small portion of the Earth's land surface, but its relatively high spatial resolution (1.3 km × 2.25 km at nadir) makes it to be the first mission allowing direct comparisons of SIF retrievals and flux tower-based GPP estimates at the ecosystem scale (Verma et al. 2017; Wood et al. 2017; Li et al. 2018b, 2018c), which promises to deliver important information for the understanding of SIF-GPP relationships. The discrete OCO-2 soundings have also been used to generate spatially and

645 temporally continuous SIF estimates globally. For example, Li and Xiao (2019) developed the
646 global, OCO-2 based SIF product (GOSIF) with 0.05-degree resolution and 8-day time step for
647 the period from 2000 to present using OCO-2 SIF, MODIS, and meteorological reanalysis data.
648 In addition, the first SIF retrievals from TROPOMI have become available very recently (Kohler
649 et al. 2018). TROPOMI shares the spatially-continuous sampling of GOME-2 and its potential
650 for SIF retrieval at both red and far-red wavelengths, but offers a much better monitoring
651 potential because of the finer spatial resolution (i.e., 3 km ×7 km at nadir), a number of clear-sky
652 SIF observations, and daily global coverage. The bidirectional effects associated with the wide
653 swath of TROPOMI might introduce difficulty to the retrieval of far-red fluorescence.

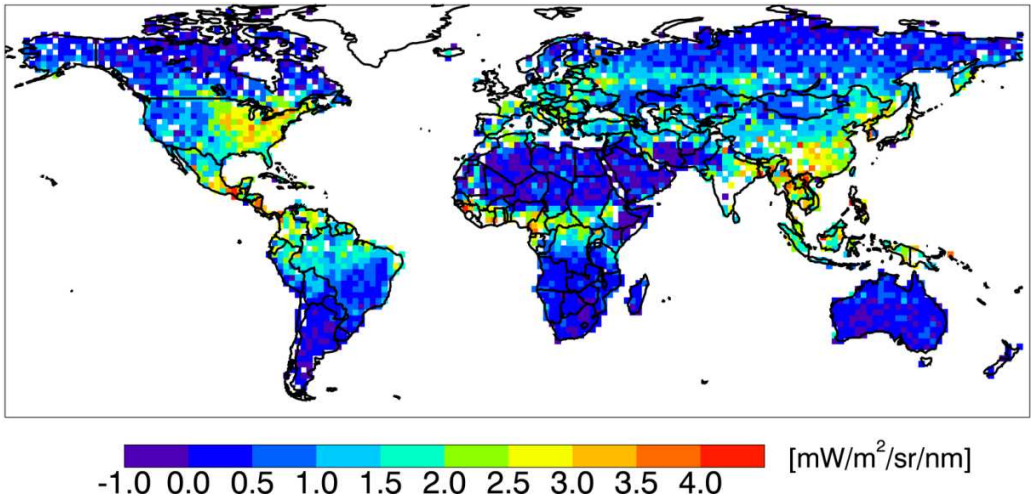

654

655 **Figure 6**. First global solar-induced chlorophyll fluorescence (SIF) map based on monthly averages of
656 instantaneous SIF for July 2009 from GOSAT P polarization. (Reproduced from Joiner et al. 2011)
657
658 A number of studies based on global SIF products have demonstrated that a close
659 relationship between SIF and GPP holds at ecosystem to global scales. A strong linear
660 correlation was observed between SIF based on GOSAT and gridded GPP data derived from
661 data-driven models for global and annual data composites (Frankenberg et al. 2011), and the

same applied to monthly averages over single biomes (Guanter et al. 2012). Joiner et al. (2014) found a good correspondence between the temporal trajectories of SIF and GPP. Li et al. (2018c) conducted a global-scale analysis based on OCO-2 soundings and flux tower data, showing that there was a strong relationship between SIF and GPP at the ecosystem level, and the relationship was also nearly universal across a wide variety of biomes. Other studies have focused on the analysis of the magnitude and dynamics of GPP using satellite-based SIF data over particular biomes, such as large crop belts (Guanter et al. 2014; Zhang et al. 2014d; Song et al. 2018), the Amazon forest (Lee et al. 2013; Parazoo et al. 2013; Guan et al. 2015), high latitude forests (Walther et al. 2016; Jeong et al. 2017), temperate forests (Li et al. 2018c), tundra ecosystems (Luus et al. 2017), and dryland ecosystems in Southwest U.S. (Smith et al. 2018). There is therefore a large body of literature showing that space-based SIF retrievals are able to represent GPP better than the reflectance-based vegetation parameters widely used in remote sensing.

To relate SIF to GPP some considerations should be taken into account. First, SIF is known to be a good indicator of green APAR, as SIF responds to PAR and is directly emitted by chlorophyll-a molecules. This close relationship between SIF and green APAR is most likely driving the high linear SIF-GPP correlations at coarse spatial and temporal scales (Yang et al., 2018) for those ecosystems (e.g., croplands, grasslands) in which productivity is driven by total chlorophyll content (Guanter et al. 2014). However, there is much less remote sensing-based evidence for the ability of SIF to track short-term changes in photosynthetic efficiency (Middleton et al. 2018). The SIF yield might be less sensitive than the photosynthesis yield under stress conditions (Wohlfahrt et al. 2018). In addition, although photosynthesis and fluorescence yields tend to be positively correlated under natural conditions, they have different temporal trajectories within the day and season for certain stress conditions (Porcar-Castell et al. 2014).

685 Second, the relationship between photosynthesis and top-of-canopy SIF measurements is
686 complicated by leaf and plant structure effects: a fraction of the SIF photons emitted by one leaf
687 can be trapped by other leaves, and is therefore not counted in the satellite measurement. This
688 effect strongly depends on canopy structure and leaf morphology and orientation (Fournier et al.
689 2012) as well as wavelength. Some studies dealing with this topic and proposing different
690 solutions for canopy-to-leaf downscaling have been published recently (Liu et al. 2018a; Romero
691 et al. 2018; Yang and van der Tol 2018), and further research is warranted in the next years.
692 Third, the clear-sky bias in space-based SIF retrievals complicates their use to quantify daily
693 GPP estimates comprising both clear- and cloudy-sky conditions. This clear-sky bias especially
694 affects SIF-based GPP estimates for those ecosystems in which clear-sky GPP differs
695 substantially from cloudy-sky GPP (Zhang et al. 2018b).

696 The systematic estimation of GPP from space-based SIF retrievals requires therefore an
697 explicit or implicit consideration of those confounding factors. Process-based modeling appears
698 as a potentially effective approach to dealing with this problem. Mechanistic models with
699 explicit representations of SIF and photosynthesis are being developed. For example, the SCOPE
700 (Soil Canopy Observation, Photochemistry and Energy fluxes) photosynthesis and fluorescence
701 model (van der Tol et al. 2009) couples SIF and GPP with a series of inputs describing
702 vegetation status (pigment content and canopy structure) and meteorological conditions, and it is
703 being widely used to analyze the relationship between SIF and GPP (Verrelst et al. 2015; Zhang
704 et al. 2016). In parallel, the photosynthesis modules of some DGVMs are being extended in order
705 to incorporate a consistent modeling of SIF (Lee et al. 2015b; Thum et al. 2017). An accurate
706 representation of photosynthesis and SIF in such global C models is a pre-condition to the use of
707 space-based SIF retrievals to benchmark terrestrial biosphere models and to improve their global

GPP predictions, which could be based on data assimilation schemes (Scholze et al. 2017; MacBean et al. 2018).

4.6. Estimating ER from land surface temperature

ER is a large C flux from the land to the atmosphere, and is thus an important contributor to the increasing atmospheric CO_2 and, consequently, global climate change (Le Quere et al. 2009). The underlying reason of correlating air (or soil) temperature to ER is that temperature is a main environmental controlling factor of respiration rates (Raich and Schlesinger 1992; Lloyd and Taylor 1994). A remote sensing approach of using LST has the potential of providing spatially distributed estimates of ER on a per-pixel basis. Rahman et al (2005) first found that the MODIS-derived LST (MOD11) was strongly correlated with the EC-derived ER, especially for densely forested sites. Many studies then tested the ER-LST relationship and its variations in other regions and for different biomes. A strong correlation between MODIS LST and tower ER was found for two Swedish peat lands (R^2 = 0.93 to 0.98) (Schubert et al. 2010). Moore et al. (2013) utilized a modified version of the 'TG' model (Sims et al. 2008), in which LST was combined with the EVI of a high-elevation insect-infested forest to estimate GPP and then to derive ER (Moore et al. 2013). The MODIS-derived LST was combined with a MODIS-derived water index to model ER of a mixed temperate forest with improved seasonal cycles in NEE (Tang et al. 2011). Although most of the LST-ER correlation studies used MODIS LST data, Kimball et al. (2009) used the LST derived from the Advanced Microwave Scanning Radiometer for EOS (AMSR-E) sensor and found it is an effective surrogate to soil respiration (HR and root respiration) across a broad range of boreal forest, grassland and tundra sites in the boreal and arctic biomes.

There are a few concerns on the use of LST for estimating ER. LST is not an exact measure of either soil temperature or vegetation temperature, but a complex thermal representation of the three-dimensional land surface. Satellite pixel size and the time of data acquisition also affect the LST values. Averaging LST values over a temporal period (such as 8 days for MODIS) and over a larger area (such as 3×3 MODIS pixels) acts as a smoothing filter, which can provide a better correlation with time averaged ER. Another limitation of the semi-empirical LST-ER correlation is that it does not include other constraints to ER, such as plant productivity, soil moisture, and nutrient limitations (Jagermeyr et al. 2014). In addition, although the biochemical processes involved in the two main components of ER (i.e., autotrophic and heterotrophic respiration) have been studied quite extensively (Atkin and Tjoelker 2003; Sitch et al. 2003; Wehr et al. 2016), measuring these component fluxes separately from an ecosystem is challenging, mainly due to the difficulty in their direct measurement. The EC technique does not provide estimates of the ER components, and therefore the satellite-derived LST can only be used to directly estimate ER.

A few recent studies have extended the LST-ER relationships to include a wider range of ecosystem functionalities and parameters for improving ER estimates using remotely sensed data. Wu et al (2014) found that the nighttime LST, when combined with NDVI, was strongly correlated with ER (R^2 = 0.86) of aspen, black spruce and jack pine stands in Saskatchewan, Canada and the NDVI was an important driver of ER, confirming the connection between photosynthetic activities and both AR and HR (Wu et al. 2014). Similarly, Gao et al (2015) developed an ER model by assuming that one part of ER is derived from the current photosynthate with the respiratory rate coupling closely with GPP, and the other part of ER is derived from reserved ecosystem organic matter, with the respiratory rate responding strongly to temperature change. Their model was driven by MODIS-derived EVI, NDWI, and LST and

753 explained 93% of the variance in EC-derived ER for temperate mixed forest, temperate steppe,
754 alpine shrubland, alpine marsh and alpine meadow-steppe in Northern China and the Tibetan
755 Plateau (Gao et al. 2015). In another study, ER was modeled as an exponential function of soil
756 temperature and moisture and the model output explained up to 82% of the variance in the EC-
757 derived ER of a temperate deciduous broadleaf forest in Ozark, Missouri (Huang et al. 2014).
758 More recently, six different process models were used to examine the LST-ER relationships of
759 global terrestrial vegetation, showing that the LST-ER response curves largely displayed
760 exponential trend of respiration rates with increasing temperature, although the exact forms of
761 the relationships varied among the models (Ai et al. 2018). Based on this finding, Ai et al (2018)
762 combined the EVI of global vegetation types in their models to incorporate the effects of
763 vegetation on respiration and developed models of reference respiration, which was capable of
764 capturing the spatial and temporal patterns of ER at the global scale.

765 Since the first publication showing the promise of estimating ER from satellite-derived LST
766 (Rahman et al. 2005), most studies on this topic have used semi-empirical methods to correlate
767 ER with LST. As mentioned above, a few recent studies have attempted to utilize the LST in
768 process-based models in order to estimate ER of larger areas and diverse ecosystems. Further
769 improvement on incorporating satellite-derived LST in the process-based ER models would
770 allow the use of LST in operational models for routinely deriving ER values for global
771 ecosystems. The finer-resolution LST data derived from Landsat have not been used to estimate
772 ER yet. Recent studies have addressed the generation of consistent LST data from Landsat
773 imagery and estimating their uncertainties (Fu and Weng 2016; Laraby and Schott 2018). Studies
774 are needed to explore whether a smaller pixel of LST (such as 30 m of Landsat vs. 1 km of
775 MODIS) data would lead to better ER estimates, particularly in heterogeneous regions. It should

776 be noted that the overpass time (around 10am) is not perfect to studying LST and thereby ER.
777 The AVHRR provides routine LST data of global coverage (1.1 km, two passes each day), and
778 Terra and Aqua MODIS together offers global daytime and nighttime LST measurements for
779 four different times of the day. ASTER provides 90 m resolution LST data every 16 days, but
780 these data are available free of charge. Landsat 9, which has been fast-tracked for a December
781 2020 launch, will have a Thermal Infrared Sensor 2 (TIRS-2) with two TIR bands onboard which
782 will enable consistent retrieval of LST. Use of thermal sensors onboard unmanned aerial vehicles
783 (UAV, or drones) will be able to provide high resolution, near surface LST measurements for
784 studying ER at detailed spatial scales and on-demand temporal intervals. The NOAA's
785 Geostationary Operational Environmental Satellites (GOES) provide routine LST data (4 km,
786 once every 15 min) for North America and South America,. These GOES LST data can
787 potentially be used to examine the diurnal cycles of ER. The ECOsystem Spaceborne Thermal
788 Radiometer Experiment on Space Station (ECOSTRESS) launched on June 29, 2018 has the
789 diurnal sampling capability, and the resulting LST imagery (70 m × 70 m spatial resolution) can
790 also potentially be used to study the diurnal variations of ER.

791 **4.7. Quantifying NBP using atmospheric inversions**

792 NBP, the net carbon exchange between ecosystems and the atmosphere, can be quantified using
793 remotely sensed column CO_2 concentrations. CO_2 is a passive tracer in the atmosphere: it has no
794 chemical sink there and is only absorbed at the Earth's surface, by oceans and the terrestrial
795 biosphere. This characteristic, for instance, prevents defining a lifetime for CO_2 (Tans 1997).
796 Marginal sources in the atmosphere from the oxidation of reduced C (Folberth et al. 2005) and
797 from aircraft contribute to the increase of its concentrations, while respiration from the
798 biosphere, outgassing from the oceans and the volcanoes, fires and anthropogenic sources have a

much larger impact altogether (Ciais et al. 2013). Air motions therefore directly relate these various sources and sinks, termed "fluxes" hereafter, to the CO_2 concentrations that are observed in the atmosphere. This link is not a bijection and inverting it is meaningful only from a statistical point of view. Inversion is usually performed by assimilating the observed CO_2 concentrations into a numerical transport model under the constraint of some prior estimation of the fluxes and within a Bayesian framework (Peylin et al. 2013). Such an approach has been developed in the 1990s for the interpretation of measurements from the surface air sample networks (Enting et al. 1995), but sparse measurement coverage, particularly in low or high latitudes and over the oceans, limited the flux information content and motivated the extension of the approach to satellite observations of the CO_2 column (Rayner and O'Brien 2001).

Initial satellite studies focused on partial columns above the planetary boundary layer retrieved from radiances measured in the TIR wavelength by orbiting sensors that were designed for other purposes like meteorology (Chevallier et al. 2009; Nassar et al. 2011; Chevallier et al. 2014): High resolution Infrared Radiation Sounder-2 (HIRS-2) (Chedin et al. 2003), Atmospheric Infrared Sounder (AIRS) (Engelen et al. 2004) and Tropospheric Emission Spectrometer (TES) (Kulawik et al. 2010). Only Nassar et al. (2011) found the impact of the assimilation of such data (TES in this case) positive, and only by assimilating it jointly with measurements from the surface network. In general, these early attempts were hampered by systematic errors in the retrievals and in the transport models (particularly for vertical motion) of various amplitudes. The variability of the CO_2 column over the globe and over a year is of the order of 10‰ of the CO_2 dry air model fractions and most of it is already known: the useful signal is of the order of 1‰ of the retrieval value (Chevallier et al. 2005) and ideally should not be obscured by similar errors.

These issues have been reduced by optimizing the sensors for atmospheric inversion. Appropriate choice of the wavelengths in the SWIR rather than the TIR range extended the column retrievals to the planetary boundary layer, close to the surface fluxes, in sunlit and cloud-free areas, and therefore relaxed the constraint on the accuracy of the transport model a bit. It also allowed better identification of the CO_2 signal in the measured spectrum with respect to the signals from other atmospheric constituents or from the surface, therefore reducing the retrieval systematic errors. This evolution was started by SCIAMACHY on-board EnviSat operated from 2002 until 2012, and has been continued by TANSO-FTS on-board GOSAT in 2009 (still being operated, and is followed by GOSAT-2 launched in October 2018), and by NASA's OCO-2 in 2014 (still being operated). Similar data from three recent Chinese satellites (e.g., TanSat) were not as widely available at the time of writing, but more instruments are being planned in the USA, Asia and Europe. Residual systematic errors in the SWIR retrievals are further damped by empirical bias-corrections against reference retrievals from ground-based spectrometers (Wunch et al. 2011), even though these reference data themselves have non-negligible absolute uncertainties (Wunch et al. 2010). Transport models have progressed on their side with increased horizontal and vertical resolutions, better meteorological analyses and improved parameterization of subgrid-scale processes (Locatelli et al. 2015; Krol et al. 2018).

A few inverse modeling studies attempted to document the natural surface fluxes at regional to global scales using these SWIR retrievals (Basu et al. 2013; Reuter et al. 2014), specifically for extreme events such as the 2010 summer heat wave in Eurasia (Guerlet et al. 2013), the 2011 La Niña episode in Australia (Detmers et al. 2015), and the 2015-2016 El Niño episode in the Tropics (Liu et al. 2017). Yet these studies have been paralleled by intercomparison exercises between inversions, or with aircraft data or C inventories that questioned the reliability of

845 existing satellite-based CO_2 inversions (Chevallier et al. 2014; Reuter et al. 2017). Kondo et al.
846 (2015) examined global NBP (**Figure 7**) derived from the inversion of atmospheric CO_2
847 concentrations retrieved by GOSAT SWIR spectra, and found large differences in the NBP with
848 flux estimate derived from a bottom-up approach.

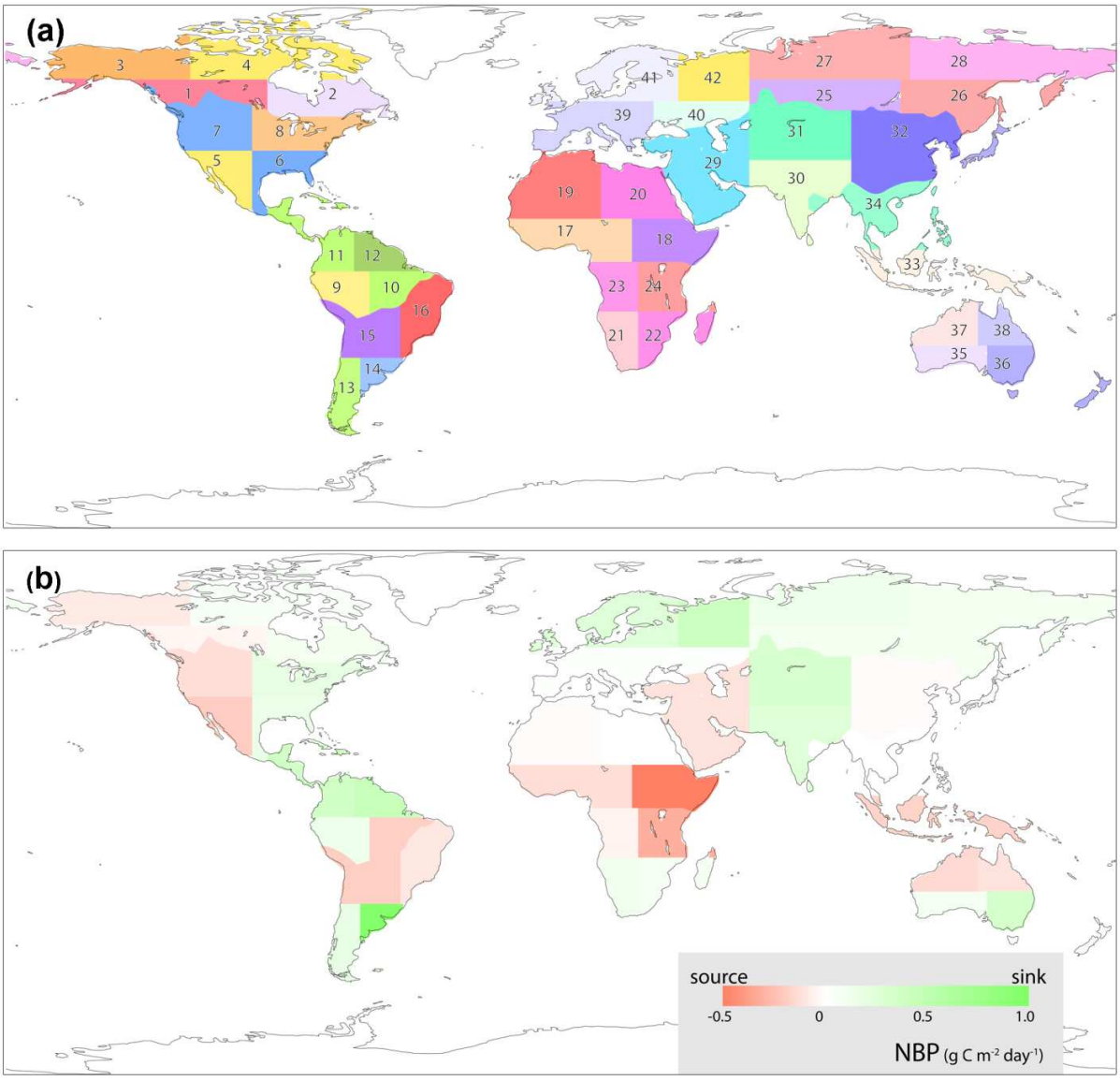

849

850 **Figure 7**. Annual NBP estimates based on GOSAT L4A, a flux product derived from GOSAT
851 atmospheric CO_2 concentrations with Bayesian inverse modeling: (a) terrestrial regions (i.e., tiles) used
852 for the development of the GOSAT L4A product; (b) mean annual NBP over the period 2000-2014.

853

854 The much increased scientific visibility of CO_2 remote sensing (Eldering et al. 2017),
855 manifests the fact that the accuracy of the CO_2 retrievals and of the transport models is
856 approaching the levels needed to constrain the fluxes from the natural biosphere (Buchwitz et al.
857 2017) despite all residual uncertainties in the end-to-end processing chains. The remote sensing
858 of CO_2 has defined unprecedented quality standards in the monitoring of the Earth's atmosphere.
859 The technical challenges have been taken up by major space agencies, while the various levels of
860 the processing chains are being developed by a growing scientific community. The current lack
861 of routine reference CO_2 column observations with systematic errors less than 1‰ is a hard limit
862 (WMO/IAEA 2016) that, e.g., the development of in-situ vertical light profile measurements
863 may erase in the future (Karion et al. 2010). In the meantime, a collective approach is needed,
864 where diverse radiative transfer and transport models, several satellite instruments and some of
865 the related data described in the other sections are used to identify and interpret the robust signals
866 in the satellite-based atmospheric inversions.

867

868 **5. Remote sensing of carbon stocks**

869 Remote sensing has been widely used to quantify biomass carbon stocks at regional to global
870 scales since the early 1990s. Biomass C stock has been estimated using passive optical remote
871 sensing data, microwave remote sensing data, and lidar remote sensing data. Carbon stocks in
872 soils have also been quantified using remote sensing, mainly for croplands and at relatively small
873 spatial scales.

874 **5.1. Passive optical remote sensing of biomass**

875 AGB has been frequently estimated from passive optical remote sensing that is particularly
876 sensitive to vegetation canopy properties. Passive optical satellite observations with a wide range

of spatial resolutions have been applied for estimating AGB. The coarse-resolution data (250m - 8000m) (e.g., AVHRR, SPOT, and MODIS) are often used to estimate biomass at regional or global scales for various ecosystems such as forests (Dong et al. 2003; Zhang and Kondragunta 2006; Chopping et al. 2011), grasslands (John et al. 2018), and Arctic tundra (Epstein et al. 2012). The medium spatial resolution data (~30m), mainly from Landsat TM/ETM+/OLI, Sentinel-2 Multispectral Imager (MSI), and Terra/Aqua ASTER, are perhaps the widely-used optical remote sensing data for biomass estimation at local and regional scales for different ecosystems such as forests (Fazakas et al. 1999; Turner et al. 2004; Sibanda et al. 2015), grasslands (Friedl et al. 1994), and shrublands (Shoshany and Karnibad 2011). The high spatial resolution data (< 5m), including high-resolution satellite imagery on QuickBird (2.44m in multispectral and 0.61m in panchromatic), IKONOS (3.2m in multispectral and 0.82m in panchromatic), and WorldView-2/3 (1.85m in multispectral and 46cm in panchromatic), are commonly used to calculate local tree biomass (Leboeuf et al. 2007; Palace et al. 2008; Fuchs et al. 2009) and grass biomass (Sibanda et al. 2017).

The variables derived from passive optical remote sensing for biomass estimation mainly consist of spectral reflectance, VIs, spatial texture, and vegetation canopy attributes. Spectral reflectances are the simplest variables, which vary from visible to SWIR wavelength. VIs are more frequently used in biomass estimation because they can enhance green vegetation signals and minimize the impacts from soil background, sun-canopy-sensor geometry, and atmosphere (Huete et al. 1985). The commonly used VIs are NDVI, EVI, Simple Ratio (SR), middle infrared (MIR) index, chlorophyll based difference index, and tasseled cap (TC) transformation or principal component analysis (PCA) of spectral bands. Spatial texture of spectral or panchromatic bands, which describes the spatial characteristics of images and identifies objects

900 or regions in images, has also been used for biomass estimation (Sarker and Nichol 2011).
901 Canopy spatial texture is scale dependent, which can be calculated using a 3 × 3 window size or
902 Fourier Transform Textural Ordination (FOTO) method from very high spatial resolution
903 imagery (Eckert 2012; Dube and Mutanga 2015b; Ploton et al. 2017).

904 Moreover, vegetation canopy attributes derived from optical satellite data can be used as
905 effective predictors of AGB. The frequently used attributes include LAI, canopy structure, and
906 tree shadow fraction. LAI, an important biophysical factor regulating photosynthesis,
907 evapotranspiration, and C fluxes, has been estimated from spectral VIs based on either empirical,
908 regression models (Heiskanen 2006) or radiative transfer (RT) algorithms (Myneni et al. 1997b).
909 Canopy structure is generally quantified using biophysical parameters (e.g., tree crown size/area,
910 height, and density), and both foliage biomass and total standing biomass are related to these
911 parameters (Franklin and Hiernaux 1991; Wu and Strahler 1994). Canopy reflectance models
912 have been used to estimate the crown size and density within each grid cell. The Li–Strahler
913 geometric-optical (GO) model is a widely used canopy reflectance model (Li and Strahler 1985).
914 Shadow fraction can also be quantified from medium-resolution satellite imagery (e.g., Landsat
915 TM/ETM+) using spectral mixture analysis (SMA) (Hall et al. 1995) and from high-resolution
916 satellite imagery using a digital value threshold approach (Leboeuf et al. 2007). Although it is
917 not a biophysical forest attribute, shadow fraction has proven useful for the estimation of forest
918 biomass (Greenberg et al. 2005).

919 AGB is generally estimated by empirically or functionally relating to satellite-derived
920 variables based on empirical models (regression or machine learning approaches) and physically-
921 based allometric models. Simple regression models are established by associating a single VI or
922 spectral reflectance to field biomass measurements (Roy and Ravan 1996; Calvao and Palmeirim

923 2004; Heiskanen 2006). The simple linear model format could also be transformed from
924 logarithmic or exponential functions. The model coefficients can be estimated with the ordinary
925 least-squares approach by assuming that independent variables have high accuracy or the
926 reduced major axis regression method by assuming that both dependent and independent
927 variables have significant uncertainties (Larsson 1993; Powell et al. 2010). Although the simple
928 model is widely applied to estimate AGB in a local region, the model accuracy and optimal
929 independent variables vary with spectral variable and local environment (Roy and Ravan 1996;
930 Foody et al. 2003; Lu et al. 2004). Further, the simple regression models could also correlate
931 biomass to shadow fraction from high resolution imagery (Jasinski and Crago 1999; Leboeuf et
932 al. 2007) and to the LAI in the logarithmic relationships (Saatchi et al. 2007; Madugundu et al.
933 2008).

934 A multiple regression model is able to improve biomass estimates by combining surface
935 reflectance, VIs, and biophysical variables (Zheng et al. 2004; Hall et al. 2006). Multiple
936 regression analyses can be performed in three different ways. First, the multiple regression from
937 the ordinary least-squares approach typically includes all explanatory variables regardless of the
938 strength of the relationship between each variable and biomass. Second, stepwise regression
939 analysis can be used to identify the most important explanatory variables for the final model
940 based on their relative contributions. Third, the canonical correlation analysis can maximize the
941 correlation among variables and align spectral bands with the variation in biomass (Heiskanen
942 2006) and therefore allows multiple regression analysis in a simple and linear way (Cohen et al.
943 2003). A variety of multiple regression models have been used to estimate biomass (Lu 2005;
944 Saatchi et al. 2007; Powell et al. 2010; Eckert 2012; Dube and Mutanga 2015b), while the

945 variables used vary among studies and it is still challenging to identify the optimal variables for a
946 given study.

947 The machine learning algorithm or non-parametric approach has been widely used in recent
948 biomass estimation efforts. Unlike regression methods, this approach can easily handle a large
949 number of explanatory variables derived from remotely-sensed and ancillary data that are
950 linearly or nonlinearly related to biomass. The commonly used machine learning algorithms
951 include neural networks (Foody et al. 2001) and regression trees (John et al. 2018). The machine
952 learning approaches have been established for estimating AGB using time series of MODIS
953 reflectance with ancillary data (including climate and topographic variables) in large regional
954 areas for forests in California (Baccini et al. 2004), Africa (Baccini et al. 2008), and Russia
955 (Houghton et al. 2007), and across the conterminous U.S. (Blackard et al. 2008) and for
956 grasslands in Mongolia and Inner Mongolia (John et al. 2018). Similarly, machine learning
957 approaches, particularly random forest (Breiman 2001), are also established using other optical
958 satellite observations (such as Landsat TM/OLI, Sentinal-2 MSI, and Woldview-2) and spectral
959 variables to calculate biomass at regional scales (Powell et al. 2010; Dube and Mutanga 2015a;
960 Karlson et al. 2015; Pandit et al. 2018). In general, the regression tree approach has advantages
961 over other models in producing consistent estimates with smaller errors (Powell et al. 2010).

962 Allometric model is a physically-based approach and has been widely used for the estimation
963 of forest AGB. It converts the measurements of tree variables (e.g., canopy crown size, crown
964 depth, diameter at breast height or DBH, and tree height) to AGB based on field observations
965 (TerMikaelian and Korzukhin 1997). The allometric models for biomass estimation are in
966 various forms (Pastor et al. 1984; TerMikaelian and Korzukhin 1997), and AGB is most
967 commonly estimated as a power function of DBH. Although the specific forms of allometric

968 models vary with species and site, generalized allometric models have also been used for
969 biomass estimation across large regions dominated by mixed species (Jenkins et al. 2003; Wirth
970 et al. 2004).

971 Most vegetation attributes, particularly tree height and stem diameter, are hard to be retrieved
972 from passive optical remote sensing data, but canopy properties can be easily detected by optical
973 remote sensing data. A foliage-based allometric model was developed to associate AGB to
974 foliage biomass that is a function of satellite-derived LAI (Zhang and Kondragunta 2006). As a
975 result, the maximum LAI derived from 1 km MODIS LAI product (Myneni et al. 2002) was used
976 to estimate AGB across the conterminous United States after the allometric models were
977 established for needleleaf forests, broadleaf forests, and mixed forests, respectively (Zhang and
978 Kondragunta 2006). Moreover, a biomass allometric model based on satellite data was also
979 established with tree crown area. Allometric models are typically developed for coniferous and
980 deciduous trees separately using field measurements and linear least squares regression. Tree
981 crown area derived from the GO model (Soenen et al. 2010; Chopping et al. 2011), object-based
982 classification (Rasmussen et al. 2011), or high-resolution satellite data (Hirata et al. 2014) is used
983 to estimate forest biomass at regional scales based on general allometric models. This method
984 was used to estimate biomass in Canada from SPOT multispectral data and was shown to be
985 better than empirical approaches (NDVI or shadow fraction) (Soenen et al. 2010). Canopy
986 structure parameters were also retrieved from both MODIS and MISR data for the estimation of
987 biomass (Chopping et al. 2011).

988 Passive optical remote sensing provides perhaps the best tool for biomass estimation at
989 regional to global scales because of its global coverage, multiple spatial resolutions, repeat visits,
990 and cost-effectiveness. However, the satellite variables used in the developed empirical models

991 (regression or machine learning approaches) for AGB estimation vary greatly across various
992 regional environments and the models cannot be directly transferred across biomes and different
993 vegetation phenological stages of satellite observations. Further, it is difficult to evaluate the
994 relative performance of different models because of the complexity in AGB estimation. Satellite-
995 based allometric model is an alternative approach that estimates AGB based on vegetation
996 structural variables. It is challenging is to accurately retrieve vegetation canopy attributes from
997 passive optical remote sensing data. The spectral signal tends to saturate when biomass is high,
998 leading to underestimation of high biomass density and overestimation of low biomass density.

999 **5.2. Microwave remote sensing of biomass**

1000 Microwave remote sensing sensors include radiometers and scatterometers. The scatterometer is
1001 also referred to as an active sensor because it actively sends microwave pulses to the ground and
1002 measures the backscattered power, while the radiometer is referred to as a passive sensor because
1003 it passively observes the microwave radiance from the Earth and its atmosphere (Liu 2015). Real
1004 aperture radar (RAR) is a scatterometer that measures the range from the sensor to the target.
1005 The resolution of RAR depends on the pulse width in the range direction and the distance from
1006 the antenna to the target in the azimuth direction, while the beam width of the radar depends on
1007 both wavelength and the antenna size. In 1951, Carl A. Wiley found that a long antenna could be
1008 synthesized through the frequency analysis of Doppler shift of the signal reflected to the radar by
1009 the objects (McCandless and Jackson 2004). The synthetic aperture radar (SAR) was invented
1010 based on RAR using Wiley's findings. The first civilian spaceborne SAR was the one onboard
1011 the SEASAT which was launched in June 1978. Although the SAR onboard SEASAT only
1012 operated for a short period of time (e.g., ~100 days), this satellite opened a new era of remote
1013 sensing (Shi et al. 2012). Since then, several civilian SAR satellites have been placed in orbit by

National Aeronautics and Space Administration (NASA), European Space Agency (ESA), Japanese space Agency (JAXA), and Canadian Space Agency (CSA) for the observation of earth surface including both the sea and the land.

The wavelength or frequency of SAR is an important parameter for forest monitoring. The microwave with longer wavelength can penetrate deeper into forest canopies. The classic bands (frequency or wavelength) used by SAR in ascending order of wavelength include X-band (9.6G, 3.0cm), C-band (5.6G, 5.7cm), S-band (3.0G, 10cm), L-band (1.27G, 23.5cm), and P-band (0.435G,70.0 cm). The well-known SAR satellites include SIR-A (USA, L-band,1981), SIR-B (USA, L-band, 1984), ERS-1 (Europe, C-band 1991), ALMAZ (USSR,S-band, 1991), JERS-1 (Japan, L-band, 1992), SIR-C/X-SAR (USA, C-band, L-band; Germany, X-band, 1994), ERS-2 (Europe, C-band,1995), RADARSAT-1 (Canada, C-band,1995), SRTM (USA, C-band; Germany, X-band, 2000), ENVISAT (Europe, ASAR, C-band, 2002), ALOS/PALSAR (Japan, L-band, 2006), RADARSAT-2 (Canada, C-band 2007), TerraSAR-X (Germany, X-band, 2007), TanDEM-X (Germany, X-band, 2010), HJ-1C (China, S-band, 2012), ALOS-2 (Japan, L-band, 2014), and Gaofen-3 (China, C-band, 2016). Several new missions under preparation include BIOMASS (Europe, P-band, scheduled 2022), NISAR (USA, L-band; India, S-band, scheduled 2020), and TanDEM-L (Germany, L-band, scheduled 2022).

Microwave radar data is coherent signal with both amplitude and phase information and can be operated at various polarization, such as H (horizontal) and V (vertical) polarizations. Polarimetric SAR includes signals at quad-polarization (HH, HV, VH, and VV). The radar backscatter intensity (i.e., the power of the backscatter signal) at HV polarization was the first used for forest biomass estimation. In addition to the use of SAR backscattering intensity, the other use of SAR data includes SAR interferometry (InSAR) (Rosen et al. 2000),

Radargrammetry (Schanda 1985), Polarimetric SAR interferometry (PolInSAR) (Cloude and Papathanassiou 1998), and tomographic SAR (TomoSAR) (Frey et al. 2008). In the period of SIR-A and SIR-B, the information of earth surface was mainly extracted from the SAR image intensity. Radargrammetry is the application of photogrammetry (optical image) on SAR images. Radargrammetry can detect the vertical distribution of ground objects by measuring displacements of one object on two SAR images acquired with different view angles. Scientists insisted on the studies of radargrammetry from 1960s till recent years (G 1963; Vastaranta et al. 2014). In addition to terrain elevations, the improvement of spatial resolution of SAR images provided radargrammetry a new opportunity to capture the 3D structures of forest (Vastaranta et al. 2012). The InSAR data from SIR-C/X-SAR mission and tandem ERS-1 and ERS-2 was a milestone in the monitoring of forest using SAR data. They advanced studies of SAR interferometry, especially interferometric coherence, on the estimation of forest AGB. PolInSAR and TomoSAR can directly detect the 3D structure of forest and provide a new technique for monitoring forest AGB. The new missions, including BIOMASS (Le Toan et al. 2011), NISAR (Rosen et al. 2016) and Tandem-L, have the work mode to acquire SAR data for PolInSAR and TomoSAR.

Spaceborne SAR can work at all time under all-weather conditions. Therefore, it has great potential for the estimation of forest AGB even over areas that are often covered by clouds or fog throughout the year. The estimation of forest AGB was initiated by two papers published in the early 1990s. Le Toan et al (1992) observed the strong correlation of L- and P-band SAR backscattering coefficients with red pine biomass. Dobson et al (1992) reported that the backscatter of polarimetric airborne SAR at P-, L- and C-bands was dependent on AGB of conifer forests. Following these two pioneering studies, many scientists estimated forest biomass

using multi-band and multi-polarization SAR data (Beaudoin et al. 1994; Rignot et al. 1994; Harrell et al. 1995; Kasischke et al. 1995; Pulliainen et al. 1996; Ranson et al. 1997; Ranson and Sun 2000; Sun et al. 2002; Ni et al. 2016). In addition to radar backscatter coefficients, interferometric coherence was also used to estimate forest AGB in the early 2000s (Luckman et al. 2000; Gaveau 2002; Santoro et al. 2002; Santoro et al. 2007). These studies showed that the SAR backscatter increased almost linearly with increasing biomass and then gradually saturates at high biomass level. The biomass saturation level depends on radar frequency with ~200 tons/ha at P-band and ~100 tons/ha at L-band, while the backscatter at the C-band is much less sensitive to biomass (Shi et al. 2012). For example, Yu and Saatchi (2016) examined the relationship between ALOS/PALSAR HV backscatter and AGB for tropical forests and temperate conifer forests, and found different relationships and different levels of sensitivity to AGB among the biomes (**Figure 8**). Neither the SAR backscattering coefficients nor the interferometric coherence is the direct measurement of forest AGB. Their strong correlation with AGB could be easily destroyed by environmental factors such as precipitation and soil moistures (Kasischke et al. 2011).

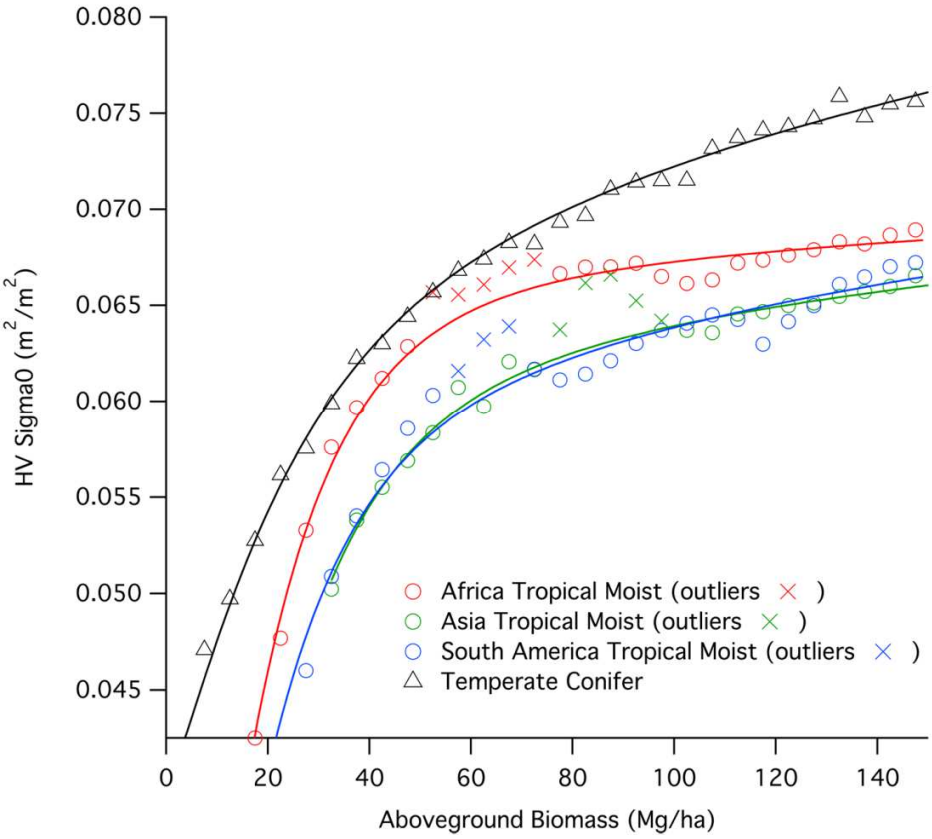

1075

1076 **Figure 8**. Relationships between bin-averaged means of ALOS/PALSAR HV backscatter coefficient
1077 (sigma-0) and AGB values of the middle of the bin for tropical moist forests (Africa, Southeast Asia, and
1078 Latin America) and temperature conifer forests. Solid lines stand for the regression lines between HV
1079 sigma-0 and AGB. For fitting purposes, outliers marked with x were excluded and bins above 155 Mg ha^{-1}
1080 were cut off for tropical forests. (Reproduced from Yu and Saatchi 2016)

1081

1082 Forest AGB is directly determined by four parameters: tree number, tree height, tree DBH,
1083 and tree species. Forest spatial structures are characterized by the first three parameters. The
1084 direct measurement of forest spatial structure using PolInSAR and TomoSAR data will be the
1085 final solution to overcome the saturation for accurate estimation of forest AGB. The PolInSAR
1086 and TomoSAR provide this kind of SAR techniques. PolInSAR makes compound use of the
1087 dependence of penetration capability of microwave on both frequency and polarizations, while

TomoSAR combines the penetration capability of microwave on frequency and view angles. Many studies have measured forest height using SAR imagery (Garestier et al. 2008; Minh et al. 2016; Khati et al. 2017). Currently, the dataset used in studies on PolInSAR and TomoSAR are acquired by airborne sensors. The advantages and disadvantages of PolInSAR and TomoSAR will be fully explored when the BIOMASS, NISAR and Tandem-L data are available in near future.

5.3. Lidar remote sensing of biomass

Lidar is an active remote sensing technology which determines the distance between the sensor and the target using laser energy. Lidar is able to provide accurate information on the vertical structure of forests through recorded discrete returns or waveforms (Lefsky et al. 2007; Pang et al. 2008; Simard et al. 2011). Discrete return lidar systems record several returns from each laser pulse. Waveform lidar systems record a continuous waveform with return signal as a function of time from sensor to target. By using different platforms, lidar data can be acquired from terrestrial, aircraft, and spacecraft lidar. These data can characterize the vertical information of forests at different scales varying from leaf, branch, individual tree, to large forest stands. **Figure 9** illustrates a typical workflow of deriving vegetation vertical structure and biomass from raw lidar data (Zhao et al. 2018b). Lidar data have also been used to estimate the biomass of other ecosystems such as shrublands (Li et al. 2017) and grasslands (Wu et al. 2009).

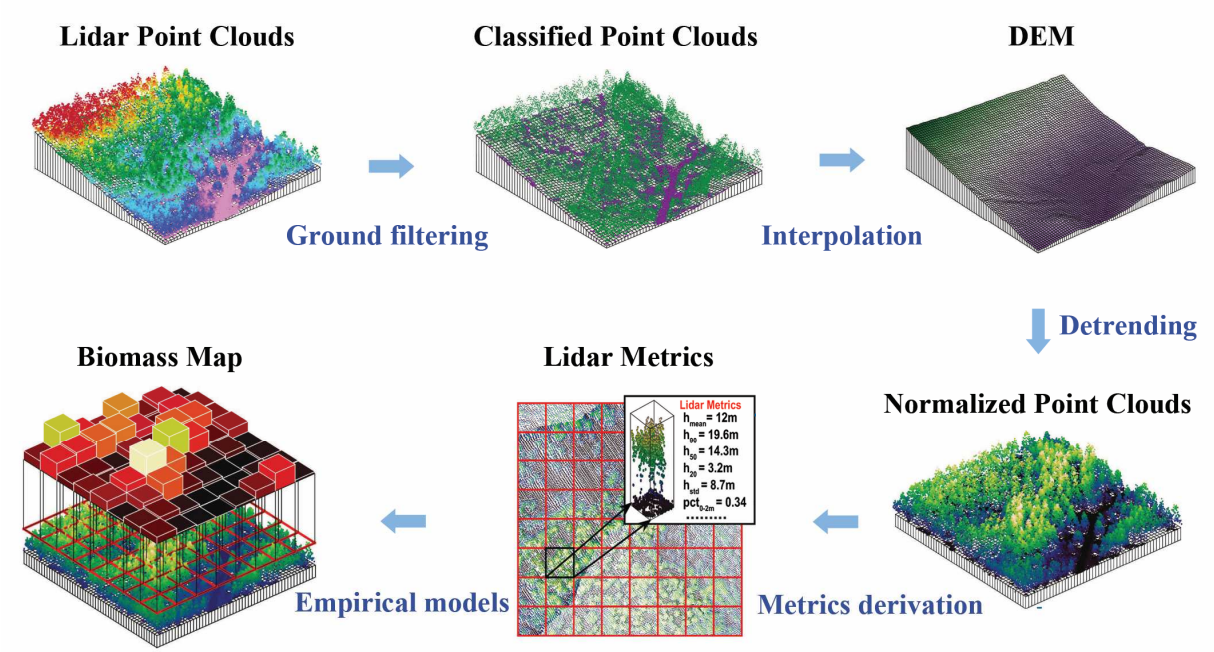

Figure 9. A workflow of deriving vegetation vertical structure and biomass from raw lidar data. Airborne discrete return lidar data are used as an example here, and a similar workflow applies to other types of lidar data. (Adapted from Zhao et al. 2018b)

The terrestrial laser scanning (TLS) sensor provides very dense point cloud data with millimeter intervals (Liang et al. 2016). After classification, TLS data can be separated into points from trunk, branch, and leaves for forests. Branch and foliage volume can then be estimated using shape information fitted from point cloud data (Hauglin et al. 2013; Stovall et al. 2017). This provides a non-destructive way to estimate AGB, even for allometric equation development (Kankare et al. 2013; Stovall et al. 2017). A more recent study showed how to produce quantitative 3D models of branch and trunk using quantitative structural models (Disney et al. 2018). These models improved the estimates of AGB especially for irregular tree stems. A recent study demonstrated the potential of this direct biomass estimation method for tropical forests (Rahman et al. 2017). Besides biomass estimation at individual tree level, forest biomass

or volume at stand level has also been successfully estimated using single-scan TLS data (Astrup et al. 2014; Liang et al. 2016).

Airborne laser scanners (ALS) has been increasingly used for biomass estimation. Strong relationships between laser data and AGB have been shown in many forests because of the capability of ALS to capture canopy height and density accurately. Through segmentation of canopy height model or point cloud data with high density, the ALS data can be used to quantify height, crown width, and crown volume that in turn can be used to estimate biomass at individual tree level (Popescu 2007; Tao et al. 2014). With the increasing availability of multitemporal ALS data, changes in tree level biomass can also be estimated, although correction of negative height biases might be needed (Zhao et al. 2018b). Recently, lidar data acquired from UAVs have also been used to estimate AGB of forests (Messinger et al. 2016) and grasslands (Wang et al. 2017) at landscape scales.

More operational applications at the stand level or large area make use of low point density ALS data. The lidar-derived height and density metrics are often used to build biomass estimation model with biomass data from field plots (Naesset and Gobakken 2008; Zhao et al. 2009; Pang and Li 2012). For example, Næsset and Gobakken (2008) investigated the relationship between forest biomass and canopy coverage using two groups of variables derived from lidar data which include quartile heights and crown densities. Zhao et al. (2009) estimated biomass using two scale-invariant models based on lidar-derived canopy height distributions and quintile functions, respectively. Pang et al. (2012) showed the benefits from species group stratification for component biomass estimation of stem, branch, and leaves. The airborne large footprint waveform data also showed good biomass estimates for a variety of forest types (Lefsky et al. 1999; Drake et al. 2002). Lefsky et al. (1999) estimated biomass of a temperate

deciduous forest using height indices from the Scanning LiDAR Imager of Canopies by Echo Recovery (SLICER) data. Drake et al. (1999) used the height of median energy from the Laser Vegetation Imaging Sensor (LVIS) data as a good index for biomass estimation in tropical forests. Recently, some studies also estimated biomass at the provincial or even national scale using ALS data (GOFC-GOLD 2016; Price et al. 2017). Price et al. (2017) proved that ALS data were helpful to estimate biomass of trees outside forest. The GOFC-GOLD recommended the use of ALS data for biomass estimation in local efforts in reducing emissions from deforestation and forest degradation (REDD+) (GOFC-GOLD, 2016). Lidar-based biomass surveys at regional scales may require less intensive field sampling than other remote sensing approaches.

Over the past decade, several spaceborne lidar sensors have been on-orbit. The main advantages of spaceborne lidar is the capability to collect data routinely for large regions or even globally. The Geoscience Laser Altimeter System (GLAS) aboard the ICESat satellite operated from 2003 to 2008. Lefsky et al. (2005) showed that it was feasible to estimate forest AGB using GLAS waveform data firstly. The GLAS data were then used to estimate biomass for pan-tropical forests (Baccini et al. 2008; Saatchi et al. 2011). The main limitations of spaceborne lidar systems are the spatial discontinuity and short operation period. Therefore, these discrete footprint biomass estimates are usually fused with estimates from other imagery remotely sensed data (e.g., MODIS, Landsat, and PALSAR) (Baccini et al. 2008; Saatchi et al. 2011; Sun et al. 2011).

With the development of lidar technology, more lidar data are becoming available from new generation systems like Advanced Topographic Laser Altimeter System (ATLAS) and Global Ecosystem Dynamics Investigation (GEDI). The ATLAS onboard ICESat-2 launched in September 2018 is a photon counting system using a micro-pulse, multi-beam photon counting

lidar that works at 532 nm (Markus et al. 2017). Compared to waveform data, the photon counting approach introduces abundant noise appearing in the atmosphere and even below the ground, making it difficult to extract the correct canopy and ground surface in vegetated areas. A few studies have been done to detect the noise and separate the signal, such as a recent novel methodological framework was developed to retrieve ground and canopy height using data from the Multiple Altimeter Beam Experimental Lidar (MABEL), an airborne simulator of ATLAS (Popescu et al. 2018). An approach that was tested with MABEL data by using local outlier factor algorithm modified with an ellipse searching area showed good performance not only in lower noise rate with relatively flat terrain surface but also for a quite high noise rate environment in relatively rough terrain (Chen, Pang, Li et al. 2019). These studies showed good performance for MABEL and simulated data, but further development of noise filtering is still necessary to explore vegetation applications for the new ATLAS data. A study to compare photon counting height metrics with both MABEL and discrete return lidar (DRL) has been done in savanna ecosystem (Gwenzi et al. 2016), showing moderate correlation between MABEL-derived height metrics and DRL-derived height metrics and weaker correlation between simulated ATLAS data with DRL indices. The GEDI system contains 3-laser system flying on the International Space Station (ISS), and the full waveform lidar has a circular footprint of ~25 m. Compared with GLAS system with 40 Hz frequency, GEDI will work with 242 Hz (Stavros et al. 2017). GEDI, launched on December 5, 2018, is the first spaceborne lidar mission that was specifically designed to study forests. GEDI will cover the geographical region between ~51. 6° N and S latitudes from the ISS. The availability of the lidar data from these spaceborne platforms will greatly facilitate the estimation of AGB at large scales.

5.4. Remote sensing of soil organic carbon

Laboratory spectral characteristics of soils in the Visible, NIR, and SWIR (VNIR-SWIR, 400-2500 nm) domain have been largely studied and described for decades (Ben-dor and Banin 1995; Ben-Dor et al. 1999; Rossel et al. 2006). The base line height and spectral shape are linked to soil physical features and absorption bands are linked to soil chemical features. For example, clay minerals produce an absorption band centred at 2200 nm due to the combination of vibrations associated with the OH and OH-Al-OH bonds (Hunt et al. 1971) and organic matter induces changes in spectral shape and absorption bands due to vibrations of O-H and C-H bonds linked to lignin and cellulose (Ben-Dor et al. 1997). Previous studies have then demonstrated that VNIR-SWIR spectral measurements acquired in laboratory conditions over soil samples can be used to accurately estimate several soil properties, such as soil organic matter (SOM) or SOC, Clay, Calcium Carbonate and Iron content (Chang and Laird 2002; Shepherd and Walsh 2002). For example, Shi et al. (2014) classified 1581 soil samples to clusters with different SOM content based on VNIR-SWIR spectra using a fuzzy clustering method, and found that the spectral reflectance of the soil clusters generally decreased with increasing SOM content (**Figure 10**).

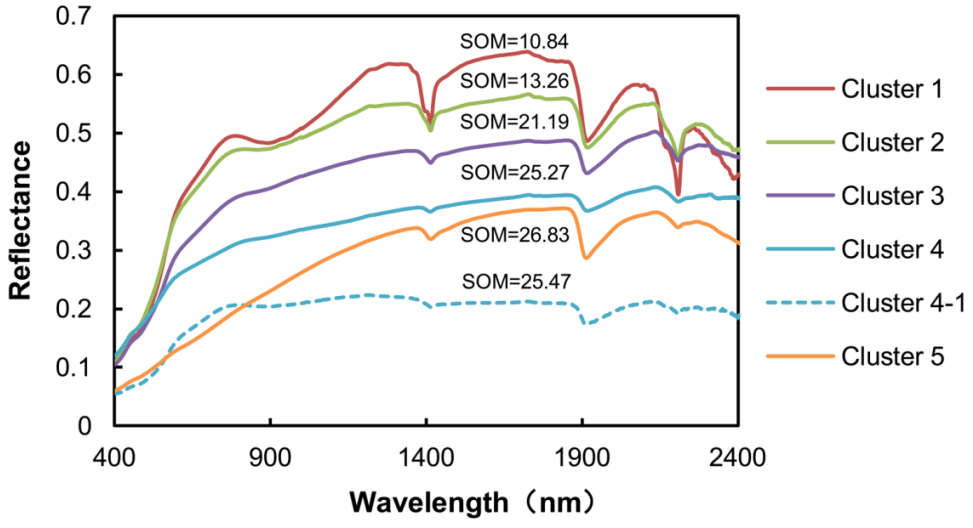

1206 **Figure 10**. Reflectance spectra of soil samples in different clusters with different soil organic matter
1207 (SOM) content. (Adapted from Shi et al. 2014)
1208
1209 The mapping of soil properties from VNIR-SWIR imaging data has followed encouraging
1210 results of laboratory VNIR-SWIR spectroscopy and is achieved by developing either
1211 SpectroTransfer Functions (STFs) models based on multivariate regression models (Gomez and
1212 Lagacherie 2016) or SCORPAN (*s*oils and/or soil properties, *c*limate and/or climate properties,
1213 *o*rganisms like flora and fauna and human activities, *r*elief settings, *p*arent material, *a*ge, and
1214 spatial coordinate *n*) models based on machine learning techniques (McBratney et al. 2003). The
1215 STFs models link the soil properties measured by conventional laboratory analysis (dependent
1216 variables) and the VNIR-SWIR spectra (predictor variables). The SCORPAN models link the
1217 soil properties measured by conventional laboratory analysis (dependent variables) and several
1218 environmental variables with the potential to explain the dependent variables (e.g., climatic data,
1219 topographic data, VNIR-SWIR spectra and spectral index). The STFs models are mainly based
1220 on multivariate regression methods such as the partial least squares regression and support vector
1221 machine (Gomez et al. 2008; Stevens et al. 2010). The SCORPAN models are mainly based on
1222 random forest and boosted regression trees (Wang et al. 2018). SFTs functions are developed and
1223 applied only for bare soils as soil surface components (such as the dry and green vegetation)
1224 affect imaging VNIR-SWIR measurements (Bartholomeus et al. 2011). SFTs functions are
1225 therefore developed for croplands during ploughing periods (Ben-Dor et al. 2002) and arid
1226 ecosystems (Jarmer et al. 2010). By contrast, SCORPAN models which use environmental
1227 variables indirectly linked to the SOC content and stock, may be applied for croplands,
1228 rangelands, shrublands and grasslands. The SCORPAN models therefore have higher mapping
1229 coverage potential than SFTs models.

The SOC content is a key soil property associated with soil physical, chemical and biological fertility. It is also related to soil structure and porosity maintenance. The first SOC content mapping effort based on remotely sensed data and SFTs models was conducted over croplands in Israel using reflectance data from an airborne hyperspectral sensor, the Digital Airborne Imaging Spectrometer (DAIS) (Ben-Dor et al. 2002). Then, several studies have successfully mapped SOC content at landscape and regional scales using VNIR-SWIR imaging data acquired by multispectral satellite sensors (Wilcox et al. 1994; Jarmer et al. 2010), hyperspectral Hyperion sensor aboard the Earth Observing-1 (EO-1) satellite (Gomez et al. 2008; Lu et al. 2013; Minu et al. 2017), and hyperspectral airborne sensors (Selige et al. 2006; Hbirkou et al. 2012). These studies had moderate to high performances in SOC content estimation, with Ratio of Performance to Deviation (RPD) from 1.4 to 2 and coefficient of determination (R^2) values from 0.5 to 0.8.

The SOC stock, the mass of C per unit area for a given depth (expressed in g C ha^{-1}), is a function of SOC content (expressed in g C kg^{-1} or %), bulk density (expressed in g cm^{-3}) and depth (expressed in cm) (Mishra et al. 2010). Some recent studies estimated SOC stock using SFTs models with laboratory (Rossel and Hicks 2015; Guo et al. 2019), field (Cambou et al. 2016), and imaging (Guo et al. 2019) VNIR-SWIR data. Two approaches were proposed to estimate SOC stocks with VNIR-SWIR spectroscopy. In a first approach, the SOC stock is estimated directly using a STF which links a set of SOC stocks measured by conventional laboratory analysis and a set of VNIR-SWIR spectra. In a second approach, each variable of SOC stocks (SOM, soil bulk density) is estimated by SFTs and then the SOC stocks are estimated using an equation which links the SOC stock to these variables (Mishra et al. 2010). The estimation of SOC stock using laboratory VNIR-SWIR spectroscopy had reasonable

performance (R^2 = 0.65, RMSE = 3.27 Mg C ha^{-1}). They also obtained moderate performances of SOC stock estimation using VNIR-SWIR imaging data (R^2 = 0.42, RMSE = 3.6 Mg C ha^{-1}).

Recent studies have mapped SOC content and stock using SCORPAN models and VNIR-SWIR satellite imagery data. For example, Wang et al. (2018) showed that the use of seasonal fractional cover data derived from VNIR-SWIR imagery data in association with classical environmental predictors (climate, lithology, relief and weathering covariates) improved the performance of SOC stock prediction. The VNIR-SWIR imagery data used for the estimation of SOC stock are mainly provided by MODIS (Mishra et al. 2010; Gray et al. 2015) and Landsat satellite sensors (Were et al. 2015; Yang et al. 2015a; Grinand et al. 2017; Schillaci et al. 2017; Wang et al. 2018). The VNIR-SWIR imagery from MODIS was also used for SOC content mapping (Ratnayakea et al. 2016; Somarathna et al. 2016). VNIR-SWIR imagery data can be used as spectral bands (Were et al. 2015; Ratnayakea et al. 2016; Grinand et al. 2017) or to generate biophysical variables or VIs such as percent vegetation cover (Gray et al. 2015) and NDVI (Mishra et al. 2010; Ratnayakea et al. 2016; Somarathna et al. 2016; Schillaci et al. 2017). These studies exhibited large variability in the performance of SOC stock estimation, with R^2 = 0.4 and RMSE = 3 Mg C ha^{-1} in semi-arid rangelands of eastern Australia (Wang et al., 2018) and R^2 = 0.72 and RMSE = 14.4 Mg C ha^{-1} in southeastern Madagascar dominated by forest, crop, and pasture (Grinand et al. 2017). Long-term satellite data (e.g., MODIS) can also be used to examine the trends in SOC (or SOM) at regional scales (Chen, Chang, Xiao et al. 2019).

6. Remote sensing of disturbance impacts on the terrestrial carbon cycle

Ecosystems can exhibit a range of responses to disturbances depending on disturbance type, severity (damage per area), timing, and ecosystem type, and these responses govern the type and

success of remote sensing methods employed. Key milestones for using remote sensing to study disturbance effects on C cycling began with the early use of satellite imagery to document disturbed areas, including deforestation (Stone et al. 1983) and wildfire (Turner et al. 1994). The development of global time series of VIs with AVHRR (Los et al. 1994) allowed the combination of satellite data with C cycle models (e.g., CASA) (Field et al. 1995) and longer studies of disturbance effects over large areas (Hicke et al. 2003). The availability of free Landsat imagery facilitated the assembly of large-scale, fine-resolution disturbance datasets (Masek et al. 2008; Hansen et al. 2013) as well as disturbance datasets key for C studies such as burned areas from the Monitoring Trends in Burn Severity (MTBS) project (Eidenshink et al. 2007). The development and release of MODIS products (e.g., LAI, GPP/NPP) have provided useful data globally in studying C cycling. More recent significant advances include the use of lidar data to estimate C stocks with high certainty and the use of remote sensing to scale net C fluxes from EC flux towers. Remotely sensed data offer substantial opportunities to incorporate disturbance information into C cycle studies (Frolking et al. 2009; McDowell et al. 2015).

Multiple attributes of disturbance (e.g., severity, timing) and C cycling (fluxes and stocks) can be studied with remote sensing. The area of disturbance is an important attribute (Senf et al. 2017) and can include damage to ecosystems (e.g., stress or canopy damage) or plant mortality. Widespread plant mortality is the largest disturbance effect on the C cycle and therefore one of the easiest to study with remote sensing. The loss of canopy (fires, storms, insects, disease, harvest) or change in needle or leaf color (fires, insects, disease) allows quantification of disturbance extent and severity. Changes in vegetation or soil color following burning also facilitates detection. Substantial (wildfires) or more subtle (insects, drought) changes in canopy temperature during and after disturbances may aid with detection. Disturbances across large

1299 regions that include a mix of disturbance types have been mapped (Masek et al. 2008; Cohen et
1300 al. 2016). More muted ecosystem responses and therefore decreased accuracy can result from
1301 lower mortality severity (e.g., background tree mortality). Finer resolution data (e.g., Landsat
1302 and finer) are better for detecting smaller disturbances than coarser resolution imagery (e.g.,
1303 AVHRR, MODIS), but data processing and storage requirements are substantially greater,
1304 precluding many analyses over broad regions. Remote sensing of disturbances that do not cause
1305 vegetation mortality (e.g., low or moderate drought or defoliation) is challenging. To address
1306 these challenges, methods that detect disturbances using imagery time series have been
1307 employed (Jepsen et al. 2009; Meigs et al. 2011a).

1308 Quantifying the magnitude of vegetation response or area of damage within a pixel provides
1309 additional information beyond a binary classification of disturbed/undisturbed. Often,
1310 information on disturbance type and therefore the response of vegetation is available from expert
1311 knowledge or ancillary data (e.g., aerial surveys documenting insect and disease damage or
1312 burned area datasets) and can aid the estimation of the fraction that a pixel is disturbed. Drought
1313 typically has a relatively large spatial footprint, and most vegetation within a satellite pixel is
1314 likely to experience similar stress. Some insect outbreaks (e.g., bark beetle outbreaks) kill trees,
1315 and therefore anomalous signals (from predisturbance conditions) can be translated into an
1316 estimate of the number of trees killed (Meddens and Hicke 2014). The MTBS dataset classifies
1317 burn severity into low, moderate, and high using Landsat imagery (Eidenshink et al. 2007). Other
1318 disturbance types, such as insect defoliation, prove more challenging to determine damage
1319 severity because a given reflectance signal may result from widespread low damage or
1320 substantial damage over a smaller area. The amount of damage within a pixel also determines the
1321 detectability of a disturbance. Meddens et al. (2013) found that accuracy of classifying trees

killed by bark beetles increases with fraction of pixel occupied by killed trees. Tradeoffs exist between spatial resolution and extent: very fine spatial resolution imagery (e.g., 1-2 m) can detect individual killed trees but have limited extent (e.g., Hicke and Logan 2009), whereas coarse-resolution imagery requires larger disturbances within a pixel but has global extent.

The timing and evolution of a disturbance are other important attributes. Repeated remotely sensed observations of a disturbance are often available either on a regular basis or for select times. Temporal resolutions can range from daily to yearly depending on the revisit time of the sensor and objective of the study. For example, active fire and burned area maps are produced globally as both daily (MOD14A1 and MYD14A1) and monthly (MCD64A1) MODIS products, respectively (Justice et al. 2002), drought monitoring is available at approximately two-week intervals (Hargrove et al. 2009), and insect outbreaks have been mapped at annual resolution (Meddens and Hicke 2014). Continental (Zhao et al. 2018a) and global (Hansen et al. 2013) time series maps of changes in forest cover have been produced from Landsat imagery. Spatiotemporal dynamics of individual events, or parts of events, can also be studied with remotely sensed data. Landsat time series are particularly valuable for slow-moving disturbances such as insect or disease outbreaks (Meigs et al. 2011a; Meddens and Hicke 2014). Remote sensing data are useful for estimating not only the immediate effects of disturbance but also the recovery rates of stocks and fluxes. For example, recovery of GPP following wildfires (Hicke et al. 2003) and bark beetle outbreaks (Bright et al. 2013) were studied using LUE models along with annual time series of AVHRR and MODIS imagery, respectively.

The impacts of disturbances on C fluxes can be estimated by combining satellite observations with models. LUE models have been used to compare predisturbance GPP and NPP estimated with satellite reflectances to postdisturbance values, including monitoring recovery

1345 rates (Hicke et al. 2003). A bark beetle outbreak caused a 5-26% decrease in MODIS-derived
1346 GPP, depending on mortality severity (Bright et al. 2013). Global fire emissions (C fluxes from
1347 combustion) were estimated to be 2.2 Pg C $year^{-1}$ during 1997-2016 by combining satellite-
1348 driven model estimates of C stocks and satellite-derived maps of burned area (van der Werf et al.
1349 2017) (**Figure 11a**). Net ecosystem fluxes following disturbances can also be estimated by
1350 upscaling EC flux tower data using satellite data (Xiao et al. 2011a; Schwalm et al. 2012). For
1351 example, hurricane Katrina led to a net carbon release into the atmosphere in the Gulf Coast
1352 region impacted by the disturbance (Xiao et al. 2011a) (**Figure 11b**). The early 2000s drought in
1353 western North America reduced the regional C sink by 30-298 Tg C yr^{-1} (Schwalm et al. 2012),
1354 and the 2006 drought had a greater effect across the conterminous US (Xiao et al. 2011a)
1355 (**Figure 11c**). Mechanistic ecosystem models can quantify modifications to C cycling following
1356 disturbance by using satellite-derived information on the extent and timing of disturbances
1357 (Meigs et al. 2011b).

1358 Estimating the amount of C stocks within disturbance areas has been accomplished with
1359 remote sensing in multiple ways (Frolking et al. 2009). Bright et al. (2012b) overlaid airborne
1360 optical imagery (for mapping disturbance area) on airborne lidar data (for estimating C stocks) to
1361 quantify the amount of C in lodgepole pines killed by mountain pine beetles (**Figure 11d**).
1362 Satellite imagery is needed for larger disturbance areas. Chambers et al. (2007) estimated the
1363 number of trees and associated C stocks affected by hurricane Katrina using spectral mixture
1364 analysis and Landsat and MODIS imagery. By combining Landsat imagery and field
1365 observations, Huang et al. (2010) estimated that drought-induced mortality of piñon-juniper
1366 woodlands resulted in a loss of 4.6 Tg C in an area in the southwestern US in the early 2000s.
1367 Hicke et al. (2013) used Landsat-based MTBS burn severity data and insect data from aerial

surveys in the western US together with a biomass map produced using MODIS imagery (Blackard et al. 2008) to estimate the amount of C in trees killed by wildfires and bark beetle outbreaks.

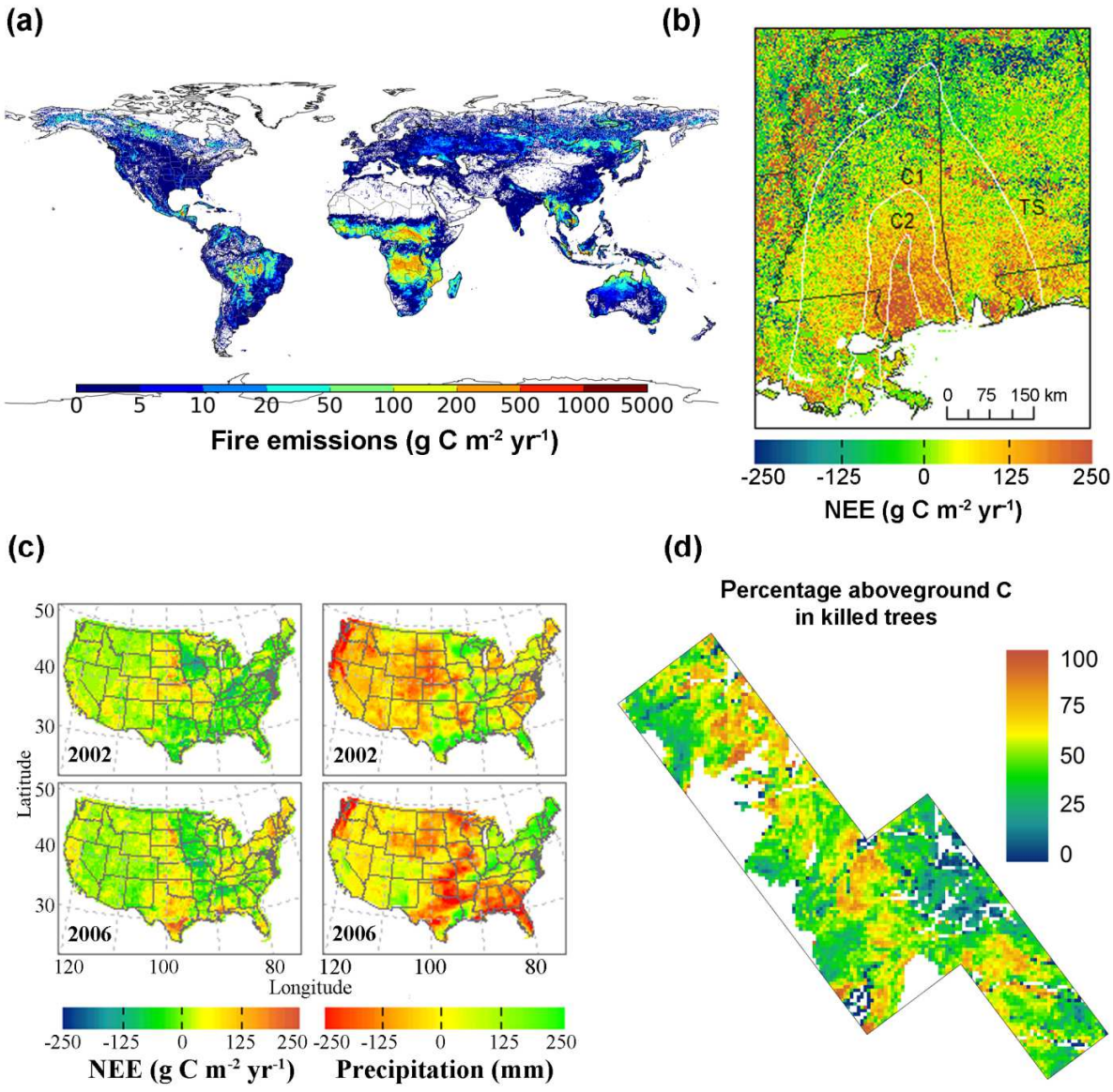

Figure 11. Illustration of remote sensing applications to assess carbon cycle impacts of different disturbance types with different methods across a range of spatial scales. (a) Use of satellite imagery and carbon cycle modeling to estimate mean annual combustion emissions from wildfires (g C m^{-2} $year^{-1}$),

1997-2016 (van der Werf et al. 2017). (b) Anomalies of annual NEE in 2006 relative to the 6-year period 2001–2006, indicating that hurricane Katrina led to a net C release into the atmosphere (Xiao et al. 2011a). The white lines indicate the isotachs, including tropical storm (TS), hurricane category 1 (C1), and hurricane category 2 (C2). (c) Drought effects (right column; precipitation anomalies from 1970-1999 means, mm) on annual NEE (left column; g C m^{-2} yr^{-1}) in 2002 (top row) and 2006 (bottom row) estimated by upscaling eddy flux covariance measurements with satellite remote sensing (Xiao et al. 2011a). (d) Integration of lidar data and aerial imagery to estimate the percentage of carbon stocks in trees within an area of a mountain pine beetle outbreak (Bright et al. 2012b).

Different sensors provide different capacities for studying disturbance effects on the C cycle. Sensors in the visible through shortwave infrared portions of the electromagnetic spectrum (e.g., Sentinel, Landsat TM/ETM+/OLI, AVHRR, and MODIS), are useful for quantifying the extent, severity, and timing of disturbances. Such sensors can detect changes in greenness as represented by NDVI, decreases in water content following plant stress or death, or changes in canopy (leaf area or color). Some of these satellites/sensors (e.g., Landsat, AVHRR, MODIS) have long time records, facilitating the study of a longer disturbance or ecosystem recovery. For instance, Meddens and Hicke (2014) used 16 years of Landsat imagery to document the spatiotemporal characteristics of a mountain pine beetle outbreak in Colorado, and Hicke et al. (2003) quantified NPP responses following using 17 years of AVHRR data. Emitted longwave radiation can also be used to identify disturbances. Plant stress and mortality results in a reduction or loss of cooling associated with transpiration, thereby raising surface temperatures (Heller 1968; Hesslerová et al. 2018). The MODIS LST product was combined with EVI to produce a Disturbance Index that takes advantage of this change in surface temperature (Mildrexler et al. 2007). Because of nonlinear relationships between canopy closure and biomass (or C) as well as

1399 confounding influences of green understory, challenges exist for using shortwave reflectances to
1400 estimate biomass following disturbances. Lidar data can facilitate biomass estimates (Frolking et
1401 al. 2009). Returns from ground-based, airborne, and space-based lidar systems (in the visible and
1402 NIR portions of the electromagnetic spectrum) has been used to estimate canopy height and
1403 volume (Dolan et al. 2011), and the resulting biomass estimates along with disturbance area can
1404 then be used to quantify the loss of C stocks (Bright et al. 2012a). For example, C stocks and
1405 recovery were assessed by mapping fires with Landsat imagery and estimating biomass with
1406 airborne lidar (Bolton et al. 2015).

1407 Despite the significant contribution of remote sensing to advances in the understanding of
1408 disturbance impacts on the C cycle, important challenges remain. Maintaining the continuity of
1409 existing long-term satellite records, especially Landsat and MODIS, is critical for providing
1410 additional understanding of this topic. Studies of future disturbances, trends in disturbances and
1411 their changes through time, and recovery following disturbances will benefit from continuing
1412 these records. Refinement and development of global, wall-to-wall mapping of disturbances at
1413 30-m spatial resolution and finer will increase the capability to separate disturbance types,
1414 leading to better estimates of immediate and legacy impacts on the C cycle. Imagery at fine
1415 spatial resolution and broad spatial extent is needed to map diffuse, low-severity disturbances
1416 that are nevertheless widespread across the landscape, such as background tree mortality (van
1417 Mantgem et al. 2009) and disease outbreaks (Sturrock et al. 2011). Continued development of
1418 translating disturbance area into C cycle variables (stocks and fluxes) is needed.

1419

1420 **7. Uncertainty and validation of carbon flux and stock estimates**

1421 **7.1. Uncertainty**

Estimates of C fluxes and stocks based on remote sensing can have significant uncertainty. One important source of uncertainty in C flux/stock estimates is the uncertainty of the remote sensing data products. For example, the satellite-derived surface reflectance, vegetation indices, SIF, and LAI have several sources of uncertainty such as atmospheric effects (e.g., Rayleigh scattering, ozone, aerosol, and water vapor content), retrieval errors, cloud contamination, and sensor degradation (van Leeuwen et al. 2006; Fang et al. 2012). Besides uncertainty associated with remote sensing data, C fluxes and/or stocks estimated from modeling approaches have two other main sources of uncertainty: model structure (e.g., incomplete or flawed underlying processes and assumptions) and model parameters (e.g., imperfectly or poorly defined parameters due to lack of information). For example, the uncertainty in meteorological data (Zhao et al. 2006), satellite-derived LAI data (Liu et al. 2018b), and land cover maps (Quaife et al. 2008; Xiao et al. 2011b; Zheng et al. 2018) can lead to significant uncertainty in regional C fluxes from LUE or diagnostic models. The uncertainty of model parameters can also lead to significant uncertainty in C fluxes in LUE and diagnostic models (Hilton et al. 2014; Xiao et al. 2014b). The biomass estimates have several sources of uncertainty: biases in field sampling, errors in plot locations, measurement errors in DBH and height, misrepresentation of allometric relationships or processes in models, errors in remotely sensed data, and imperfect retrieval methods (Lu et al. 2012). Friedl et al. (2001) attributed the uncertainty of remotely sensed data to three main sources: (1) errors introduced during the acquisition process of the observations, (2) errors generated by the processing of the remotely sensed data; (3) errors resulting from the scale mismatch between the grid cells of remotely sensed data and the scale of the ecological variables or processes of interest on the ground.

The uncertainty in remote sensing data products and the resulting C flux estimates can obscure the analysis or comparison of the magnitude, interannual variability, and long-term trends in vegetation productivity and C dynamics. As mentioned earlier, satellite-derived VIs are widely used as proxies of GPP, while LUE models, machine learning approaches, and diagnostic process-based models are more routinely used to quantify GPP. We used the GIMMS3g NDVI dataset based on AVHRR data (Pinzon and Tucker 2014), the EVI dataset based on MODIS data (Huete et al. 2002), the MODIS GPP product based on a LUE model (Running et al. 2004), GPP data from a diagnostic process-based model – BEPS (Liu et al. 2018b), and GPP data from a machine learning approach (EC-MOD) (Xiao et al. 2014a) to examine the trends in vegetation productivity in China from 2000 to 2014 (**Figure 12**). All these data products exhibited increasing trends, indicating that vegetation productivity had been increasing due to various factors (e.g., climatic warming, CO_2 fertilization, afforestation, and improved agricultural management practices). Despite the general agreement in the trends, the rate of increase was different between the two NDVI products (GIMMS3g NDVI and MODIS EVI) and among different GPP products (MODIS-GPP, BEPS, and EC-MOD), and there were also large discrepancies in total annual GPP among the three GPP products. Reducing the uncertainty in various remote sensing data products is essential for better understanding the dynamics of ecosystem C fluxes.

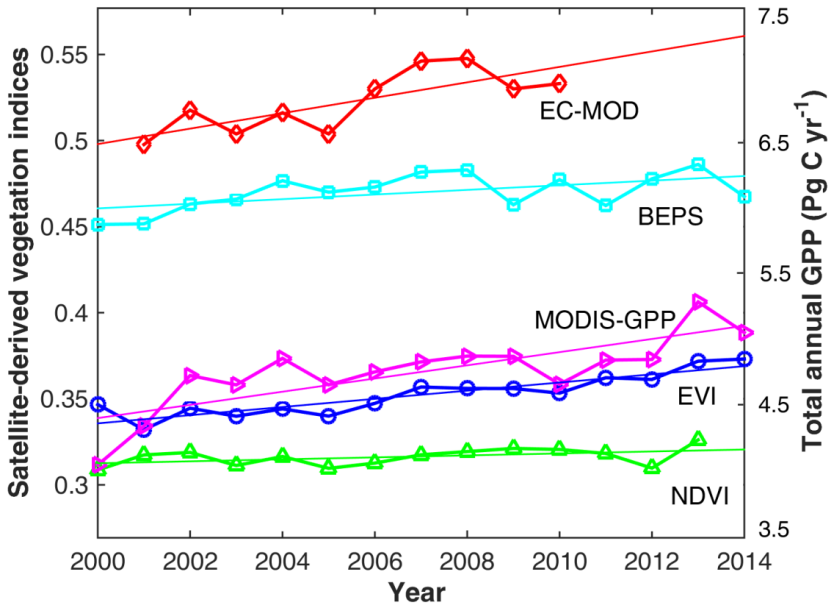

Figure 12. Trends of satellite-derived vegetation indices (VIs) and estimated GPP for China over the period 2000-2014. The VIs consist of GIMMS3g NDVI and MODIS EVI. Mean values averaged throughout the year are used for both NDVI and EVI. The EVI is multiplied by 2 for displaying purposes. The total annual GPP estimates are from a data-driven (or machine learning approach) – EC-MOD, a LUE model (MODIS-GPP), and a diagnostic process-based model – BEPS. The curves with symbols stand for annual mean NDVI, EVI, or GPP. The lines stand for the fitted trend lines: NDVI (y=0.00057x-0.83, R^2 =0.21,p=0.095), EVI (y=0.0012x-2.21, R^2=0.81, p<0.0001), MODIS GPP (y=0.049x-95.19, R^2=0.62, p<0.001), EC-MOD (y=0.058x-110.13, R^2=0.59, p<0.01), and BEPS (y=0.017x-28.93, R^2=0.31, p<0.05).

Similarly, the C stock maps based on different remote sensing data and approaches can exhibit significant discrepancies. For example, several forest AGB maps have been developed for the conterminous U.S. (**Figure 13**). Some maps are solely based on optical remote sensing data. For example, Zhang and Kondragunta (2006) developed an AGB map for North America using MODIS data streams (e.g., LAI, land cover, vegetation continuous fields) and foliage-based generalized allometric models. Blackard et al. (2008) developed an AGB map with 250 m

resolution for the U.S. from MODIS data (surface reflectance, NDVI, and percent tree cover), topographic variables, climate, and plot-level biomass data from the U.S. Forest Service's Forest Inventory Data (FIA) Program using a machine learning approach. Some other maps are based on optical and microwave remote sensing data. Wilson et al. (2013) developed a forest AGB map using FIA field data, environmental factors (e.g., temperature, precipitation), MODIS-derived vegetation phenology, and tree cover data based on Landsat. Some other studies, however, combined SAR and/or lidar data with optical remote sensing data. For example, Kellndorfer et al. (2013) developed a forest AGB map using biomass data from the USDA Forest Service FIA Program, high-resolution InSAR data from the Shuttle Radar Topography Mission (SRTM), and optical remote sensing data from Landsat ETM+ using an empirical modeling approach. The NASA-CMS map (Saatchi et al. 2012) is based on a multi-scale approach along with a variety of geospatial layers (e.g., ICESat GLAS, MODIS, PALSAR, climate, topography, Landsat disturbance, and Landsat LAI). The ICESat GLAS waveforms were linked to FIA-measured biomass via the Lorey's Height metric, and the biomass converted from waveforms were then used as training data for statistical models of biomass (Saatchi et al. 2012). Four maps (**Figure 13a-d**) had the highest AGB in the Pacific Northwest and intermediate values in the Appalachian Mountains and the Rocky Mountains regions, while the Zhang and Kondragunta map had similar AGB values in the Pacific Northwest and the Appalachian Mountains. The CMS map had higher AGB in the eastern U.S. and the Rocky Mountains than the other four products. The total AGB C stock ranged from 17.2 to 28.3 Pg C (**Figure 13f**). The Zhang and Kondragunta product had the highest total C stock, and the CMS product also had much higher C stock than the other products. Quantifying and reducing the uncertainty in remote sensing C stock products are

essential for assessing regional or global C storage and informing management and climate policymaking.

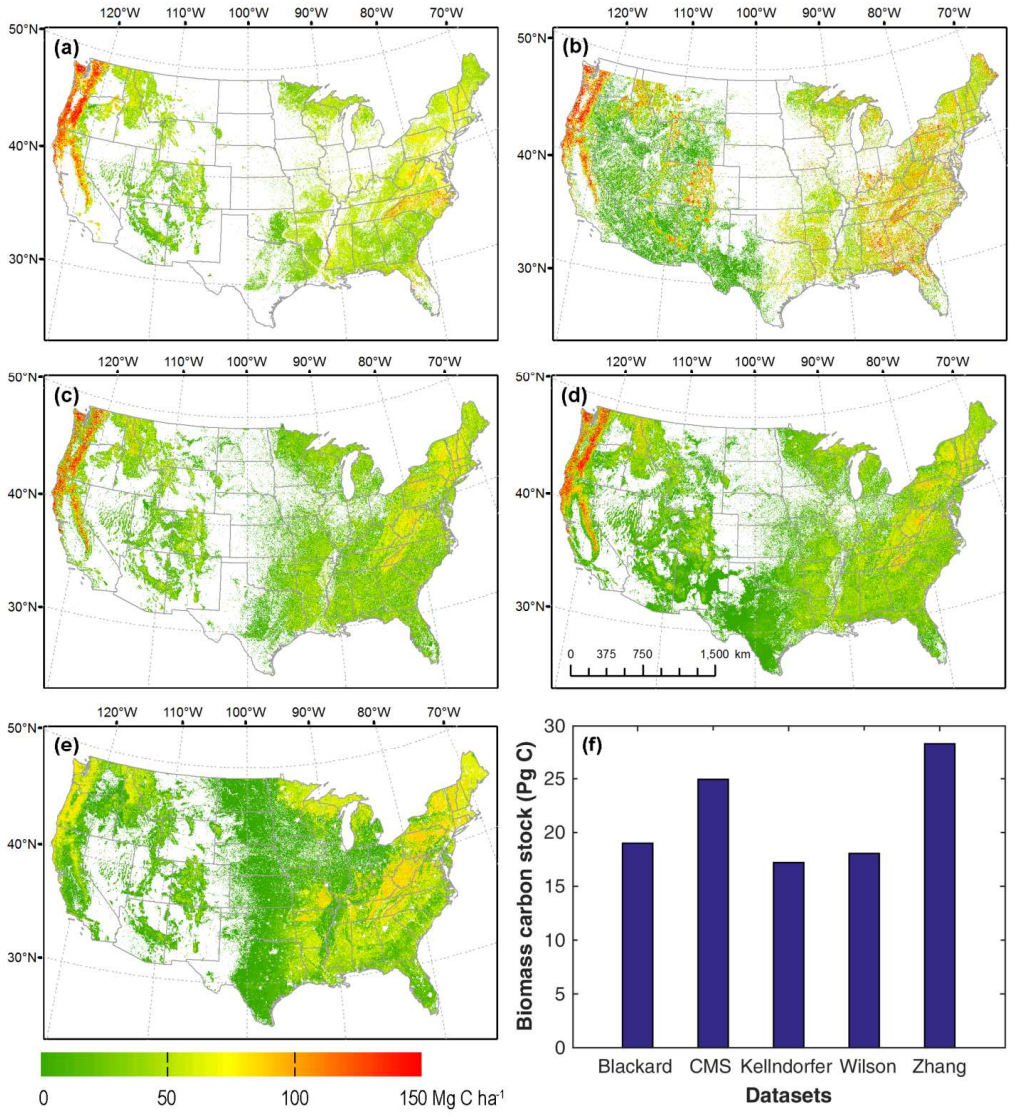

Figure 13. Forest aboveground biomass (AGB) carbon stock of the conterminous U.S. based on different datasets: (a) the Blackard et al. map; (b) the Carbon Monitoring System (CMS) map; (c) the Kellndorfer et al. map; (d) the Wilson et al. map; (e) the Zhang et al. map; (f) the total forest AGB carbon stock of the five products.

1508 Quantifying and reducing uncertainty in C flux and stock estimates remain a grand challenge.
1509 It is important to quantify the full uncertainty of these estimates by considering various sources
1510 of uncertainty. Future efforts are needed to pursue the quantification of the full uncertainty in C
1511 flux and stock estimates. Meanwhile, it is equally important to reduce the uncertainty in the
1512 estimates of C fluxes and/or stocks by using remotely sensed data with higher quality and finer
1513 resolution and better approaches.

1514 **7.2. Validation**

1515 The remote sensing of the terrestrial C cycle typically requires calibration and validation. Both in
1516 situ measurements and satellite/airborne data have been used to assess the accuracy of the C
1517 flux/stock estimates. C flux estimates have been typically validated using in situ measurements
1518 such as flux data from eddy covariance flux towers (Heinsch et al. 2006; Liu et al. 2018b) and
1519 NPP measurements. EC flux measurements from flux networks (e.g., FLUXNET, AmeriFlux,
1520 Fluxnet-Canada, EUROFLUX, USCCC) (Wofsy et al. 1993; Baldocchi et al. 2001; Xiao et al.
1521 2013) are perhaps the most accurate and most widely used data for validating carbon flux
1522 estimates based on remote sensing methods. For example, flux tower data from AmeriFlux and
1523 Fluxnet-Canada were used to develop and validate the data-driven approach based on MODIS
1524 data streams for the generation of the gridded, 1-km carbon flux product (GPP, ER, and NEP)
1525 over North America (Xiao et al. 2014a) (**Figure 14**). Besides the flux networks (e.g., AmeriFlux
1526 and FLUXNET), measurements have from other networks have also been to validate carbon
1527 fluxes. The Spectral Network (SpecNet) integrates remote sensing with carbon flux
1528 measurements (Gamon et al. 2010). The ES1309 (Innovative optical Tools for proximal sensing of
1529 ecophysical processes or OPTIMISE) Cost Action network aims at exploring optical observations
1530 from drones and airborne sensors with high spectral, spatial, and temporal resolutions to explore

1531 the links among light use, plant physiology and ecosystem functioning and to validate satellite
1532 missions such as Sentinel and the proposed FLuorescence EXplorer (FLEX) missions. The C
1533 stock (AGB or SOC) estimates are typically validated using plot-based C stock data (Lefsky et al.
1534 1999; Blackard et al. 2008; Sun et al. 2011).

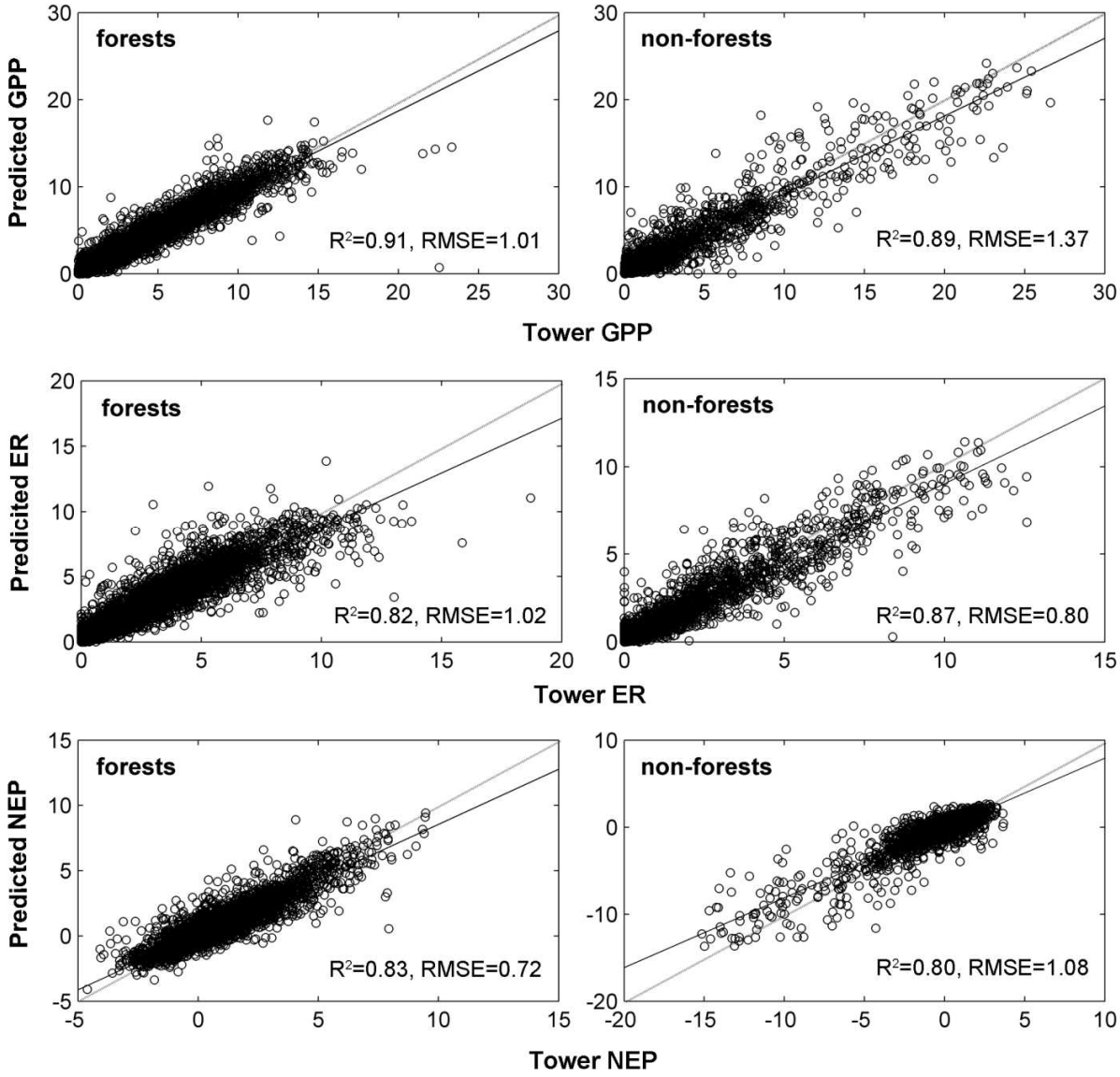

1535

1536 **Figure 14**. Cross-validation of a data-driven upscaling approach based on MODIS data streams for the
1537 development of gridded, 1-km carbon fluxes over North America with flux tower data from AmeriFlux
1538 and Fluxnet-Canada (Xiao et al. 2014a). Top panels: GPP for forests and non-forests; middle panels: ER

1539 for forests and non-forests; bottom panels: NEP for forests and non-forests ($p < 0.001$ for all cases). The
1540 units of GPP and RMSE are g C m^{-2} d^{-1}.

1541 However, the observations from satellite instruments often have medium to coarse
1542 resolution ranging from a few hundred meters to tens of square kilometers. Therefore there could
1543 be a moderate to large scale mismatch between the footprint of in situ measurements and the grid
1544 cell of satellite data, which makes it challenging to directly evaluate remotely sensed data using
1545 in situ measurements. For example, the ground area that a MODIS grid cell stands for is much
1546 larger than a field plot for in-situ LAI measurements, and to evaluate the MODIS-based LAI data
1547 products, gridded LAI estimates derived from finer-resolution satellite imagery (e.g., Landsat)
1548 have been used to bridge the gap between in situ measurements and MODIS-based estimates. A
1549 field plot is close to the grid cell of finer-resolution satellite data (e.g., Landsat) or airborne data,
1550 and the in situ measurements are used to calibrate/validate the satellite (or airborne) estimates
1551 that will then in turn be used to evaluate the estimates from medium- or coarse-resolution
1552 satellite data. This kind of calibration and validation framework was proposed to evaluate
1553 multiple MODIS data products (e.g., GPP/NPP, land cover, LAI) using field measurements in
1554 the Bigfoot Project (Cohen et al. 2006) (**Figure 15**). For example, the MODIS GPP and NPP
1555 products were validated using 30-m resolution GPP and NPP estimates driven by the Biome-
1556 BGC model and Landsat-derived LAI data (Turner et al. 2006). High-resolution satellite data and
1557 fine-resolution airborne and/or UAV data can bridge the gap between field plots or flux towers
1558 and satellite grid cells and help evaluate and validate satellite-derived C flux/stock estimates.

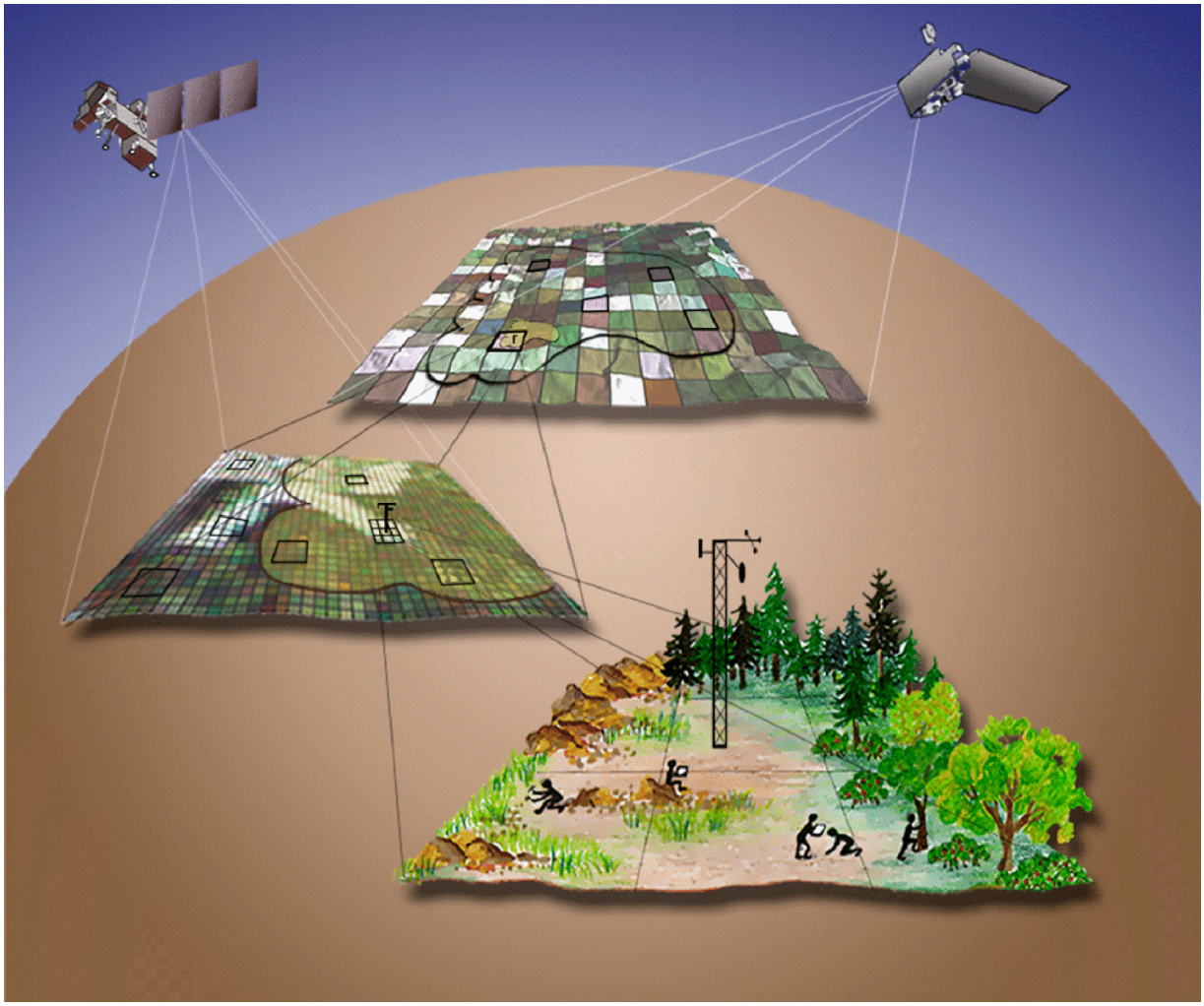

Figure 15. A framework for calibrating and validating carbon flux and stock estimates derived from satellite remote sensing using in situ measurements. Finer-resolution satellite or airborne data can bridge the gap between in situ measurements and medium/coarse resolution satellite data. (Reproduced from Cohen et al. 2006)

Field campaigns are an important component of NASA's Earth Observing System (EOS) and the evaluation and validation of remote sensing of the terrestrial C cycle. NASA has initiated a series of field campaigns over the last three to four decades. For example, the First ISLSCP (International Satellite Land Surface Climatology Project) Field Experiment (FIFE) (Sellers et al.

1988) was conducted at and around the Konza Prairie in Kansas in 1987 and 1989. The objectives of FIFE were to understand the processes regulating the exchange of energy, water, and carbon between the land surface and the atmosphere, develop and test remote sensing methods, and understand how to scale information and processes from the pixel or ecosystem level to regional scales. The Boreal Ecosystem-Atmosphere Study (BOREAS), a joint U.S.-Canadian effort, had field deployments in 1994 and 1996, aimed at quantifying the exchanges of carbon, water, and energy between the boreal forest and the atmosphere (Sellers et al. 1995). BOREAS collected and compiled remote sensing and ground-based (e.g., fluxes) observations. The Large Scale Biosphere-Atmosphere Experiment in Amazonia (LBA), one of the largest coordinated scientific endeavors in the tropics, started in 1998 (Nobre et al. 2001). One of the themes of LBA is carbon storage and exchange, and one of the strategies is to scale processes from small scales to the entire basin scale using models and remote sensing. The latest NASA field campaign is perhaps the Arctic-Boreal Vulnerability Experiment (ABoVE) in Alaska and western Canada that started in 2015 and is planned to last for 8 to 10 years (Kasischke et al. 2010). ABoVE seeks a better understanding of the vulnerability and resilience of arctic and boreal ecosystems to the changing environment. These field campaigns can help develop and refine methods for spatial and temporal scaling of field observation and evaluating remotely sensed data products.

8. Prospects for remote sensing of the terrestrial carbon cycle

8.1. Remote sensing of carbon fluxes

Key challenges and opportunities with the use of satellite-derived VIs in approximating or estimating ecosystem C fluxes involve the extension of the long time series data record, amidst

ever increasing space and time fidelity of the satellite data, including reduced uncertainties in geolocation, radiometry, and snow and cloud detection (Tucker et al. 2005). Continuity and extension of the satellite VI data record and other land products has recently been provided by the Visible Infrared Imaging Radiometer Suite (VIIRS) onboard NOAA-20, the first Joint Polar Satellite System (JPSS-1) launched in November, 2017 (Justice et al. 2013). The NASA/NOAA JPSS series will further extend our capabilities to examine long-term trends in ecosystem C fluxes and/or stocks. Geostationary data at 1 km pixel resolutions such as Himawari AHI (Advanced Himawari Imager) and GOES-R ABI (Advanced Baseline Imager) are now becoming widely available at sub-hourly time intervals and enabling improved precision of phenological time factors (e.g., budburst, full leaf expansion, dormancy) into ecosystem production models. Better understanding how flux tower data and VIs converge (e.g., Huang et al. 2019) will further reveal the underlying mechanisms of the C cycle (e.g., phenology and climate drivers) and help interpret satellite-derived greenness measures (Restrepo-Coupe et al. 2016).

Satellite phenology products, based on normalized bidirectional adjusted reflectances and a 2-band EVI (EVI2) have been developed for MODIS (MCD12Q2) and extended to VIIRS (Zhang et al. 2018a). There are also phenology metrics being derived from Landsat at 30 m spatial resolution (Melaas et al. 2016) enabling improved spatial-temporal scaling within heterogeneous landscapes, and ready upscaling of surface C measurements to larger landscape units and regional to global studies, which can constrain C cycle models. Ground-based phenocam networks can provide independent sources of land surface phenology information for comparisons and potential validation with satellite phenology products (Richardson et al. 2018).

Additionally, VIs can also play an important role in validating ecosystem responses to climate change. For example, Ichii et al. (2007) used an ecosystem model, BIOME-BGC, to

1615 determine which rooting depth could best estimate GPP based on the consistency between
1616 simulated GPP and satellite-based EVI seasonality and thereby to better simulate C, water, and
1617 energy cycles of tropical forests. Thus, although remote sensing can only directly monitor some
1618 topsoil properties, it can help parameterize models, and with extrapolated climatic data, make it
1619 possible to estimate whole ecosystem C exchange under conditions not yet encountered.

1620 The relationships between SIF and VIs and their relationships with photosynthesis (e.g., Li et
1621 al. 2018b, 2018c) should be examined at various timescales to exploit the complementary use of
1622 VIs with SIF and to better understand the interplay between direct photosynthesis process
1623 measures (SIF) and photosynthetic capacity measures (VIs). Plants respond to the dynamics of
1624 environmental variables through stomatal closure and other diurnal adjustments that cannot be
1625 easily sensed by VIs, and are more likely captured by SIF measurements. The Orbiting Carbon
1626 Observatory-3 (OCO-3) recently launched on May 4, 2019 has the diurnal but temporally
1627 fragmented sampling capability and its measurements will help understand the diurnal cycles of
1628 SIF and photosynthesis. At longer time scales, plants may increase leaf area and their
1629 photosynthetic capacity under favorable environmental conditions, and reduce LAI under stress
1630 when leaves are expensive to produce and maintain. Thus, at longer time scales, there would be a
1631 convergence of satellite greenness signals with biologic and structural canopy properties. Future
1632 research is needed to reveal whether SIF is able to detect plant stress almost immediately and can
1633 be effectively used for temporal remote sensing of vegetation photosynthesis.

1634 The discrete SIF soundings from OCO-2 and OCO-3 can be used to generate global, gridded-
1635 SIF estimates (e.g., GOSIF) (Li and Xiao 2019) with finer spatial and temporal resolutions using
1636 spatially and temporally continuous MODIS and meteorological data along with data-driven
1637 approaches. Moreover, newly operating and upcoming missions such as TROPOMI and

1638 the FLuorescence EXplorer (FLEX), respectively, will provide gridded SIF observations. The
1639 TROPOMI instrument aboard Sentinel-5P that was launched in October 2017 provides
1640 continuous SIF retrievals at 0.2° spatial resolution globally (Guanter et al. 2015a; Kohler et al.
1641 2018). The TROPOMI SIF product promises to lead a new breakthrough in the application of
1642 SIF for the monitoring of vegetation C fluxes. The FLEX that is anticipated to be launched in
1643 2022 will map SIF globally at the finest spatial resolution (300 m) of all existing and upcoming
1644 spaceborne instruments (Drusch et al. 2017). In addition, a series of geostationary satellites are
1645 scheduled for launch in the 2019–2021 timeframe, and will provide unprecedented SIF
1646 measurements in sub-daily time intervals over some regions in Europe (Sentinel-4) and the
1647 Americas (TEMPO and GeoCARB). The variety of SIF datasets have the potential to open up a
1648 new era in mapping terrestrial photosynthesis. However, further work is needed in order to
1649 develop methods to estimate GPP from SIF observations. These models will have to deal with, at
1650 least, the effect of canopy structure effects on SIF data, the physiological relationships between
1651 SIF, photosynthesis and non-photochemical quenching, and the upscaling from instantaneous
1652 and clear-sky SIF data to the diurnal and all-sky conditions in which GPP estimates are typically
1653 reported.

1654 The growing number of EC flux sites globally, especially more sites in under-represented
1655 ecosystems and regions, is anticipated to benefit the upscaling of C fluxes to regional to global
1656 scales based on machine learning approaches. A tremendous amount of new remotely sensed
1657 data can be used to upscale ecosystem C fluxes. For example, new satellite data products such as
1658 gridded SIF products derived from OCO-2 (e.g., GOSIF) (Li and Xiao 2019), gridded SIF
1659 observations from TROPOMI (Kohler et al. 2018) and FLEX, and gridded soil moisture products
1660 from the Soil Moisture Active Passive (SMAP) mission (Brown et al. 2013) will potentially

1661 improve the upscaling of flux observations. The integration of the Landsat archive and Sentinel
1662 data will greatly improve the frequency of cloud-free observations, which can make it possible to
1663 upscale C fluxes from towers to regional scales with finer spatial resolution (e.g., 30 m). The
1664 fusion between Landsat and Sentinel data with higher spatial resolution and MODIS data with
1665 more frequent coverage could lead to reflectance and VIs with higher temporal and spatial
1666 resolution that will help capture fast responses of vegetation to stress conditions (e.g., droughts)
1667 and thus the model capacity to capture the detailed seasonal variations and abrupt changes. Other
1668 potential directions in the machine learning approaches include how to better incorporate
1669 management and disturbance information and how to quantify and reduce the uncertainties in
1670 upscaled fluxes.

1671 The column CO_2 concentrations observed by satellite missions such as GOSAT, OCO-2, and
1672 GOSAT-2 are expected to be more frequently used to quantify NBP at regional to global scales,
1673 while reducing the uncertainty in the resulting NBP estimates is critical for assessing C budgets
1674 and informing climate policy. The launch of high-resolution imaging CO_2 sensors in a few years
1675 (Polonsky et al. 2014; Pinty et al. 2017) will allow monitoring the plumes of CO_2-rich or CO_2-
1676 depleted air. Anthropogenic emissions are a primary target but they will provide novel
1677 information about natural fluxes as well. However, they will further challenge the quality of the
1678 transport models that will have to properly simulate these plumes within the inverse systems.
1679 Merging atmospheric inversion with Numerical Weather Prediction data assimilation could be a
1680 natural way forward.

1681 Besides the satellite missions mentioned above, hyperspectral imagery from recently
1682 launched and forthcoming satellites is expected to benefit the estimation of C fluxes. The
1683 recently launched and forthcoming sensors, such as PRISMA (Prototype Research Instruments

and Space Mission technology Advancement) (launched in March 2019) (Stefano et al. 2013), SBG (Surface Biology and Geology) (previously Hyperspectral InfraRed Imager, HyspIRI) (Lee et al. 2015a), and EnMap (Environmental Mapping and Analysis Program) (Guanter et al. 2015b), will also produce an increasing amount of hyperspectral data with spatial resolution of 20-30 m, 30 m, and 60 m, respectively. In addition, new CubeSat-type constellations of dozens or hundreds of small satellites in orbit will potentially provide land observations with high spatial and temporal coverage that will be useful to C cycle studies, although the processing and inter-calibration of these observations can be a challenge.

Integrating satellite-based data products and process-based models will continue to be an effective way to improve our understanding of terrestrial C cycle processes. First, satellite-based data products need to be improved by reducing their uncertainties. Second, some key variables such as disturbance history, which we currently face difficulties to estimate globally, will benefit process-based modeling. Third, methods of model and data integration, including model parameter optimization and data assimilation, need to be further explored. These model and data integration studies mostly rely on a single satellite-based product. Use of multiple satellite-based products can likely refine terrestrial process-based models. Currently, many terrestrial process-based prognostic models are used to evaluate global terrestrial C budget (Le Quere et al. 2017; Sitch et al. 2015) and show large model-by-model differences in estimated terrestrial C fluxes. With the aid of improved and new satellite-based terrestrial products and integration techniques with process models, these model-by-model differences can be potentially reduced.

8.2. Remote sensing of carbon stocks

Passive optical remote sensing, microwave remote sensing, and lidar remote sensing will continue to be used for AGB estimation. Passive optical remote sensing will continue to be one

of the most important data sources for AGB estimation because of its high spatial and temporal resolution and spatially and temporally continuous coverage. Recently, the NASA Harmonized Landsat and Sentinel-2 (HLS) product has been operationally produced in near real time by combining Lansat-8 and Sentinel-2 observations (Claverie et al. 2018), which allows us to monitor vegetation dynamics at a 30-m field scale with an interval of fewer than 5 days across the globe. Thus, the HLS time series could be used to extract an optimal time series for estimating AGB, which will enhance the capability of consistent AGB estimation from local to global scales. However, the establishment of empirical models or deep machine learning algorithms based on passive optical remote sensing requires a large set of reliable training data representing a broad range of biomass values, while such training data are usually insufficient at regional or global scales. There is a need for the generation of large AGB samples from in situ measurements, very high-resolution passive remote sensing data (e.g., QuickBird, IKONOS, and UAVs), and lidar measurements. Combining HLS data, satisfactory training samples, and deep machine learning algorithms will significantly improve the performance of AGB estimation. Further, saturation issue in biomass estimation using passive optimal remote sensing is expected to be at least partly solved by the fusion of passive optical remote sensing with lidar and microwave remote sensing data.

It has been nearly three decades since the SAR data were initially used for the estimation of forest AGB. The accurate mapping of forest biomass with SAR data at regional scales faces three challenges: saturation problems, terrain effects, and scale issue between the size of field sampling plot and the basic unit of regional mapping of forest AGB. The saturation problem in biomass estimation using radar backscatter intensity may be improved or solved by incorporating forest spatial structure information derived from InSAR data (Sun et al. 2011) or other data such

as optical stereo images (Zhang et al. 2017). Using the three-dimensional information derived from InSAR, Radargrammetry, and optical stereoscopy to estimate forest height or to improve the biomass estimation from SAR data will remain an active study area. For example, the digital surface model (DSM) from TanDEM-X data can be used to monitor forest biomass changes (Karila et al. 2019). If the digital terrain model (DTM) exists, the InSAR DSM can be used to generate canopy height model (CHM) or biomass maps. NASA's NISAR, to be launched in 2021, will provide global L-band InSAR data for biomass mapping and forest disturbance monitoring. As mentioned earlier, the PolInSAR or TomoSAR data, especially at L and P bands, can be used to retrieve the 3D structure of forest canopy directly without DTM. With the launch of TanDEM-L and BIOMASS (Quegan et al. 2019), both scheduled in 2022, the PolInSAR and TomoSAR data will be widely available to users, and therefore the effects of complex terrains on PolInSAR or TomoSAR data can be further explored. The terrain effect is a barrier for accurate biomass estimation based on SAR data. The development of theoretical models and simulations will likely help identify a proper solution to terrain effects (Ni et al. 2018). One solution to the scale issue could be the synergy of SAR data with other types of data such as lidar (Qi and Dubayah 2016) and stereo imagery (Zhang et al. 2017).

Lidar sensors and systems have evolved dramatically. TLS is becoming more portable and is being integrated with mobile platforms (e.g., mobile laser scanning or MLS, backpack laser scanning or BLS). ALS data have the tendency to be integrated with data from other sensors like hyperspectral sensors (Asner et al. 2007; Kampe et al. 2010; Cook et al. 2013; Pang et al. 2016). With the decrease of the data acquisition cost, ALS is being applied for biomass estimation (Price et al. 2017) or sampling at large scales (Matasci et al. 2018). With more spaceborne lidar systems on-orbit, the expendability and generalizability of the AGB estimation models based on

1753 lidar data will need more consideration for operational regional or global biomass mapping
1754 efforts. The recently launched GEDI will provide estimates of forest biomass over broad regions.
1755 The GEDI will produce high resolution laser ranging observations of the 3D structure of the
1756 Earth using a geodetic-class lidar laser system with a 25 m footprint. The integration of
1757 spaceborne lidar, SAR, and passive optical remote sensing data is anticipated to provide
1758 seamless, more accurate AGB estimates at the global scale.

1759 Passive optical remote sensing will continue to be used for the mapping of SOC at landscape
1760 to regional scales. The recent launch of the Sentinel-2A and -2B satellite sensors by the
1761 European Space Agency (Baillarin et al. 2012) will produce an increasing amount of
1762 multispectral VNIR-SWIR data over the world with high revisit frequency (5 days) and spatial
1763 resolution from 10 to 20m, which could be used in SCORPAN models for SOC content and
1764 stock mapping. This high revisit frequency would allow the acquisition of Sentinel-2 data during
1765 both periods either with adequate vegetation coverage and periods with high coverage of bare
1766 soils. Hyperspectral imagery from recently launched and forthcoming satellites is expected to
1767 benefit the estimation of SOC at regional scales. The launch of forthcoming sensors, such as
1768 PRISMA (Stefano et al. 2013), SBG (Lee et al. 2015a), and EnMap (Stuffler et al. 2007) satellite
1769 sensors will also produce an increasing amount of hyperspectral VNIR-SWIR data with spatial
1770 resolution of 20-30 m, 30 m, and 60 m, respectively, which could be used in SFTs models for
1771 SOC content and stock mapping.

1772 **8.3. Quantifying and reducing uncertainty in carbon flux and stock estimates**

1773 Uncertainty information of carbon fluxes is essential for carbon cycle studies. First, modeled
1774 fluxes with uncertainty bounds can facilitate the direct comparison between modeled and
1775 observed fluxes/stocks. Second, the quantification of uncertainty will also facilitate the

intercomparison of different approaches (e.g., modeling, inventory, atmospheric inversions). Third, the availability of uncertainty information will help interpret the dynamics in carbon fluxes/stocks. Fourth, a better understanding of the sources of uncertainty can provide insight on future improvement of ecosystem approaches and input data streams. Finally, better quantification of the uncertainty in C flux/stock estimates is essential for sound climate and decision-making. Estimates of C fluxes and stocks based on remote sensing could have significant uncertainties, while quantifying and reducing these uncertainties still remain a grand challenge. Future efforts are needed to account for various sources of uncertainty and thereby to quantify the full uncertainty in C flux and stock estimates. Meanwhile, it is equally important to reduce the uncertainty in the estimates of C fluxes and/or stocks by using remotely sensed data with higher quality and finer resolution and better approaches.

8.4. Long-term trends in carbon fluxes and stocks

Recent decades have witnessed dramatic changes in the Earth's climate, including a dramatic rise in air temperature, elevated atmospheric CO_2, enhanced nitrogen (N) deposition, and increasing drought frequency and severity (IPCC 2013). Rapid changes in land cover/land use, including deforestation, afforestation, and urbanization, have also occurred. These changes have substantially altered ecosystem function and processes. For example, there is compelling evidence that many parts of the northern middle and high latitudes have been exhibiting "greening" trends since the early 1980s (Zhou et al. 2001; Xiao and Moody 2005; Saleska et al. 2016). Evidence of the greening is mainly from the NDVI record derived from AVHRR on board NOAA's polar-orbiting satellites. The satellite-derived greening signal has been widely interpreted as evidence that ecosystem productivity and net C uptake have been increasing in many parts of the Earth's land surface. Despite these efforts, a more recent study based on long-

term satellite and FLUXNET records found that there were no trends in spring and autumn phenology in the northern hemisphere during the warming hiatus (Wang et al. 2019). More studies are needed to reveal the long-term trends in carbon fluxes. Meanwhile, a mechanistic understanding of the observed trends is also needed. Satellite observations have also been used to assess the long-term trends in terrestrial biomass (Liu et al. 2015). Inter-calibration among different sensors and bias correction for orbital drift and sensor degradation are critical for long-term analyses in remote sensing data. Inter-calibration among sensors and bias correction are essential for ensuring a high-quality, long-term GIMMS3g NDVI record (Pinzon and Tucker 2014). The radiometric degradation of MetOp-A GOME-2 over its lifetime has led to declining SIF (Joiner et al. 2016), which has hindered long-term analyses of SIF. The lengthening of the satellite records and the addition of new satellite observations will further extend our capabilities to examine long-term trends in ecosystem C fluxes and/or stocks and their responses and feedbacks to the climate.

8.5. Geospatial processing platforms facilitating remote sensing of the terrestrial carbon cycle

Geospatial processing platforms that provide high performance computing and massive storage capacity are anticipated to play an important role in remote sensing of the terrestrial C cycle in the future. Google Earth Engine is perhaps the most advanced cloud-based geospatial processing platform in the world that is currently available to the remote sensing research community and the public (Gorelick et al. 2017). This platform allows the users to perform highly-interactive algorithm development and develop data products at the global scale. It makes a tremendous amount of widely-used data (e.g., Landsat, MODIS) available so that the users do not need to download or store these data. Downloading satellite data for multiple years for the globe could

be a formidable task to an individual scientist for the medium resolution (e.g., 1 km), not to mention finer spatial resolution (e.g., 30 m). With the massive computing and storage capabilities, various built-in functions, and tremendous amount of remote sensing and ancillary (e.g., climate) data, Google Earth Engine and potentially other geospatial processing platforms are anticipated to greatly facilitate planetary-scale remote sensing of the terrestrial C cycle.

8.6. Synergy and integration of remote sensing data in carbon cycle studies

Remotely sensed data from different platforms/sensors have been synergistically used. For example, the VIs from the AVHRR and MODIS have been merged to generate the Vegetation Index and Phenology product (Didan 2014). OCO-2 SIF soundings and MODIS data were blended to develop global, gridded SIF estimates for the period from 2000 to present (e.g., GOSIF) (Li and Xiao 2019). The lidar-radar synergies improved the accuracy in forest biomass estimates (Hyde et al. 2007; Sun et al. 2011), and the synergy of Landsat 8/OLI and ICESat-2 improved the estimation of shrub/herbaceous biomass (Glenn et al. 2016). Synergies of different remote sensing data will receive growing attention in future C cycle studies. For example, the synergies of VIs and SIF are likely to improve the estimation of C fluxes. The synergistic use of lidar, radar, and passive optical remote sensing data is expected to be more widely used for biomass estimation, particularly at regional to global scales. The synergy and integration of different remote sensing data and methods have the potential to quantify the different C flux components and C stocks and therefore to assess the entire terrestrial C cycle at regional to global scales. For example, VIs, SIF, LUE models, data-driven methods, and atmospheric inversions can be used to estimate C fluxes; biophysical variables and vegetation properties (e.g., LAI, FAPAR, canopy N content) derived from multispectral and hyperspectral imagery can be assimilated to process-based models for simulating C fluxes and/or stocks; lidar, SAR, and the

synergy between lidar/SAR and passive optical remote sensing data (e.g., Landsat, Sentinel, MODIS) can be used to quantify biomass C stocks; the impacts of disturbance on the C cycle can also be quantified using remote sensing data. The synergistic use and integration of various remotes sensing data and methods can potentially provide a holistic picture of the terrestrial C cycle.

Acknowledgements:

This study was financially supported by the National Aeronautics and Space Administration (NASA) (the Carbon Cycle Science Program: NNX14AJ18G; the Climate Indicators and Data Products for Future National Climate Assessments: NNX16AG61G; the Science of Terra and Aqua: NNX14AI70G) and National Science Foundation (NSF) (MacroSystems Biology: EF-1638688). The lead author (J. Xiao) would like to thank Dr. David Schimel for helpful discussion. We thank Dr. Xufeng Wang for processing the GIMMS3g NDVI and MODIS EVI data and Dr. Yibo Liu for providing BEPS GPP data. We thank Dr. Steve Running and the two anonymous reviewers for their constructive and insightful comments on the manuscript.

Acronyms and abbreviations:

ABI	Advanced Baseline Imager
ACGS	Atmospheric Carbon Dioxide Grating Spectrometer
AGB	Aboveground biomass
AHI	Advanced Himawari Imager
AIRS	Atmospheric Infrared Sounder
ALS	Airborne laser scanners
AMSR-E	Advanced Microwave Scanning Radiometer for EOS
ANPP	Aboveground net primary productivity (NPP)
AOP	Airborne observation platform
APAR	Absorbed photosynthetically active radiation
AR	Autrophic respiration
ASCII	American Standard Code for Information Interchange

ASTER	Advanced Spaceborne Thermal Emission and Reflection Radiometer
ATLAS	Advanced Topographic Laser Altimeter System
AVHRR	Advanced very high resolution radiometer
AVIRIS	Airborne Visible/InfraRed Imaging Spectrometer
BEAMS	Biosphere model integrating Eco-physiological And Mechanistic approaches using Satellite data
BEPS	Boreal Ecosystems Productivity Simulator
BLS	Backpack laser scanning
BRDF	Bidirectional reflectance distribution function
CASA	Carnegie Ames Stanford Approach Biosphere model
CHM	Canopy height model
CLM	Community Land Model
CMS	Carbon Monitoring System
CO_2	Carbon dioxide
CSA	Canadian Space Agency
DAIS	Digital Airborne Imaging Spectrometer
DBH	Diameter at breast height
DGVM	Dynamic Global Vegetation Model
DRL	Discrete return lidar
DSM	Digital Surface Model
DTM	Digital Terrain Model
EC	Eddy covariance
EC-MOD	Eddy Covariance-MODIS
EnMap	Environmental Mapping and Analysis Program
EnviSat	ENVIronment SATellite
EO-1	Earth Observing-1
EOS	Earth Observing System
ER	Ecosystem respiration
ERS	European Remote Sensing
ESA	European Space Agency
ETM+	Enhanced Thematic Mapper Plus
EVI	Enhanced vegetation index
EVI-2	Two-band EVI
FAPAR	Fraction of absorbed photosynthetically active radiation
FIA	Forest Inventory Data
FLEX	FLuorescence EXplorer
FOTO	Fourier Transform Textural Ordination
GEDI	Global Ecosystem Dynamics Investigation
GeoCARB	Geostationary Carbon Observatory
GIMMS	Global Inventory Monitoring and Modeling System
GLAS	Geoscience Laser Altimeter System
GLASS	Global LAnd Surface Satellite
GO	Geometric-optical
GOES	Geostationary Operational Environmental Satellites
GOFC-GOLD	Global Observation of Forest Cover and Land Dynamics
GOME-2	Global Monitoring Ozone Experiment 2

1920	GOSAT	Greenhouse gases Observing SATellite
1921	GPP	Gross primary productivity
1922	HIRS-2	High resolution Infrared Radiation Sounder-2
1923	HLS	Harmonized Landsat and Sentinel-2
1924	HR	Heterotrophic respiration
1925	Hyperion	Hyperspectral Imager
1926	HyspIRI	Hyperspectral Infrared Imager
1927	ICESat	Ice, Cloud,and land Elevation Satellite
1928	InSAR	SAR interferometry
1929	InTEC	Integrated Terrestrial Ecosystem C-budget model
1930	ISS	International Space Station
1931	JAXA	Japan Aerospace Exploration Agency
1932	JERS-1	Japanese Earth Resources Satellite 1
1933	JPSS-1	First Joint Polar Satellite System
1934	LAI	Leaf area index
1935	lidar	Light detection and ranging
1936	LST	Land surface temperature
1937	LUE	Light use efficiency
1938	LVIS	Laser Vegetation Imaging Sensor
1939	MABEL	Multiple Altimeter Beam Experimental Lidar
1940	MIR	Middle infrared
1941	MLS	Mobile laser scanning
1942	MODIS	Moderate resolution imaging spectroradiometer
1943	MSI	Multispectral Imager
1944	MTBS	Monitoring Trends in Burn Severity
1945	MTCI	MERIS total chlorophyll index
1946	NASA	National Aeronautics and Space Administration
1947	NBP	Net biome productivity
1948	NDVI	Normalized difference vegetation index
1949	NDWI	Normalized difference water index
1950	NEE	Net ecosystem exchange
1951	NEON	National Ecological Observatory Network
1952	NEP	Net ecosystem productivity
1953	NIR	Rear-infrared
1954	NISAR	NASA-ISRO SAR Mission
1955	NOAA	National Oceanic and Atmospheric Administration
1956	NPP	Net primary productivity
1957	OCO-2	Orbiting Carbon Observatory-2
1958	OCO-3	Orbiting Carbon Observatory-3
1959	OLI	Operational Land Imager
1960	ORCHIDEE	Organizing Carbon and Hydrology in Dynamics Ecosystems model
1961	PALSAR	Phased Array type L-band Synthetic Aperture Radar
1962	PAR	Photosynthetically active radiation
1963	PCA	Principal component analysis
1964	PolInSAR	Polarimetric SAR interferometry

PRISMA	Prototype Research Instruments and Space Mission technology Advancement
PVI	Perpendicular vegetation index
RAR	Real aperture radar
REDD+	Reducing emissions from deforestation and forest degradation
RMSE	Root mean squared error
RT	Radiative transfer
SAR	Synthetic aperture radar
SCIAMACHY	SCanning Imaging Absorption spectroMeter for Atmospheric CartograpHY
SCOPE	Soil Canopy Observation, Photochemistry and Energy fluxes
SCORPAN	*s*oils and/or soil properties, *c*limate and/or climate properties, *o*rganisms like flora and fauna and human activities, *r*elief settings, *p*arent material, *a*ge, and spatial coordinate *n*
SeaSat	Seafaring Satellite
SiB2	Simple Biosphere Model 2
SIF	Solar-induced chlorophyll fluorescence
SIR-C/X-SAR	Spaceborne Imaging Radar-C / X-Band Synthetic Aperture Radar
SLICER	Scanning LiDAR Imager of Canopies by Echo Recovery
SMA	Spectral mixture analysis
SMAP	Soil Moisture Active Passive Mission
SOC	Soil organic carbon
SPOT	Satellite Pour l'Observation de la Terre
SR	Simple Ratio
STFs	SpectroTransfer Functions
SWIR	Shortwave infrared
TanSat	Chinese Carbon Dioxide Observation Satellite
TANSO-FTS	Carbon Observation-Fourier Transform Spectrometer
TC	Tasseled cap transformation
TC-GVI	Tasselled cap green vegetation index
TEMPO	Tropospheric Emissions: Monitoring of Pollution
TES	Tropospheric Emission Spectrometer
TIR	Thermal infrared
TIRS-2	Thermal Infrared Sensor 2
TLS	Terrestrial laser scanning
TM	Thematic Mapper
TomoSAR	Tomographic SAR
TROPOMI	TROPOspheric Monitoring Instrument
UAV	Unmanned aerial vehicles
USDA	U.S. Department of Agriculture
USGS	U.S. Geological Survey
VI	Vegetation index
VIIRS	Visible Infrared Imaging Radiometer Suite
VNIR/SWIR	Visible Near Infrared and Short Wave Infrared
WDRVI	Wide dynamic range vegetation index

2011

2012 **References:**

2013 Ai, J.L., Jia, G.S., Epstein, H.E., Wang, H.S., Zhang, A.Z., Hu, Y.H. 2018. MODIS-Based
2014 Estimates of Global Terrestrial Ecosystem Respiration. *Journal of Geophysical Research-*
2015 *Biogeosciences,* 123, 326-352.
2016 Alemohammad, S.H., Fang, B., Konings, A.G., Aires, F., Green, J.K., Kolassa, J., Miralles, D.,
2017 Prigent, C., Gentine, P. 2017. Water, energy, and carbon with artificial neural networks
2018 (WECANN): a statistically based estimate of global surface turbulent fluxes and gross
2019 primary productivity using solar-induced fluorescence. *Biogeosciences,* 14, 4101-4124.
2020 Asner, G.P., Knapp, D.E., Kennedy-Bowdoin, T., Jones, M.O., Martin, R.E., Boardman, J., Field,
2021 C.B. 2007. Carnegie Airborne Observatory: in-flight fusion of hyperspectral imaging and
2022 waveform light detection and ranging (wLiDAR) for three-dimensional studies of
2023 ecosystems. *Journal of Applied Remote Sensing,* 1, 013536,
2024 https://doi.org/10.1117/1.2794018.
2025 Asrar, G., Fuchs, M., Kanemasu, E.T., Hatfield, J.L. 1984. Estimating absorbed photosynthetic
2026 radiation and leaf-area index from spectral reflectance in wheat. *Agronomy Journal,* 76,
2027 300-306.
2028 Astrup, R., Ducey, M.J., Granhus, A., Ritter, T., von Lupke, N. 2014. Approaches for estimating
2029 stand-level volume using terrestrial laser scanning in a single-scan mode. *Canadian*
2030 *Journal of Forest Research-Revue Canadienne De Recherche Forestiere,* 44, 666-676.
2031 Atkin, O.K., Tjoelker, M.G. 2003. Thermal acclimation and the dynamic response of plant
2032 respiration to temperature. *Trends in Plant Science,* 8, 343-351.
2033 Baccini, A., Friedl, M.A., Woodcock, C.E., Warbington, R. 2004. Forest biomass estimation
2034 over regional scales using multisource data. *Geophysical Research Letters,* 31, L10501,
2035 doi:10.1029/2004GL019782.
2036 Baccini, A., Laporte, N., Goetz, S.J., Sun, M., Dong, H. 2008. A first map of tropical Africa's
2037 above-ground biomass derived from satellite imagery. *Environmental Research Letters,* 3,
2038 045011, doi:10.1088/1748-9326/3/4/045011.
2039 Baillarin, S.J., Meygret, A., Dechoz, C., Petrucci, B., Lacherade, S., Tremas, T., Isola, C.,
2040 Martimort, P., Spoto, F., Ieee (2012). Sentinel-2 level 1 products and image processing
2041 performances. *2012 Ieee International Geoscience and Remote Sensing Symposium* (pp.
2042 7003-7006). New York: Ieee.
2043 Baldocchi, D., Falge, E., Gu, L.H., Olson, R., Hollinger, D., Running, S., Anthoni, P., Bernhofer,
2044 C., Davis, K., Evans, R., Fuentes, J., Goldstein, A., Katul, G., Law, B., Lee, X.H., Malhi,
2045 Y., Meyers, T., Munger, W., Oechel, W., U, K.T.P., Pilegaard, K., Schmid, H.P.,
2046 Valentini, R., Verma, S., Vesala, T., Wilson, K., Wofsy, S. 2001. FLUXNET: A new tool
2047 to study the temporal and spatial variability of ecosystem-scale carbon dioxide, water
2048 vapor, and energy flux densities. *Bulletin of the American Meteorological Society,* 82,
2049 2415-2434.
2050 Barkley, M.P., Monks, P.S., Engelen, R.J. 2006. Comparison of SCIAMACHY and AIRS CO2
2051 measurements over North America during the summer and autumn of 2003. *Geophysical*
2052 *Research Letters,* 33, L20805, doi:10.1029/2006GL026807.
2053 Bartholomeus, H., Kooistra, L., Stevens, A., van Leeuwen, M., van Wesemael, B., Ben-Dor, E.,
2054 Tychon, B. 2011. Soil Organic Carbon mapping of partially vegetated agricultural fields

with imaging spectroscopy. *International Journal of Applied Earth Observation and Geoinformation,* 13, 81-88.
Basu, S., Guerlet, S., Butz, A., Houweling, S., Hasekamp, O., Aben, I., Krummel, P., Steele, P., Langenfelds, R., Torn, M., Biraud, S., Stephens, B., Andrews, A., Worthy, D. 2013. Global CO2 fluxes estimated from GOSAT retrievals of total column CO2. *Atmospheric Chemistry and Physics,* 13, 8695-8717.
Beaudoin, A., Letoan, T., Goze, S., Nezry, E., Lopes, A., Mougin, E., Hsu, C.C., Han, H.C., Kong, J.A., Shin, R.T. 1994. Retrieval of forest biomass from SAR data. *International Journal of Remote Sensing,* 15, 2777-2796.
Ben-dor, E., Banin, A. 1995. Near-infrared analysis as a rapid method to simultaneously evaluate several soil properties. *Soil Science Society of America Journal,* 59, 364-372.
Ben-Dor, E., Inbar, Y., Chen, Y. 1997. The reflectance spectra of organic matter in the visible near-infrared and short wave infrared region (400-2500 nm) during a controlled decomposition process. *Remote Sensing of Environment,* 61, 1-15.
Ben-Dor, E., Irons, J.A., Epema, G.F. (1999). Soil reflectance. *Manual of Remote Sensing: Remote Sensing for the Earth Sciences* (pp. 111-189): New York: John Wiley & Sons Inc.
Ben-Dor, E., Patkin, K., Banin, A., Karnieli, A. 2002. Mapping of several soil properties using DAIS-7915 hyperspectral scanner data - a case study over clayey soils in Israel. *International Journal of Remote Sensing,* 23, 1043-1062.
Blackard, J.A., Finco, M.V., Helmer, E.H., Holden, G.R., Hoppus, M.L., Jacobs, D.M., Lister, A.J., Moisen, G.G., Nelson, M.D., Riemann, R., Ruefenacht, B., Salajanu, D., Weyermann, D.L., Winterberger, K.C., Brandeis, T.J., Czaplewski, R.L., McRoberts, R.E., Patterson, P.L., & Tymcio, R.P. 2008. Mapping US forest biomass using nationwide forest inventory data and moderate resolution information. *Remote Sensing of Environment,* 112, 1658-1677.
Bodesheim, P., Jung, M., Gans, F., Mahecha, M.D., Reichstein, M. 2018. Upscaled diurnal cycles of land-atmosphere fluxes: a new global half-hourly data product. *Earth System Science Data,* 10, 1327-1365.
Bolton, D.K., Coops, N.C., Wulder, M.A. 2015. Characterizing residual structure and forest recovery following high-severity fire in the western boreal of Canada using Landsat time-series and airborne lidar data. *Remote Sensing of Environment,* 163, 48-60.
Boyte, S.P., Wylie, B.K., Howard, D.M., Dahal, D., Gilmanov, T. 2018. Estimating carbon and showing impacts of drought using satellite data in regression-tree models. *International Journal of Remote Sensing,* 39, 374-398.
Breiman, L. 2001. Random forests. *Machine Learning,* 45, 5-32.
Bright, B.C., Hicke, J.A., Hudak, A.T. 2012a. Estimating aboveground carbon stocks of a forest affected by mountain pine beetle in Idaho using lidar and multispectral imagery. *Remote Sensing of Environment,* 124, 270-281.
Bright, B.C., Hicke, J.A., Hudak, A.T. 2012b. Landscape-scale analysis of aboveground tree carbon stocks affected by mountain pine beetles in Idaho. *Environmental Research Letters,* 7, 045702.
Bright, B.C., Hicke, J.A., Meddens, A.J.H. 2013. Effects of bark beetle-caused tree mortality on biogeochemical and biogeophysical MODIS products. *Journal of Geophysical Research: Biogeosciences*, 118, 974–982.

Brown, M.E., Escobar, V., Moran, S., Entekhabi, D., O'Neill, P.E., Njoku, E.G., Doorn, B., Entin, J.K. 2013. NASA's Soil Moisture Active Passive (SMAP) mission and opportunities for applications users. *Bulletin of the American Meteorological Society,* 94, 1125-1128.

Buchwitz, M., Reuter, M., Schneising, O., Hewson, W., Detmers, R.G., Boesch, H., Hasekamp, O.P., Aben, I., Bovensmann, H., Burrows, J.P., Butz, A., Chevallier, F., Dils, B., Frankenberg, C., Heymann, J., Lichtenberg, G., De Maziere, M., Notholt, J., Parker, R., Warneke, T., Zehner, C., Griffith, D.W.T., Deutscher, N.M., Kuze, A., Suto, H., Wunch, D. 2017. Global satellite observations of column-averaged carbon dioxide and methane: The GHG-CCI XCO2 and XCH4 CRDP3 data set. *Remote Sensing of Environment, 203*, 276-295.

Cai, W.W., Yuan, W.P., Liang, S.L., Zhang, X.T., Dong, W.J., Xia, J.Z., Fu, Y., Chen, Y., Liu, D., Zhang, Q. 2014. Improved estimations of gross primary production using satellite-derived photosynthetically active radiation. *Journal of Geophysical Research-Biogeosciences,* 119, 110-123.

Calvao, T., Palmeirim, J.M. 2004. Mapping Mediterranean scrub with satellite imagery: biomass estimation and spectral behaviour. *International Journal of Remote Sensing,* 25, 3113-3126.

Cambou, A., Cardinael, R., Kouakoua, E., Villeneuve, M., Durand, C., Barthes, B.G. 2016. Prediction of soil organic carbon stock using visible and near infrared reflectance spectroscopy (VNIRS) in the field. *Geoderma,* 261, 151-159.

Chambers, J.Q., Fisher, J.I., Zeng, H.C., Chapman, E.L., Baker, D.B., Hurtt, G.C. 2007. Hurricane Katrina's carbon footprint on U. S. Gulf Coast forests. *Science,* 318, 1107-1107.

Chang, C.W., Laird, D.A. 2002. Near-infrared reflectance spectroscopic analysis of soil C and N. *Soil Science,* 167, 110-116.

Chedin, A., Serrar, S., Scott, N.A., Crevoisier, C., Armante, R. 2003. First global measurement of midtropospheric CO2 from NOAA polar satellites: Tropical zone. *Journal of Geophysical Research-Atmospheres,* 108(D18), 4581, doi:10.1029/2003JD003439, 2003.

Chen, B., Pang, Y., Li, Z., Lu, H., Liu, L., North, P.R.J., Rosette, J.A.B. 2019. Ground and top of canopy extraction from photon counting LiDAR data using local outlier factor with ellipse searching area. *IEEE Geoscience and Remote Sensing Letters*, doi: 10.1109/LGRS.2019.2899011.

Chen, D., Chang, N.J., Xiao, J.F., Zhou, Q.B., Wu, W.B. 2019. Mapping dynamics of soil organic matter in croplands with MODIS data and machine learning algorithms. *Science of the Total Environment,* 669, 844-855.

Chen, J., Chen, W.J., Liu, J., Cihlar, J., Gray, S. 2000. Annual carbon balance of Canada's forests during 1895-1996. *Global Biogeochemical Cycles,* 14, 839-849.

Chevallier, F., Engelen, R.J., Carouge, C., Conway, T.J., Peylin, P., Pickett-Heaps, C., Ramonet, M., Rayner, P.J., Xueref-Remy, I. 2009. AIRS-based versus flask-based estimation of carbon surface fluxes. *Journal of Geophysical Research-Atmospheres,* 114, D20303, doi:10.1029/2009JD012311.

Chevallier, F., Engelen, R.J., Peylin, P. 2005. The contribution of AIRS data to the estimation of CO2 sources and sinks. *Geophysical Research Letters,* 32, L23801, doi:10.1029/2005GL024229.

Chevallier, F., Palmer, P.I., Feng, L., Boesch, H., O'Dell, C.W., Bousquet, P. 2014. Toward robust and consistent regional CO_2 flux estimates from in situ and spaceborne measurements of atmospheric CO_2. *Geophysical Research Letters,* 41, 1065-1070.

Chopping, M., Schaaf, C.B., Zhao, F., Wang, Z.S., Nolin, A.W., Moisen, G.G., Martonchik, J.V., Bull, M. 2011. Forest structure and aboveground biomass in the southwestern United States from MODIS and MISR. *Remote Sensing of Environment,* 115, 2943-2953.

Ciais, P., Sabine, C., Bala, G., Bopp, L., Brovkin, V., Canadell, J., Chhabra, A., DeFries, R., Galloway, J., Heimann, M., Jones, C., Le Quéré, C., Myneni, R.B., Piao, S., Thornton, P. (2013). Carbon and Other Biogeochemical Cycles. In T.F. Stocker, D. Qin, G.-K. Plattner, M. Tignor, S.K. Allen, J. Boschung, A. Nauels, Y. Xia, V. Bex, & P.M. Midgley (Eds.), *Climate Change 2013: The Physical Science Basis. Contribution of Working Group I to the Fifth Assessment Report of the Intergovernmental Panel on Climate Change*. Cambridge, United Kingdom and New York, NY, USA: Cambridge University Press.

Claverie, M., Ju, J., Masek, J.G., Dungan, J.L., Vermote, E.F., Roger, J.C., Skakun, S.V., Justice, C. 2018. The Harmonized Landsat and Sentinel-2 surface reflectance data set. *Remote Sensing of Environment,* 219, 145-161.

Cloude, S.R., Papathanassiou, K.P. 1998. Polarimetric SAR interferometry. *IEEE Transactions on Geoscience and Remote Sensing,* 36, 1551-1565.

Cohen, W.B., Maiersperger, T.K., Gower, S.T., Turner, D.P. 2003. An improved strategy for regression of biophysical variables and Landsat ETM+ data. *Remote Sensing of Environment,* 84, 561-571.

Cohen, W.B., Maiersperger, T.K., Turner, D.P., Ritts, W.D., Pflugmacher, D., Kennedy, R.E., Kirschbaum, A., Running, S.W., Costa, M., Gower, S.T. 2006. MODIS land cover and LAI collection 4 product quality across nine sites in the western hemisphere. *Ieee Transactions on Geoscience and Remote Sensing,* 44, 1843-1857.

Cohen, W.B., Yang, Z.Q., Stehman, S.V., Schroeder, T.A., Bell, D.M., Masek, J.G., Huang, C.Q., Meigs, G.W. 2016. Forest disturbance across the conterminous United States from 1985-2012: The emerging dominance of forest decline. *Forest Ecology and Management,* 360, 242-252.

Collatz, G.J., Ball, J.T., Grivet, C., Berry, J.A. 1991. Physiological and environmental regulation of stomatal conductance, photosynthesis, and transpiration: a model that includes a laminar boundary layer. *Agricultural and Forest Meteorology,* 54, 107-136.

Cook, B.D., Corp, L.A., Nelson, R.F., Middleton, E.M., Morton, D.C., McCorkel, J.T., Masek, J.G., Ranson, K.J., Ly, V., Montesano, P.M. 2013. NASA Goddard's LiDAR, Hyperspectral and Thermal (G-LiHT) Airborne Imager. *Remote Sensing,* 5, 4045-4066.

Cook, R.B., Margle, S.M., Holladay, S.K., Heinsch, F.A., Schaaf, C.B. (2004). Subsets of remote sensing products for AmeriFlux sites: MODIS ASCII Subsets. In, *Ameriflux Annual Meeting*. Boulder, CO.

Damm, A., Guanter, L., Paul-Limoges, E., van der Tol, C., Hueni, A., Buchmann, N., Eugster, W., Ammann, C., Schaepman, M.E. 2015. Far-red sun-induced chlorophyll fluorescence shows ecosystem-specific relationships to gross primary production: An assessment based on observational and modeling approaches. *Remote Sensing of Environment,* 166, 91-105.

Dash, J., Curran, P.J. 2004. The MERIS terrestrial chlorophyll index. *International Journal of Remote Sensing,* 25, 5403-5413.

Daumard, F., Champagne, S., Fournier, A., Goulas, Y., Ounis, A., Hanocq, J.F., Moya, I. 2010. A field platform for continuous measurement of canopy fluorescence. *IEEE Transactions on Geoscience and Remote Sensing,* 48, 3358-3368.

Demarty, J., Chevallier, F., Friend, A.D., Viovy, N., Piao, S.L., Ciais, P. 2007. Assimilation of global MODIS leaf area index retrievals within a terrestrial biosphere model. *Geophysical Research Letters,* 34, L15402, doi:10.1029/2007GL030014.

Detmers, R.G., Hasekamp, O., Aben, I., Houweling, S., van Leeuwen, T.T., Butz, A., Landgraf, J., Kohler, P., Guanter, L., Poulter, B. 2015. Anomalous carbon uptake in Australia as seen by GOSAT. *Geophysical Research Letters,* 42, 8177-8184.

Didan, K. 2014. Multi-Satellite Earth Science Data Record for Studying Global Vegetation Trends and changes, The University of Ari- zona, Tucson, AZ.

Disney, M.I., Vicari, M.B., Burt, A., Calders, K., Lewis, S.L., Raumonen, P., Wilkes, P. 2018. Weighing trees with lasers: advances, challenges and opportunities. *Interface Focus,* 8, 20170048. http://dx.doi.org/10.1098/rsfs.2017.0048.

Dobson, M.C., Ulaby, F.T., LeToan, T., Beaudoin, A., Kasischke, E.S., Christensen, N. 1992. Dependence of radar backscatter on coniferous forest biomass. *IEEE Transactions on Geoscience and Remote Sensing,* 30, 412-415.

Dolan, K.A., Hurtt, G.C., Chambers, J.Q., Dubayah, R.O., Frolking, S., Masek, J.G. 2011. Using ICESat's Geoscience Laser Altimeter System (GLAS) to assess large-scale forest disturbance caused by hurricane Katrina. *Remote Sensing of Environment,* 115, 86-96.

Dong, J.R., Kaufmann, R.K., Myneni, R.B., Tucker, C.J., Kauppi, P.E., Liski, J., Buermann, W., Alexeyev, V., Hughes, M.K. 2003. Remote sensing estimates of boreal and temperate forest woody biomass: carbon pools, sources, and sinks. *Remote Sensing of Environment,* 84, 393-410.

Dou, X.M., Yang, Y.G. 2018. Estimating forest carbon fluxes using four different data-driven techniques based on long-term eddy covariance measurements: Model comparison and evaluation. *Science of the Total Environment,* 627, 78-94.

Drake, J.B., Dubayah, R.O., Clark, D.B., Knox, R.G., Blair, J.B., Hofton, M.A., Chazdon, R.L., Weishampel, J.F., Prince, S.D. 2002. Estimation of tropical forest structural characteristics using large-footprint lidar. *Remote Sensing of Environment,* 79, 305-319.

Drusch, M., Moreno, J., Del Bello, U., Franco, R., Goulas, Y., Huth, A., Kraft, S., Middleton, E.M., Miglietta, F., Mohammed, G., Nedbal, L., Rascher, U., Schttemeyer, D., Verhoef, W. 2017. The FLuorescence EXplorer Mission Concept-ESA's Earth Explorer 8. *IEEE Transactions on Geoscience and Remote Sensing,* 55, 1273-1284.

Dube, T., Mutanga, O. 2015a. Evaluating the utility of the medium-spatial resolution Landsat 8 multispectral sensor in quantifying aboveground biomass in uMgeni catchment, South Africa. *Isprs Journal of Photogrammetry and Remote Sensing,* 101, 36-46.

Dube, T., Mutanga, O. 2015b. Investigating the robustness of the new Landsat-8 Operational Land Imager derived texture metrics in estimating plantation forest aboveground biomass in resource constrained areas. *ISPRS Journal of Photogrammetry and Remote Sensing,* 108, 12-32.

Eckert, S. 2012. Improved forest biomass and carbon estimations using texture measures from WorldView-2 satellite data. *Remote Sensing,* 4, 810-829.

Eidenshink, J., Schwind, B., Brewer, K., Zhu, Z., Quayle, B., Howard, S. 2007. A project for monitoring trends in burn severity. *Fire Ecology,* 3, 3-12.

Eldering, A., Wennberg, P.O., Crisp, D., Schimel, D.S., Gunson, M.R., Chatterjee, A., Liu, J., Schwandner, F.M., Sun, Y., O'Dell, C.W., Frankenberg, C., Taylor, T., Fisher, B., Osterman, G.B., Wunch, D., Hakkarainen, J., Tamminen, J., Weir, B. 2017. The Orbiting

2235 Carbon Observatory-2 early science investigations of regional carbon dioxide fluxes.
2236 *Science,* 358, eaam5745. DOI: 10.1126/science.aam5745
2237 Engelen, R.J., Andersson, E., Chevallier, F., Hollingsworth, A., Matricardi, M., McNally, A.P.,
2238 Thepaut, J.N., Watts, P.D. 2004. Estimating atmospheric CO2 from advanced infrared
2239 satellite radiances within an operational 4D-Var data assimilation system: Methodology
2240 and first results. *Journal of Geophysical Research-Atmospheres,* 109, D19309,
2241 doi:10.1029/2004JD004777.
2242 Enting, I.G., Trudinger, C.M., Francey, R.J. 1995. A synthesis inversion of the concentration and
2243 delta-C-13 of atmospheric CO_2. *Tellus Series B-Chemical and Physical Meteorology,* 47,
2244 35-52.
2245 Epstein, H.E., Raynolds, M.K., Walker, D.A., Bhatt, U.S., Tucker, C.J., Pinzon, J.E. 2012.
2246 Dynamics of aboveground phytomass of the circumpolar Arctic tundra during the past
2247 three decades. *Environmental Research Letters,* 7, 015506, oi:10.1088/1748-
2248 9326/7/1/01550.
2249 Fang, H.L., Wei, S.S., Jiang, C.Y., Scipal, K. 2012. Theoretical uncertainty analysis of global
2250 MODIS, CYCLOPES, and GLOBCARBON LAI products using a triple collocation
2251 method. *Remote Sensing of Environment,* 124, 610-621.
2252 Farquhar, G.D., Caemmerer, S.V., Berry, J.A. 1980. A biochemical model of photosynthetic CO_3
2253 assimilation in leaves of C_3 species. *Planta,* 149, 78-90.
2254 Fazakas, Z., Nilsson, M., Olsson, H. 1999. Regional forest biomass and wood volume estimation
2255 using satellite data and ancillary data. *Agricultural and Forest Meteorology,* 98-9, 417-
2256 425.
2257 Fensholt, R., Sandholt, I., Rasmussen, M.S. 2004. Evaluation of MODIS LAI, fAPAR and the
2258 relation between fAPAR and NDVI in a semi-arid environment using in situ
2259 measurements. *Remote Sensing of Environment,* 91, 490-507.
2260 Field, C.B., Randerson, J.T., Malmstrom, C.M. 1995. Global net primary production: Combining
2261 ecology and remote sensing. *Remote Sensing of Environment,* 51, 74-88.
2262 Flexas, J., Briantais, J.M., Cerovic, Z., Medrano, H., Moya, I. 2000. Steady-state and maximum
2263 chlorophyll fluorescence responses to water stress in grapevine leaves: A new remote
2264 sensing system. *Remote Sensing of Environment,* 73, 283-297.
2265 Folberth, G., Hauglustaine, D.A., Ciais, P., Lathiere, J. 2005. On the role of atmospheric
2266 chemistry in the global CO2 budget. *Geophysical Research Letters,* 32,
2267 L08801,doi:10.1029/2004GL021812.
2268 Foody, G.M., Boyd, D.S., Cutler, M.E.J. 2003. Predictive relations of tropical forest biomass
2269 from Landsat TM data and their transferability between regions. *Remote Sensing of*
2270 *Environment,* 85, 463-474.
2271 Foody, G.M., Cutler, M.E., McMorrow, J., Pelz, D., Tangki, H., Boyd, D.S., Douglas, I. 2001.
2272 Mapping the biomass of Bornean tropical rain forest from remotely sensed data. *Global*
2273 *Ecology and Biogeography,* 10, 379-387.
2274 Fournier, A., Daumard, F., Champagne, S., Ounis, A., Goulas, Y., Moya, I. 2012. Effect of
2275 canopy structure on sun-induced chlorophyll fluorescence. *ISPRS Journal of*
2276 *Photogrammetry and Remote Sensing,* 68, 112-120.
2277 Frankenberg, C., Fisher, J.B., Worden, J., Badgley, G., Saatchi, S.S., Lee, J.E., Toon, G.C., Butz,
2278 A., Jung, M., Kuze, A., Yokota, T. 2011. New global observations of the terrestrial
2279 carbon cycle from GOSAT: Patterns of plant fluorescence with gross primary
2280 productivity. *Geophysical Research Letters,* 38, L17706, doi:10.1029/2011GL048738.

2281 Franklin, J., Hiernaux, P.H.Y. 1991. Estimating foliage and woody biomass in Sahelian and
2282 Sudanian woodlands using a remote sensing model. *International Journal of Remote*
2283 *Sensing,* 12, 1387-1404.
2284 Frey, O., Morsdorf, F., Meier, E. 2008. Tomographic imaging of a forested area by airborne
2285 multi-baseline P-band SAR. *Sensors,* 8, 5884-5896.
2286 Friedl, M.A., McGwire, K.C., McIver, D.K. (2001). An overview of uncertainty in optical
2287 remotely sensed data for ecological applications. In M.F.G. C. T. Hunsaker, M. A. Friedl,
2288 and T. J. Case (Ed.), *Spatial Uncertainty in Ecology: Implications for Remote Sensing*
2289 *and GIS Applications* (pp. 258–283). New York, NY, USA: Springer.
2290 Friedl, M.A., Michaelsen, J., Davis, F.W., Walker, H., Schimel, D.S. 1994. Estimating grassland
2291 biomass and leaf area index using ground and satellite data. *International Journal of*
2292 *Remote Sensing,* 15, 1401-1420.
2293 Friedl, M.A., Sulla-Menashe, D., Tan, B., Schneider, A., Ramankutty, N., Sibley, A., Huang,
2294 X.M. 2010. MODIS Collection 5 global land cover: Algorithm refinements and
2295 characterization of new datasets. *Remote Sensing of Environment,* 114, 168-182.
2296 Frolking, S., Palace, M.W., Clark, D.B., Chambers, J.Q., Shugart, H.H., Hurtt, G.C. 2009. Forest
2297 disturbance and recovery: A general review in the context of spaceborne remote sensing
2298 of impacts on aboveground biomass and canopy structure. *Journal of Geophysical*
2299 *Research: Biogeosciences,* 114, G00E02, doi:10.1029/2008JG000911.
2300 Fu, P., Weng, Q.H. 2016. Consistent land surface temperature data generation from irregularly
2301 spaced Landsat imagery. *Remote Sensing of Environment,* 184, 175-187.
2302 Fuchs, H., Magdon, P., Kleinn, C., Flessa, H. 2009. Estimating aboveground carbon in a
2303 catchment of the Siberian forest tundra: Combining satellite imagery and field inventory.
2304 *Remote Sensing of Environment,* 113, 518-531.
2305 G, L.P. 1963. An analytical and experimental study of stereo for radar. *Photogrammetric*
2306 *Engineering,* 29, 294-300.
2307 Gamon, J.A., Coburn, C., Flanagan, L.B., Huemmrich, K.F., Kiddle, C., Sanchez-Azofeifa, G.A.,
2308 Thayer, D.R., Vescovo, L., Gianelle, D., Sims, D.A., Rahman, A.F., Pastorello, G.Z.
2309 2010. SpecNet revisited: bridging flux and remote sensing communities. *Canadian*
2310 *Journal of Remote Sensing,* 36, S376-S390.
2311 Gamon, J.A., Serrano, L., Surfus, J.S. 1997. The photochemical reflectance index: an optical
2312 indicator of photosynthetic radiation use efficiency across species, functional types, and
2313 nutrient levels. *Oecologia,* 112, 492-501.
2314 Gao, B.C. 1996. NDWI - A normalized difference water index for remote sensing of vegetation
2315 liquid water from space. *Remote Sensing of Environment,* 58, 257-266.
2316 Gao, Y.N., Yu, G.R., Li, S.G., Yan, H.M., Zhu, X.J., Wang, Q.F., Shi, P.L., Zhao, L., Li, Y.N.,
2317 Zhang, F.W., Wang, Y.F., Zhang, J.H. 2015. A remote sensing model to estimate
2318 ecosystem respiration in Northern China and the Tibetan Plateau. *Ecological Modelling,*
2319 304, 34-43.
2320 Garestier, F., Dubois-Fernandez, P.C., Papathanassiou, K.P. 2008. Pine forest height inversion
2321 using single-pass X-band PolInSAR data. *IEEE Transactions on Geoscience and Remote*
2322 *Sensing,* 46, 59-68.
2323 Gaveau, D.L.A. 2002. Modelling the dynamics of ERS-1/2 coherence with increasing woody
2324 biomass over boreal forests. *International Journal of Remote Sensing,* 23, 3879-3885.
2325 Gitelson, A.A. 2004. Wide dynamic range vegetation index for remote quantification of
2326 biophysical characteristics of vegetation. *Journal of Plant Physiology,* 161, 165-173.

2327 Glenn, E.P., Huete, A.R., Nagler, P.L., Nelson, S.G. 2008. Relationship between remotely-
2328 sensed vegetation indices, canopy attributes and plant physiological processes: What
2329 vegetation indices can and cannot tell us about the landscape. *Sensors,* 8, 2136-2160.
2330 Glenn, N.F., Neuenschwander, A., Vierling, L.A., Spaete, L., Li, A.H., Shinneman, D.J., Pilliod,
2331 D.S., Arkle, R.S., McIlroy, S.K. 2016. Landsat 8 and ICESat-2: Performance and
2332 potential synergies for quantifying dryland ecosystem vegetation cover and biomass.
2333 *Remote Sensing of Environment,* 185, 233-242.
2334 Goetz, S., Dubayah, R. 2011. Advances in remote sensing technology and implications for
2335 measuring and monitoring forest carbon stocks and change. *Carbon Management,* 2, 231-
2336 244.
2337 GOFC-GOLD (2016). A sourcebook of methods and procedures for monitoring and reporting
2338 anthropogenic greenhouse gas emissions and removals associated with deforestation,
2339 gains and losses of carbon stocks in forests remaining forests, and forestation. In: GOFC-
2340 GOLD Report version COP22-1, (GOFC-GOLD Land Cover Project Office,
2341 Wageningen University, The Netherlands).
2342 Gomez, C., Lagacherie, P. (2016). Mapping of primary soil properties using optical visible and
2343 near infrared (Vis-NIR) remote sensing. In N. Baghdadi, & M. Zribi (Eds.), *Land Surface*
2344 *Remote Sensing in Agriculture and Forest* (pp. 1-35): Elsevier.
2345 Gomez, C., Rossel, R.A.V., McBratney, A.B. 2008. Soil organic carbon prediction by
2346 hyperspectral remote sensing and field vis-NIR spectroscopy: An Australian case study.
2347 *Geoderma,* 146, 403-411.
2348 Gorelick, N., Hancher, M., Dixon, M., Ilyushchenko, S., Thau, D., Moore, R. 2017. Google
2349 Earth Engine: Planetary-scale geospatial analysis for everyone. *Remote Sensing of*
2350 *Environment,* 202, 18-27.
2351 Goward, S.N., Huemmrich, K.F. 1992. Vegetation canopy PAR absorptance and the normalized
2352 difference vegetation index: An assessment using the SAIL model. *Remote Sensing of*
2353 *Environment,* 39, 119-140.
2354 Goward, S.N., Tucker, C.J., Dye, D.G. 1985. North American vegetation patterns observed with
2355 the NOAA-7 advanced very high resolution radiometer. *Vegetatio,* 64, 3-14.
2356 Gray, J.M., Bishop, T.F.A., Wilson, B.R. 2015. Factors controlling soil organic carbon stocks
2357 with depth in eastern Australia. *Soil Science Society of America Journal,* 79, 1741-1751.
2358 Greenberg, J.A., Dobrowski, S.Z., Ustin, S.L. 2005. Shadow allometry: Estimating tree structural
2359 parameters using hyperspatial image analysis. *Remote Sensing of Environment,* 97, 15-25.
2360 Grinand, C., Le Maire, G., Vieilledent, G., Razakarnanarivo, H., Razafimbelo, T., Bernoux, M.
2361 2017. Estimating temporal changes in soil carbon stocks at ecoregional scale in
2362 Madagascar using remote-sensing. *International Journal of Applied Earth Observation*
2363 *and Geoinformation,* 54, 1-14.
2364 Gu, L., Wood, J.D., Chang, C.Y.Y., Sun, Y., Riggs, J.S. 2019. Advancing terrestrial ecosystem
2365 science with a novel automated measurement system for sun-induced chlorophyll
2366 fluorescence for integration with eddy covariance flux networks. *Journal of Geophysical*
2367 *Research-Biogeosciences,* 124, 127-146.
2368 Gu, L.H., Baldocchi, D., Verma, S.B., Black, T.A., Vesala, T., Falge, E.M., Dowty, P.R. 2002.
2369 Advantages of diffuse radiation for terrestrial ecosystem productivity. *Journal of*
2370 *Geophysical Research-Atmospheres,* 107, D6, 4050,10.1029/2001JD001242.
2371 Guan, K.Y., Pan, M., Li, H.B., Wolf, A., Wu, J., Medvigy, D., Caylor, K.K., Sheffield, J., Wood,
2372 E.F., Malhi, Y., Liang, M.L., Kimball, J.S., Saleska, S.R., Berry, J., Joiner, J., Lyapustin,

A.I. 2015. Photosynthetic seasonality of global tropical forests constrained by hydroclimate. *Nature Geoscience,* 8, 284-289.

Guanter, L., Aben, I., Tol, P., Krijger, J.M., Hollstein, A., Kohler, P., Damm, A., Joiner, J., Frankenberg, C., Landgraf, J. 2015a. Potential of the TROPOspheric Monitoring Instrument (TROPOMI) onboard the Sentinel-5 Precursor for the monitoring of terrestrial chlorophyll fluorescence. *Atmospheric Measurement Techniques,* 8, 1337-1352.

Guanter, L., Frankenberg, C., Dudhia, A., Lewis, P.E., Gomez-Dans, J., Kuze, A., Suto, H., Grainger, R.G. 2012. Retrieval and global assessment of terrestrial chlorophyll fluorescence from GOSAT space measurements. *Remote Sensing of Environment,* 121, 236-251.

Guanter, L., Kaufmann, H., Segl, K., Foerster, S., Rogass, C., Chabrillat, S., Kuester, T., Hollstein, A., Rossner, G., Chlebek, C., Straif, C., Fischer, S., Schrader, S., Storch, T., Heiden, U., Mueller, A., Bachmann, M., Muhle, H., Muller, R., Habermeyer, M., Ohndorf, A., Hill, J., Buddenbaum, H., Hostert, P., van der Linden, S., Leitao, P.J., Rabe, A., Doerffer, R., Krasemann, H., Xi, H.Y., Mauser, W., Hank, T., Locherer, M., Rast, M., Staenz, K., Sang, B. 2015b. The EnMAP spaceborne imaging spectroscopy mission for earth observation. *Remote Sensing,* 7, 8830-8857.

Guanter, L., Zhang, Y.G., Jung, M., Joiner, J., Voigt, M., Berry, J.A., Frankenberg, C., Huete, A.R., Zarco-Tejada, P., Lee, J.E., Moran, M.S., Ponce-Campos, G., Beer, C., Camps-Valls, G., Buchmann, N., Gianelle, D., Klumpp, K., Cescatti, A., Baker, J.M., Griffis, T.J. 2014. Global and time-resolved monitoring of crop photosynthesis with chlorophyll fluorescence. *Proceedings of the National Academy of Sciences of the United States of America,* 111, E1327-E1333.

Guerlet, S., Basu, S., Butz, A., Krol, M., Hahne, P., Houweling, S., Hasekamp, O.P., Aben, I. 2013. Reduced carbon uptake during the 2010 Northern Hemisphere summer from GOSAT. *Geophysical Research Letters,* 40, 2378-2383.

Guo, L., Zhang, H., Shi, T., Chen, Y., Jiang, Q., Linderman, M. 2019. Prediction of soil organic carbon stock by laboratory spectral data and airborne hyperspectral images. *Geoderma,* 337, 32-41.

Gwenzi, D., Lefsky, M.A., Suchdeo, V.P., Harding, D.J. 2016. Prospects of the ICESat-2 laser altimetry mission for savanna ecosystem structural studies based on airborne simulation data. *ISPRS Journal of Photogrammetry and Remote Sensing,* 118, 68-82.

Hall, F.G., Shimabukuro, Y.E., Huemmrich, K.F. 1995. Remote sensing of forest biophysical structure using mixture decomposition and geometric reflectance models. *Ecological Applications,* 5, 993-1013.

Hall, R.J., Skakun, R.S., Arsenault, E.J., Case, B.S. 2006. Modeling forest stand structure attributes using Landsat ETM+ data: Application to mapping of aboveground biomass and stand volume. *Forest Ecology and Management,* 225, 378-390.

Hansen, M.C., Potapov, P.V., Moore, R., Hancher, M., Turubanova, S.A., Tyukavina, A., Thau, D., Stehman, S.V., Goetz, S.J., Loveland, T.R., Kommareddy, A., Egorov, A., Chini, L., Justice, C.O., Townshend, J.R.G. 2013. High-resolution global maps of 21st-century forest cover change. *Science,* 342, 850-853.

Hargrove, W.W., Spruce, J.P., Gasser, G.E., Hoffman, F.M. 2009. Toward a national early warning system for forest disturbances using remotely sensed canopy phenology. *Photogrammetric Engineering and Remote Sensing,* 75, 1150-1156.

Harrell, P.A., BourgeauChavez, L.L., Kasischke, E.S., French, N.H.F., Christensen, N.L. 1995. Sensitivity of ERS-1 and JERS-1 radar data to biomass and stand structure in Alaskan boreal forest. *Remote Sensing of Environment,* 54, 247-260.

Hauglin, M., Astrup, R., Gobakken, T., Naesset, E. 2013. Estimating single-tree branch biomass of Norway spruce with terrestrial laser scanning using voxel-based and crown dimension features. *Scandinavian Journal of Forest Research,* 28, 456-469.

Hazarika, M.K., Yasuoka, Y., Ito, A., Dye, D. 2005. Estimation of net primary productivity by integrating remote sensing data with an ecosystem model. *Remote Sensing of Environment,* 94, 298-310.

Hbirkou, C., Patzold, S., Mahlein, A.K., Welp, G. 2012. Airborne hyperspectral imaging of spatial soil organic carbon heterogeneity at the field-scale. *Geoderma,* 175, 21-28.

He, M.Z., Kimball, J.S., Maneta, M.P., Maxwell, B.D., Moreno, A., Begueria, S., Wu, X.C. 2018. Regional crop gross primary productivity and yield estimation using fused Landsat-MODIS data. *Remote Sensing,* 10, 10(3), 372; https://doi.org/10.3390/rs10030372.

Heinsch, F.A., Zhao, M.S., Running, S.W., Kimball, J.S., Nemani, R.R., Davis, K.J., Bolstad, P.V., Cook, B.D., Desai, A.R., Ricciuto, D.M., Law, B.E., Oechel, W.C., Kwon, H., Luo, H.Y., Wofsy, S.C., Dunn, A.L., Munger, J.W., Baldocchi, D.D., Xu, L.K., Hollinger, D.Y., Richardson, A.D., Stoy, P.C., Siqueira, M.B.S., Monson, R.K., Burns, S.P., Flanagan, L.B. 2006. Evaluation of remote sensing based terrestrial productivity from MODIS using regional tower eddy flux network observations. *IEEE Transactions on Geoscience and Remote Sensing,* 44, 1908-1925.

Heiskanen, J. 2006. Estimating aboveground tree biomass and leaf area index in a mountain birch forest using ASTER satellite data. *International Journal of Remote Sensing,* 27, 1135-1158.

Heller, R.C. 1968. Previsual detection of ponderosa pine trees dying from bark beetle attack. *Proceeds of the Fifth Symposium on Remote Sensing of Environment, University of Michigan, Ann Arbor, MI*, 387-434.

Hesslerová, P., Huryna, H., Pokorný, J., Procházka, J. 2018. The effect of forest disturbance on landscape temperature. *Ecological Engineering,* 120, 345-354.

Hicke, J.A., Asner, G.P., Kasiske, E.S., French, N.H.F., Randerson, J.T., Collatz, G.J., Stocks, B.J., Tucker, C.J., Los, S.O., Field, C.B. 2003. Postfire response of North American boreal forest net primary productivity analyzed with satellite observations. *Global Change Biology,* 9, 1145-1157.

Hicke, J.A., Logan, J.A. 2009. Mapping whitebark pine mortality caused by a mountain pine beetle outbreak with high spatial resolution satellite imagery. *International Journal of Remote Sensing,* 30, 4427-4441.

Hicke, J.A., Meddens, A.J.H., Allen, C.D., Kolden, C.A. 2013. Carbon stocks of trees killed by bark beetles and wildfire in the western United States. *Environmental Research Letters,* 8, 035032.

Hilker, T., Coops, N.C., Wulder, M.A., Black, T.A., Guy, R.D. 2008. The use of remote sensing in light use efficiency based models of gross primary production: A review of current status and future requirements. *Science of the Total Environment,* 404, 411-423.

Hilton, T.W., Davis, K.J., Keller, K. 2014. Evaluating terrestrial CO2 flux diagnoses and uncertainties from a simple land surface model and its residuals. *Biogeosciences,* 11, 217-235.

Houghton, R.A., Butman, D., Bunn, A.G., Krankina, O.N., Schlesinger, P., Stone, T.A. 2007. Mapping Russian forest biomass with data from satellites and forest inventories. *Environmental Research Letters,* 2, 045032, doi:10.1088/1748-9326/2/4/045032.

Huang, C.Y., Asner, G.P., Barger, N.N., Neff, J.C., Floyd, M.L. 2010. Regional aboveground live carbon losses due to drought-induced tree dieback in pinon-juniper ecosystems. *Remote Sensing of Environment,* 114, 1471-1479.

Huang, N., Gu, L.H., Niu, Z. 2014. Estimating soil respiration using spatial data products: A case study in a deciduous broadleaf forest in the Midwest USA. *Journal of Geophysical Research-Atmospheres,* 119, 6393-6408.

Huang, X., Xiao, J., Ma, M. (2019) Evaluating the performance of satellite-derived vegetation indices for estimating gross primary productivity using FLUXNET observations across the globe. *Remote Sensing*, 11(15), 1823; https://doi.org/10.3390/rs11151823.

Huete, A., Didan, K., Miura, T., Rodriguez, E.P., Gao, X., Ferreira, L.G. 2002. Overview of the radiometric and biophysical performance of the MODIS vegetation indices. *Remote Sensing of Environment,* 83, 195-213.

Huete, A.R., Didan, K., Shimabukuro, Y.E., Ratana, P., Saleska, S.R., Hutyra, L.R., Yang, W.Z., Nemani, R.R., Myneni, R. 2006. Amazon rainforests green-up with sunlight in dry season. *Geophysical Research Letters,* 33, L06405, doi:10.1029/2005GL025583.

Huete, A.R., Jackson, R.D., Post, D.F. 1985. Spectral response of a plant canopy with different soil backgorund. *Remote Sensing of Environment,* 17, 37-53.

Huete, A.R., Restrepo-Coupe, N., Ratana, P., Didan, K., Saleska, S.R., Ichii, K., Panuthai, S., Gamo, M. 2008. Multiple site tower flux and remote sensing comparisons of tropical forest dynamics in Monsoon Asia. *Agricultural and Forest Meteorology,* 148, 748-760.

Hunt, G.R., Salisbury, J.W., Lenhoff, C.J. 1971. Visible and near-infrared spectra of minerals and rocks : III. Oxides and hydroxides. *Modern Geology,* 2, 195–205.

Huntzinger, D.N., Post, W.M., Wei, Y., Michalak, A.M., West, T.O., Jacobson, A.R., Baker, I.T., Chen, J.M., Davis, K.J., Hayes, D.J., Hoffman, F.M., Jain, A.K., Liu, S., McGuire, A.D., Neilson, R.P., Potter, C., Poulter, B., Price, D., Raczka, B.M., Tian, H.Q., Thornton, P., Tomelleri, E., Viovy, N., Xiao, J., Yuan, W., Zeng, N., Zhao, M., Cook, R. 2012. North American Carbon Program (NACP) regional interim synthesis: Terrestrial biospheric model intercomparison. *Ecological Modelling,* 232, 144-157.

Hyde, P., Nelson, R., Kimes, D., Levine, E. 2007. Exploring LIDAR-RaDAR synergy - predicting aboveground biomass in a southwestern ponderosa pine forest using LiDAR, SAR and InSAR. *Remote Sensing of Environment,* 106, 28-38.

Ichii, K., Hashimoto, H., White, M.A., Potters, C., Hutyra, L.R., Huete, A.R., Myneni, R.B., Nemanis, R.R. 2007. Constraining rooting depths in tropical rainforests using satellite data and ecosystem modeling for accurate simulation of gross primary production seasonality. *Global Change Biology,* 13, 67-77.

Ichii, K., Kondo, M., Lee, Y.H., Wang, S.Q., Kim, J., Ueyama, M., Lim, H.J., Shi, H., Suzuki, T., Ito, A., Kwon, H., Ju, W.M., Huang, M., Sasai, T., Asanuma, J., Han, S.J., Hirano, T., Hirata, R., Kato, T., Li, S.G., Li, Y.N., Maeda, T., Miyata, A., Matsuura, Y., Murayama, S., Nakai, Y., Ohta, T., Saitoh, T.M., Saigusa, N., Takagi, K., Tang, Y.H., Wang, H.M., Yu, G.R., Zhang, Y.P., Zhao, F.H. 2013. Site-level model-data synthesis of terrestrial carbon fluxes in the CarboEastAsia eddy-covariance observation network: toward future modeling efforts. *Journal of Forest Research,* 18, 13-20.

Ichii, K., Suzuki, T., Kato, T., Ito, A., Hajima, T., Ueyama, M., Sasai, T., Hirata, R., Saigusa, N., Ohtani, Y., Takagi, K. 2010. Multi-model analysis of terrestrial carbon cycles in Japan: limitations and implications of model calibration using eddy flux observations. *Biogeosciences,* 7, 2061-2080.

Ichii, K., Ueyama, M., Kondo, M., Saigusa, N., Kim, J., Alberto, M.C., Ardo, J., Euskirchen, E.S., Kang, M., Hirano, T., Joiner, J., Kobayashi, H., Marchesini, L.B., Merbold, L., Miyata, A., Saitoh, T.M., Takagi, K., Varlagin, A., Bret-Harte, M.S., Kitamura, K., Kosugi, Y., Kotani, A., Kumar, K., Li, S.G., Machimura, T., Matsuura, Y., Mizoguchi, Y., Ohta, T., Mukherjee, S., Yanagi, Y., Yasuda, Y., Zhang, Y.P., Zhao, F.H. 2017. New data-driven estimation of terrestrial CO2 fluxes in Asia using a standardized database of eddy covariance measurements, remote sensing data, and support vector regression. *Journal of Geophysical Research-Biogeosciences,* 122, 767-795.

Ichii, K., Wang, W.L., Hashimoto, H., Yang, F.H., Votava, P., Michaelis, A.R., Nemani, R.R. 2009. Refinement of rooting depths using satellite-based evapotranspiration seasonality for ecosystem modeling in California. *Agricultural and Forest Meteorology,* 149, 1907-1918.

IPCC (2013). *Climate Change 2013: The Physical Science Basis. Contribution of Working Group I to the Fifth Assessment Report of the Intergovernmental Panel on Climate Change*. Cambridge, United Kingdom and New York, NY, USA: Cambridge University Press.

Jagermeyr, J., Gerten, D., Lucht, W., Hostert, P., Migliavacca, M., Nemani, R. 2014. A high-resolution approach to estimating ecosystem respiration at continental scales using operational satellite data. *Global Change Biology,* 20, 1191-1210.

James, M.E., Kalluri, S.N.V. 1994. The Pathfinder AVHRR land data set - an improved coarse resolution data set for terrestrial monitoring. *International Journal of Remote Sensing,* 15, 3347-3363.

Jarmer, T., Hill, J., Lavee, H., Sarah, P. 2010. Mapping topsoil organic carbon in non-agricultural semi-arid and arid ecosystems of Israel. *Photogrammetric Engineering and Remote Sensing,* 76, 85-94.

Jasinski, M.F., Crago, R.D. 1999. Estimation of vegetation aerodynamic roughness of natural regions using frontal area density determined from satellite imagery. *Agricultural and Forest Meteorology,* 94, 65-77.

Jenkins, J.C., Chojnacky, D.C., Heath, L.S., Birdsey, R.A. 2003. National-scale biomass estimators for United States tree species. *Forest Science,* 49, 12-35.

Jeong, S.J., Schimel, D., Frankenberg, C., Drewry, D.T., Fisher, J.B., Verma, M., Berry, J.A., Lee, J.E., Joiner, J. 2017. Application of satellite solar-induced chlorophyll fluorescence to understanding large-scale variations in vegetation phenology and function over northern high latitude forests. *Remote Sensing of Environment,* 190, 178-187.

Jepsen, J.U., Hagen, S.B., Hogda, K.A., Ims, R.A., Karlsen, S.R., Tommervik, H., Yoccoz, N.G. 2009. Monitoring the spatio-temporal dynamics of geometrid moth outbreaks in birch forest using MODIS-NDVI data. *Remote Sensing of Environment,* 113, 1939-1947.

John, R., Chen, J.Q., Giannico, V., Park, H., Xiao, J.F., Shirkey, G., Ouyang, Z.T., Shao, C.L., Lafortezza, R., Qi, J.G. 2018. Grassland canopy cover and aboveground biomass in Mongolia and Inner Mongolia: Spatiotemporal estimates and controlling factors. *Remote Sensing of Environment,* 213, 34-48.

2553 Joiner, J., Guanter, L., Lindstrot, R., Voigt, M., Vasilkov, A.P., Middleton, E.M., Huemmrich,
2554 K.F., Yoshida, Y., Frankenberg, C. 2013. Global monitoring of terrestrial chlorophyll
2555 fluorescence from moderate-spectral-resolution near-infrared satellite measurements:
2556 methodology, simulations, and application to GOME-2. *Atmospheric Measurement*
2557 *Techniques,* 6, 2803-2823.
2558 Joiner, J., Yoshida, Y., Guanter, L., Middleton, E.M. 2016. New methods for the retrieval of
2559 chlorophyll red fluorescence from hyperspectral satellite instruments: simulations and
2560 application to GOME-2 and SCIAMACHY. *Atmospheric Measurement Techniques,* 9,
2561 3939-3967.
2562 Joiner, J., Yoshida, Y., Vasilkov, A., Schaefer, K., Jung, M., Guanter, L., Zhang, Y., Garrity, S.,
2563 Middleton, E.M., Huemmrich, K.F., Gu, L., Marchesini, L.B. 2014. The seasonal cycle of
2564 satellite chlorophyll fluorescence observations and its relationship to vegetation
2565 phenology and ecosystem atmosphere carbon exchange. *Remote Sensing of Environment,*
2566 152, 375-391.
2567 Joiner, J., Yoshida, Y., Vasilkov, A.P., Middleton, E.M., Campbell, P.K.E., Yoshida, Y., Kuze,
2568 A., Corp, L.A. 2012. Filling-in of near-infrared solar lines by terrestrial fluorescence and
2569 other geophysical effects: simulations and space-based observations from SCIAMACHY
2570 and GOSAT. *Atmospheric Measurement Techniques,* 5, 809-829.
2571 Joiner, J., Yoshida, Y., Vasilkov, A.P., Yoshida, Y., Corp, L.A., Middleton, E.M. 2011. First
2572 observations of global and seasonal terrestrial chlorophyll fluorescence from space.
2573 *Biogeosciences,* 8, 637-651.
2574 Jones, L.A., Kimball, J.S., Reichle, R.H., Madani, N., Glassy, J., Ardizzone, J.V., Colliander, A.,
2575 Cleverly, J., Desai, A.R., Eamus, D., Euskirchen, E.S., Hutley, L., Macfarlane, C., Scott,
2576 R.L. 2017. The SMAP Level 4 carbon product for monitoring ecosystem land-
2577 atmosphere CO_2 exchange. *IEEE Transactions on Geoscience and Remote Sensing,* 55,
2578 6517-6532.
2579 Jung, M., Reichstein, M., Bondeau, A. 2009. Towards global empirical upscaling of FLUXNET
2580 eddy covariance observations: validation of a model tree ensemble approach using a
2581 biosphere model. *Biogeosciences,* 6, 2001-2013.
2582 Jung, M., Reichstein, M., Margolis, H.A., Cescatti, A., Richardson, A.D., Arain, M.A., Arneth,
2583 A., Bernhofer, C., Bonal, D., Chen, J.Q., Gianelle, D., Gobron, N., Kiely, G., Kutsch, W.,
2584 Lasslop, G., Law, B.E., Lindroth, A., Merbold, L., Montagnani, L., Moors, E.J., Papale,
2585 D., Sottocornola, M., Vaccari, F., Williams, C. 2011. Global patterns of land-atmosphere
2586 fluxes of carbon dioxide, latent heat, and sensible heat derived from eddy covariance,
2587 satellite, and meteorological observations. *Journal of Geophysical Research-*
2588 *Biogeosciences,* 116, G00J07,doi:10.1029/2010JG001566.
2589 Justice, C.O., Giglio, L., Korontzi, S., Owens, J., Morisette, J.T., Roy, D., Descloitres, J.,
2590 Alleaume, S., Petitcolin, F., Kaufman, Y. 2002. The MODIS fire products. *Remote*
2591 *Sensing of Environment,* 83, 244-262.
2592 Justice, C.O., Roman, M.O., Csiszar, I., Vermote, E.F., Wolfe, R.E., Hook, S.J., Friedl, M.,
2593 Wang, Z.S., Schaaf, C.B., Miura, T., Tschudi, M., Riggs, G., Hall, D.K., Lyapustin, A.I.,
2594 Devadiga, S., Davidson, C., Masuoka, E.J. 2013. Land and cryosphere products from
2595 Suomi NPP VIIRS: Overview and status. *Journal of Geophysical Research-Atmospheres,*
2596 118, 9753-9765.

Kampe, T.U., Johnson, B.R., Kuester, M., Keller, M. 2010. NEON: the first continental-scale ecological observatory with airborne remote sensing of vegetation canopy biochemistry and structure. *Journal of Applied Remote Sensing,* 4, 043510.

Kankare, V., Holopainen, M., Vastaranta, M., Puttonen, E., Yu, X.W., Hyyppa, J., Vaaja, M., Hyyppa, H., Alho, P. 2013. Individual tree biomass estimation using terrestrial laser scanning. *ISPRS Journal of Photogrammetry and Remote Sensing,* 75, 64-75.

Karila, K., Yu, X.W., Vastaranta, M., Karjalainen, M., Puttonen, E., Hyyppa, J. 2019. TanDEM-X digital surface models in boreal forest above-ground biomass change detection. *ISPRS Journal of Photogrammetry and Remote Sensing,* 148, 174-183.

Karion, A., Sweeney, C., Tans, P., Newberger, T. 2010. AirCore: An Innovative Atmospheric Sampling System. *Journal of Atmospheric and Oceanic Technology,* 27, 1839-1853.

Karlson, M., Ostwald, M., Reese, H., Sanou, J., Tankoano, B., Mattsson, E. 2015. Mapping tree canopy cover and aboveground biomass in Sudano-Sahelian woodlands using Landsat 8 and random forest. *Remote Sensing,* 7, 10017-10041.

Kasischke, E.S., Christensen, N.L., Bourgeauchavez, L.L. 1995. Correlating radar backscatter with components of biomass in loblolly-pine forests. *IEEE Transactions on Geoscience and Remote Sensing,* 33, 643-659.

Kasischke, E.S., Goetz, S.J., Kimball, J.S., Mack, M.M. (2010). The Arctic-Boreal Vulnerability Experiment (ABoVE): A Concise Plan for a NASA-Sponsored Field Campaign. In. http://cce.nasa.gov/terrestrial_ecology/pdfs/ABoVE%20Final%20Report.pdf

Kasischke, E.S., Tanase, M.A., Bourgeau-Chavez, L.L., Borr, M. 2011. Soil moisture limitations on monitoring boreal forest regrowth using spaceborne L-band SAR data. *Remote Sensing of Environment,* 115, 227-232.

Kato, T., Knorr, W., Scholze, M., Veenendaal, E., Kaminski, T., Kattge, J., Gobron, N. 2013. Simultaneous assimilation of satellite and eddy covariance data for improving terrestrial water and carbon simulations at a semi-arid woodland site in Botswana. *Biogeosciences,* 10, 789-802.

Kauth, R.J., Thomas, G.S. (1976). The tasseled cap. A graphic description of the spectral-temporal development of agricultural crops as seen by Landsat. In, *2nd International Symposium on Machine Processing of Remotely Sensed Data, IEEE Cat. 76, CH-1103-1, Purdue University, West Lafayette, IN and Proc. of LACIE Symp., Houston, TX.*

Kellndorfer, J., Walker, W., LaPoint, L., Bishop, J., Cormier, T., Fiske, G., Kirsch, K., Westfall, J. (2013). NACP Aboveground Biomass and Carbon Baseline Data, V.2 (NBCD 2000), U.S.A., 2000. In. ORNL DAAC, Oak Ridge, Tennessee, USA. https://doi.org/10.3334/ORNLDAAC/1161

Khati, U., Singh, G., Ferro-Famil, L. 2017. Analysis of seasonal effects on forest parameter estimation of Indian deciduous forest using TerraSAR-X PolInSAR acquisitions. *Remote Sensing of Environment,* 199, 265-276.

Kimball, J.S., Jones, L.A., Zhang, K., Heinsch, F.A., McDonald, K.C., Oechel, W.C. 2009. A satellite approach to estimate land-atmosphere CO2 exchange for boreal and Arctic biomes using MODIS and AMSR-E. *IEEE Transactions on Geoscience and Remote Sensing,* 47, 569-587.

King, D.A., Turner, D.P., Ritts, W.D. 2011. Parameterization of a diagnostic carbon cycle model for continental scale application. *Remote Sensing of Environment, 115*, 1653-1664.

Kleidon, A. 2004. Global datasets of rooting zone depth inferred from inverse methods. *Journal of Climate,* 17, 2714-2722.

Kohler, P., Frankenberg, C., Magney, T.S., Guanter, L., Joiner, J., Landgraf, J. 2018. Global retrievals of solar-induced chlorophyll fluorescence with TROPOMI: First results and intersensor comparison to OCO-2. *Geophysical Research Letters,* 45, 10456-10463.

Kohler, P., Guanter, L., Joiner, J. 2015. A linear method for the retrieval of sun-induced chlorophyll fluorescence from GOME-2 and SCIAMACHY data. *Atmospheric Measurement Techniques,* 8, 2589-2608.

Kondo, M., Ichii, K., Takagi, H., Sasakawa, M. 2015. Comparison of the data-driven top-down and bottom-up global terrestrial CO2 exchanges: GOSAT CO2 inversion and empirical eddy flux upscaling. *Journal of Geophysical Research-Biogeosciences,* 120, 1226-1245.

Krol, M., de Bruine, M., Killaars, L., Ouwersloot, H., Pozzer, A., Yin, Y., Chevallier, F., Bousquet, P., Patra, P., Belikov, D., Maksyutov, S., Dhomse, S., Feng, W.H., Chipperfield, M.P. 2018. Age of air as a diagnostic for transport timescales in global models. *Geoscientific Model Development,* 11, 3109-3130.

Kulawik, S.S., Jones, D.B.A., Nassar, R., Irion, F.W., Worden, J.R., Bowman, K.W., Machida, T., Matsueda, H., Sawa, Y., Biraud, S.C., Fischer, M.L., Jacobson, A.R. 2010. Characterization of Tropospheric Emission Spectrometer (TES) CO2 for carbon cycle science. *Atmospheric Chemistry and Physics,* 10, 5601-5623.

Ladoni, M., Bahrami, H.A., Alavipanah, S.K., Norouzi, A.A. 2010. Estimating soil organic carbon from soil reflectance: a review. *Precision Agriculture,* 11, 82-99.

Laraby, K.G., Schott, J.R. 2018. Uncertainty estimation method and Landsat 7 global validation for the Landsat surface temperature product. *Remote Sensing of Environment,* 216, 472-481.

Larsson, H. 1993. Linear regression for canopy cover estimation in Acacia woodlands using Landsat-TM, -MSS, and SPOT HRV XS data. *International Journal of Remote Sensing,* 14, 2129-2136.

Le Quere, C., Raupach, M.R., Canadell, J.G., Marland, G., Bopp, L., Ciais, P., Conway, T.J., Doney, S.C., Feely, R.A., Foster, P., Friedlingstein, P., Gurney, K., Houghton, R.A., House, J.I., Huntingford, C., Levy, P.E., Lomas, M.R., Majkut, J., Metzl, N., Ometto, J.P., Peters, G.P., Prentice, I.C., Randerson, J.T., Running, S.W., Sarmiento, J.L., Schuster, U., Sitch, S., Takahashi, T., Viovy, N., van der Werf, G.R., Woodward, F.I. 2009. Trends in the sources and sinks of carbon dioxide. *Nature Geoscience,* 2, 831-836.

Le Toan, T., Beaudoin, A., Riom, J., Guyon, D. 1992. Relating forest biomass to SAR data. *IEEE Transactions on Geoscience and Remote Sensing,* 30, 403-411.

Le Toan, T., Quegan, S., Davidson, M.W.J., Balzter, H., Paillou, P., Papathanassiou, K., Plummer, S., Rocca, F., Saatchi, S., Shugart, H., Ulander, L. 2011. The BIOMASS mission: Mapping global forest biomass to better understand the terrestrial carbon cycle. *Remote Sensing of Environment,* 115, 2850-2860.

Leboeuf, A., Beaudoin, A., Fournier, R.A., Guindon, L., Luther, J.E., Lambert, M.C. 2007. A shadow fraction method for mapping biomass of northern boreal black spruce forests using QuickBird imagery. *Remote Sensing of Environment,* 110, 488-500.

Lee, C.M., Cable, M.L., Hook, S.J., Green, R.O., Ustin, S.L., Mandl, D.J., Middleton, E.M. 2015a. An introduction to the NASA Hyperspectral InfraRed Imager (HyspIRI) mission and preparatory activities. *Remote Sensing of Environment,* 167, 6-19.

Lee, J.E., Berry, J.A., Van der Tol, C.S., Yang, X., Guanter, L., Damm, A., Baker, I., Frankenberg, C. 2015b. Simulations of chlorophyll fluorescence incorporated into the Community Land Model version 4. *Global Change Biology,* 21, 3469-3477.

Lee, J.E., Frankenberg, C., van der Tol, C., Berry, J.A., Guanter, L., Boyce, C.K., Fisher, J.B., Morrow, E., Worden, J.R., Asefi, S., Badgley, G., Saatchi, S. 2013. Forest productivity and water stress in Amazonia: observations from GOSAT chlorophyll fluorescence. *Proceedings of the Royal Society B-Biological Sciences,* 280, 20130171, http://dx.doi.org/10.1098/rspb.2013.0171.

Lefsky, M.A., Harding, D., Cohen, W.B., Parker, G., Shugart, H.H. 1999. Surface lidar remote sensing of basal area and biomass in deciduous forests of eastern Maryland, USA. *Remote Sensing of Environment,* 67, 83-98.

Lefsky, M.A., Harding, D.J., Keller, M., Cohen, W.B., Carabajal, C.C., Espirito-Santo, F.D., Hunter, M.O., de Oliveira, R. 2005. Estimates of forest canopy height and aboveground biomass using ICESat. *Geophysical Research Letters,* 32, L22S02, doi:10.1029/2005GL023971.

Lefsky, M.A., Keller, M., Pang, Y., de Camargo, P.B., Hunter, M.O. 2007. Revised method for forest canopy height estimation from Geoscience Laser Altimeter System waveforms. *Journal of Applied Remote Sensing,* 1, 013537.

Li, A.H., Dhakal, S., Glenn, N.F., Spaete, L.P., Shinneman, D.J., Pilliod, D.S., Arkle, R.S., McIlroy, S.K. 2017. Lidar aboveground vegetation biomass estimates in shrublands: prediction, uncertainties and application to coarser scales. *Remote Sensing,* 9, 903; doi:10.3390/rs9090903.

Li, X., Xiao, J.F. 2019. A global, 0.05-degree product of solar-induced chlorophyll fluorescence derived from OCO-2, MODIS, and reanalysis data. *Remote Sensing,* 11(5), 517; https://doi.org/10.3390/rs11050517.

Li, X., Xiao, J.F., He, B.B. 2018a. Higher absorbed solar radiation partly offset the negative effects of water stress on the photosynthesis of Amazon forests during the 2015 drought. *Environmental Research Letters,* 13, 044005, https://doi.org/10.1088/1748-9326/aab0b1.

Li, X., Xiao, J.F., He, B.B., Arain, M.A., Beringer, J., Desai, A.R., Emmel, C., Hollinger, D.Y., Krasnova, A., Mammarella, I., Noe, S.M., Ortiz, P.S., Rey-Sanchez, A.C., Rocha, A.V., Varlagin, A. 2018b. Solar-induced chlorophyll fluorescence is strongly correlated with terrestrial photosynthesis for a wide variety of biomes: First global analysis based on OCO-2 and flux tower observations. *Global Change Biology,* 24, 3990-4008.

Li, X., Xiao, J.F., He, B.B. 2018c. Chlorophyll fluorescence observed by OCO-2 is strongly related to gross primary productivity estimated from flux towers in temperate forests. *Remote Sensing of Environment,* 204, 659-671.

Li, X.W., Strahler, A.H. 1985. Geometric-optical modeling of a conifer forest canopy. *IEEE Transactions on Geoscience and Remote Sensing,* 23, 705-721.

Liang, X.L., Kankare, V., Hyyppa, J., Wang, Y.S., Kukko, A., Haggren, H., Yu, X.W., Kaartinen, H., Jaakkola, A., Guan, F.Y., Holopainen, M., Vastaranta, M. 2016. Terrestrial laser scanning in forest inventories. *ISPRS Journal of Photogrammetry and Remote Sensing,* 115, 63-77.

Liu, J., Chen, J.M., Cihlar, J., Park, W.M. 1997. A process-based boreal ecosystem productivity simulator using remote sensing inputs. *Remote Sensing of Environment,* 62, 158-175.

Liu, J.J., Bowman, K.W., Schimel, D.S., Parazoo, N.C., Jiang, Z., Lee, M., Bloom, A.A., Wunch, D., Frankenberg, C., Sun, Y., O'Dell, C.W., Gurney, K.R., Menemenlis, D., Gierach, M., Crisp, D., Eldering, A. 2017. Contrasting carbon cycle responses of the tropical continents to the 2015-2016 El Nino. *Science,* 358, 191-+.

Liu, S.G., Bond-Lamberty, B., Hicke, J.A., Vargas, R., Zhao, S.Q., Chen, J., Edburg, S.L., Hu, Y.M., Liu, J.X., McGuire, A.D., Xiao, J.F., Keane, R., Yuan, W.P., Tang, J.W., Luo, Y.Q., Potter, C., Oeding, J. 2011. Simulating the impacts of disturbances on forest carbon cycling in North America: Processes, data, models, and challenges. *Journal of Geophysical Research-Biogeosciences,* 116, G00K08, doi:10.1029/2010JG001585.

Liu, W.T. (2015). SATELLITES AND SATELLITE REMOTE SENSING | Surface Wind and Stress. In G.R. North, J. Pyle, F. Zhang (Eds.), *Encyclopedia of Atmospheric Sciences (Second Edition)* (pp. 138-144). Oxford: Academic Press.

Liu, X., Guanter, L., Liu, L., Damm, A., Malenovsky, Z., Rascher, U., Peng, D., Du, S., Gastellu-Etchegorry, J.-P. 2018a. Downscaling of solar-induced chlorophyll fluorescence from canopy level to photosystem level using a random forest model. *Remote Sensing of Environment,* 231, 110772.

Liu, Y.B., Xiao, J.F., Ju, W.M., Zhu, G.L., Wu, X.C., Fan, W.L., Li, D.Q., Zhou, Y.L. 2018b. Satellite-derived LAI products exhibit large discrepancies and can lead to substantial uncertainty in simulated carbon and water fluxes. *Remote Sensing of Environment,* 206, 174-188.

Liu, Y.Y., van Dijk, A., de Jeu, R.A.M., Canadell, J.G., McCabe, M.F., Evans, J.P., Wang, G.J. 2015. Recent reversal in loss of global terrestrial biomass. *Nature Climate Change,* 5, 470-474.

Lloyd, J., Taylor, J.A. 1994. On the temperature-dependence of soil respiration. *Functional Ecology,* 8, 315-323.

Locatelli, R., Bousquet, P., Hourdin, F., Saunois, M., Cozic, A., Couvreux, F., Grandpeix, J.Y., Lefebvre, M.P., Rio, C., Bergamaschi, P., Chambers, S.D., Karstens, U., Kazan, V., van der Laan, S., Meijer, H.A.J., Moncrieff, J., Ramonet, M., Scheeren, H.A., Schlosser, C., Schmidt, M., Vermeulen, A., Williams, A.G. 2015. Atmospheric transport and chemistry of trace gases in LMDz5B: evaluation and implications for inverse modelling. *Geoscientific Model Development,* 8, 129-150.

Los, S.O., Justice, C.O., Tucker, C.J. 1994. A global 1-degree-by-1-degrees NDVI data set for climate studies derived from the GIMMS continental NDVI data. *International Journal of Remote Sensing,* 15, 3493-3518.

Loveland, T.R., Reed, B.C., Brown, J.F., Ohlen, D.O., Zhu, Z., Yang, L., Merchant, J.W. 2000. Development of a global land cover characteristics database and IGBP DISCover from 1 km AVHRR data. *International Journal of Remote Sensing,* 21, 1303-1330.

Lu, D. 2005. Aboveground biomass estimation using Landsat TM data in the Brazilian Amazon. *International Journal of Remote Sensing,* 26, 2509-2525.

Lu, D., Chen, Q., Wang, G., Moran, E., Batistella, M., Zhang, M., Laurin, G.V., Saah, D. 2012. Aboveground forest biomass estimation with Landsat and LiDAR data and uncertainty analysis of the estimates. *International Journal of Forestry Research,* 436537, doi:10.1155/2012/436537.

Lu, D.S., Mausel, P., Brondizio, E., Moran, E. 2004. Relationships between forest stand parameters and Landsat TM spectral responses in the Brazilian Amazon Basin. *Forest Ecology and Management,* 198, 149-167.

Lu, P., Wang, L., Niu, Z., Li, L.H., Zhang, W.H. 2013. Prediction of soil properties using laboratory VIS-NIR spectroscopy and Hyperion imagery. *Journal of Geochemical Exploration,* 132, 26-33.

Luckman, A., Baker, J., Wegmuller, U. 2000. Repeat-pass interferometric coherence measurements of disturbed tropical forest from JERS and ERS satellites. *Remote Sensing of Environment,* 73, 350-360.

Luus, K.A., Commane, R., Parazoo, N.C., Benmergui, J., Euskirchen, E.S., Frankenberg, C., Joiner, J., Lindaas, J., Miller, C.E., Oechel, W.C., Zona, D., Wofsy, S., Lin, J.C. 2017. Tundra photosynthesis captured by satellite-observed solar-induced chlorophyll fluorescence. *Geophysical Research Letters,* 44, 1564-1573.

Ma, X.L., Huete, A., Yu, Q., Coupe, N.R., Davies, K., Broich, M., Ratana, P., Beringer, J., Hutley, L.B., Cleverly, J., Boulain, N., Eamus, D. 2013. Spatial patterns and temporal dynamics in savanna vegetation phenology across the North Australian Tropical Transect. *Remote Sensing of Environment,* 139, 97-115.

MacBean, N., Maignan, F., Bacour, C., Lewis, P., Peylin, P., Guanter, L., Kohler, P., Gomez-Dans, J., Disney, M. 2018. Strong constraint on modelled global carbon uptake using solar-induced chlorophyll fluorescence data. *Scientific Reports,* 8:1973, DOI:10.1038/s41598-018-20024-w.

Madugundu, R., Nizalapur, V., Jha, C.S. 2008. Estimation of LAI and above-ground biomass in deciduous forests: Western Ghats of Karnataka, India. *International Journal of Applied Earth Observation and Geoinformation,* 10, 211-219.

Mahadevan, P., Wofsy, S.C., Matross, D.M., Xiao, X.M., Dunn, A.L., Lin, J.C., Gerbig, C., Munger, J.W., Chow, V.Y., Gottlieb, E.W. 2008. A satellite-based biosphere parameterization for net ecosystem CO2 exchange: Vegetation Photosynthesis and Respiration Model (VPRM). *Global Biogeochemical Cycles,* 22, GB2005, doi:10.1029/2006GB002735.

Markus, T., Neumann, T., Martino, A., Abdalati, W., Brunt, K., Csatho, B., Farrell, S., Fricker, H., Gardner, A., Harding, D., Jasinski, M., Kwok, R., Magruder, L., Lubin, D., Luthcke, S., Morison, J., Nelson, R., Neuenschwander, A., Palm, S., Popescu, S., Shum, C.K., Schutz, B.E., Smith, B., Yang, Y.K., Zwally, J. 2017. The Ice, Cloud, and land Elevation Satellite-2 (ICESat-2): Science requirements, concept, and implementation. *Remote Sensing of Environment,* 190, 260-273.

Masek, J.G., Collatz, G.J. 2006. Estimating forest carbon fluxes in a disturbed southeastern landscape: Integration of remote sensing, forest inventory, and biogeochemical modeling. *Journal of Geophysical Research-Biogeosciences,* 111, G01006, doi:10.1029/2005JG000062.

Masek, J.G., Huang, C., Wolfe, R., Cohen, W., Hall, F., Kutler, J., Nelson, P. 2008. North American forest disturbance mapped from a decadal Landsat record. *Remote Sensing of Environment,* 112, 2914-2926.

Matasci, G., Hermosilla, T., Wulder, M.A., White, J.C., Coops, N.C., Hobart, G.W., Zald, H.S.J. 2018. Large-area mapping of Canadian boreal forest cover, height, biomass and other structural attributes using Landsat composites and lidar plots. *Remote Sensing of Environment,* 209, 90-106.

McBratney, A.B., Santos, M.L.M., Minasny, B. 2003. On digital soil mapping. *Geoderma,* 117, 3-52.

McCandless, S.W., Jackson, C.R. (2004). Principles of Synthetic Aperture Radar. In C.R. Jackson, & J.R. Apel (Eds.), *Synthetic Aperture Radar Marine User's Manual* (pp. 1-81)

McDowell, N.G., Coops, N.C., Beck, P.S.A., Chambers, J.Q., Gangodagamage, C., Hicke, J.A., Huang, C.-y., Kennedy, R., Krofcheck, D.J., Litvak, M., Meddens, A.J.H., Muss, J.,

Negrón-Juarez, R., Peng, C., Schwantes, A.M., Swenson, J.J., Vernon, L.J., Williams, A.P., Xu, C., Zhao, M., Running, S.W., Allen, C.D. 2015. Global satellite monitoring of climate-induced vegetation disturbances. *Trends in Plant Science,* 20, 114-123.

Meddens, A.J.H., Hicke, J.A. 2014. Spatial and temporal patterns of Landsat-based detection of tree mortality caused by a mountain pine beetle outbreak in Colorado, USA. *Forest Ecology and Management,* 322, 78-88.

Meddens, A.J.H., Hicke, J.A., Vierling, L.A., Hudak, A.T. 2013. Evaluating methods to detect bark beetle-caused tree mortality using single-date and multi-date Landsat imagery. *Remote Sensing of Environment,* 132, 49-58.

Meigs, G.W., Kennedy, R.E., Cohen, W.B. 2011a. A Landsat time series approach to characterize bark beetle and defoliator impacts on tree mortality and surface fuels in conifer forests. *Remote Sensing of Environment,* 115, 3707-3718.

Meigs, G.W., Turner, D.P., Ritts, W.D., Yang, Z.Q., Law, B.E. 2011b. Landscape-Scale Simulation of Heterogeneous Fire Effects on Pyrogenic Carbon Emissions, Tree Mortality, and Net Ecosystem Production. *Ecosystems,* 14, 758-775.

Melaas, E.K., Sulla-Menashe, D., Gray, J.M., Black, T.A., Morin, T.H., Richardson, A.D., Friedl, M.A. 2016. Multisite analysis of land surface phenology in North American temperate and boreal deciduous forests from Landsat. *Remote Sensing of Environment,* 186, 452-464.

Meroni, M., Rossini, M., Picchi, V., Panigada, C., Cogliati, S., Nali, C., Colombo, R. 2008. Assessing steady-state fluorescence and PRI from hyperspectral proximal sensing as early indicators of plant stress: The case of ozone exposure. *Sensors,* 8, 1740-1754.

Messinger, M., Asner, G.P., Silman, M. 2016. Rapid assessments of Amazon forest structure and biomass using small unmanned aerial systems. *Remote Sensing,* 8(8), 615; https://doi.org/10.3390/rs8080615.

Miao, G.F., Guan, K.Y., Yang, X., Bernacchi, C.J., Berry, J.A., DeLucia, E.H., Wu, J., Moore, C.E., Meacham, K., Cai, Y.P., Peng, B., Kimm, H., Masters, M.D. 2018. Sun-induced chlorophyll fluorescence, photosynthesis, and light use efficiency of a soybean field from seasonally continuous measurements. *Journal of Geophysical Research-Biogeosciences,* 123, 610-623.

Middleton, E.M., Cheng, Y.B., Hilker, T., Black, T.A., Krishnan, P., Coops, N.C., Huemmrich, K.F. 2009. Linking foliage spectral responses to canopy-level ecosystem photosynthetic light-use efficiency at a Douglas-fir forest in Canada. *Canadian Journal of Remote Sensing,* 35, 166-188.

Middleton, E.M., Huemmrich, K.F., Landis, D.R., Black, T.A., Barr, A.G., McCaughey, J.H. 2016. Photosynthetic efficiency of northern forest ecosystems using a MODIS-derived Photochemical Reflectance Index (PRI). *Remote Sensing of Environment,* 187, 345-366.

Middleton, E.M., K.F. Huemmrich, Q. Zhang, P.K.E. Campbell, and D.R. Landis (2018). Spectral bio-indicators of photosynthetic efficiency and vegetation stress, In, Hyperspectral Remote Sensing of Vegetation (Second Edition, 4 Volume set), Chapter 5, Biophysical and Biochemical Characterization and Plant Species Studies, Editors: P.S. Thenkabail, J.G. Lyon, and A. Huete, Taylor & Francis; Vol 3: 133-179.

Migliavacca, M., Perez-Priego, O., Rossini, M., El-Madany, T.S., Moreno, G., van der Tol, C., Rascher, U., Berninger, A., Bessenbacher, V., Burkart, A., Carrara, A., Fava, F., Guan, J.H., Hammer, T.W., Henkel, K., Juarez-Alcalde, E., Julitta, T., Kolle, O., Martin, M.P., Musavi, T., Pacheco-Labrador, J., Perez-Burgueno, A., Wutzler, T., Zaehle, S.,

2871 Reichstein, M. 2017. Plant functional traits and canopy structure control the relationship
2872 between photosynthetic CO2 uptake and far-red sun-induced fluorescence in a
2873 Mediterranean grassland under different nutrient availability. *New Phytologist,* 214,
2874 1078-1091.
2875 Mildrexler, D.J., Zhao, M.S., Heinsch, F.A., Running, S.W. 2007. A new satellite-based
2876 methodology for continental-scale disturbance detection. *Ecological Applications,* 17,
2877 235-250.
2878 Minh, D.H.T., Le Toan, T., Rocca, F., Tebaldini, S., Villard, L., Rejou-Mechain, M., Phillips,
2879 O.L., Feldpausch, T.R., Dubois-Fernandez, P., Scipal, K., Chave, J. 2016. SAR
2880 tomography for the retrieval of forest biomass and height: Cross-validation at two
2881 tropical forest sites in French Guiana. *Remote Sensing of Environment,* 175, 138-147.
2882 Minu, S., Shetty, A., Minasny, B., Gomez, C. 2017. The role of atmospheric correction
2883 algorithms in the prediction of soil organic carbon from Hyperion data. *International*
2884 *Journal of Remote Sensing,* 38, 6435-6456.
2885 Mishra, U., Lal, R., Liu, D.S., Van Meirvenne, M. 2010. Predicting the spatial variation of the
2886 soil organic carbon pool at a regional scale. *Soil Science Society of America Journal,* 74,
2887 906-914.
2888 Mohammed, G.H., Colombo, R., Middleton, E.M., Rascher, U., van der Tol, C., Nedbal, L.,
2889 Goulas, Y., Pérez-Priego, O., Damm, A., Meroni, M., Joiner, J., Cogliati, S., Verhoef, W.,
2890 Gastellu-Etchegorry, J.-P., Malenovský, Z., Miller, J.R., Guanter, L., Moreno, J., Moya,
2891 I., Frankenberg, C., Zarco-Tejada, P.J. (2019). Remote sensing of solar-induced
2892 chlorophyll fluorescence (SIF) in vegetation: 50 years of progress, *Remote Sensing of*
2893 *Environment*, 231, https://doi.org/10.1016/j.rse.2019.04.030.
2894 Monteith, J.L. 1972. Solar-radiation and productivity in tropical ecosystems. *Journal of Applied*
2895 *Ecology,* 9, 747-766.
2896 Monteith, J.L., Unsworth, M.H. (1990). *Principles of Environmental Physics*. 2nd ed. Antony
2897 Rowe Ltd., Eastbourne, U.K.
2898 Moore, D.J.P., Trahan, N.A., Wilkes, P., Quaife, T., Stephens, B.B., Elder, K., Desai, A.R.,
2899 Negron, J., Monson, R.K. 2013. Persistent reduced ecosystem respiration after insect
2900 disturbance in high elevation forests. *Ecology Letters,* 16, 731-737.
2901 Moran, M.S., Ponce-Campos, G.E., Huete, A., McClaran, M.P., Zhang, Y.G., Hamerlynck, E.P.,
2902 Augustine, D.J., Gunter, S.A., Kitchen, S.G., Peters, D.P.C., Starks, P.J., Hernandez, M.
2903 2014. Functional response of U.S. grasslands to the early 21st-century drought. *Ecology,*
2904 95, 2121-2133.
2905 Myneni, R.B., Dong, J., Tucker, C.J., Kaufmann, R.K., Kauppi, P.E., Liski, J., Zhou, L.,
2906 Alexeyev, V., Hughes, M.K. 2001. A large carbon sink in the woody biomass of
2907 Northern forests. *Proceedings of the National Academy of Sciences of the United States*
2908 *of America,* 98, 14784-14789.
2909 Myneni, R.B., Hoffman, S., Knyazikhin, Y., Privette, J.L., Glassy, J., Tian, Y., Wang, Y., Song,
2910 X., Zhang, Y., Smith, G.R., Lotsch, A., Friedl, M., Morisette, J.T., Votava, P., Nemani,
2911 R.R., Running, S.W. 2002. Global products of vegetation leaf area and fraction absorbed
2912 PAR from year one of MODIS data. *Remote Sensing of Environment,* 83, 214-231.
2913 Myneni, R.B., Keeling, C.D., Tucker, C.J., Asrar, G., Nemani, R.R. 1997a. Increased plant
2914 growth in the northern high latitudes from 1981 to 1991. *Nature,* 386, 698-702.

Myneni, R.B., Nemani, R.R., Running, S.W. 1997b. Estimation of global leaf area index and absorbed par using radiative transfer models. *IEEE Transactions on Geoscience and Remote Sensing,* 35, 1380-1393.

Myneni, R.B., Williams, D.L. 1994. On the relationship between FAPAR and NDVI. *Remote Sensing of Environment,* 49, 200-211.

Naesset, E., Gobakken, T. 2008. Estimation of above- and below-ground biomass across regions of the boreal forest zone using airborne laser. *Remote Sensing of Environment,* 112, 3079-3090.

Nassar, R., Jones, D.B.A., Kulawik, S.S., Worden, J.R., Bowman, K.W., Andres, R.J., Suntharalingam, P., Chen, J.M., Brenninkmeijer, C.A.M., Schuck, T.J., Conway, T.J., Worthy, D.E. 2011. Inverse modeling of CO2 sources and sinks using satellite observations of CO2 from TES and surface flask measurements. *Atmospheric Chemistry and Physics,* 11, 6029-6047.

Nemani, R.R., Keeling, C.D., Hashimoto, H., Jolly, W.M., Piper, S.C., Tucker, C.J., Myneni, R.B., Running, S.W. 2003. Climate-driven increases in global terrestrial net primary production from 1982 to 1999. *Science,* 300, 1560-1563.

Ni, W., Sun, G., Zhang, Z., Yu, H. (2016). Retrieval of forest aboveground biomass through the synergy of X-band (TeraSAR-X/TandDEM-X) and L-band (PALSAR-2) InSAR data. In, *2016 IEEE International Geoscience and Remote Sensing Symposium (IGARSS)* (pp. 5304-5306)

Ni, W.J., Zhang, Z.Y., Sun, G.Q., Liu, Q.H. 2018. Modeling interferometric SAR features of forest canopies over mountainous area at landscape scales. *IEEE Transactions on Geoscience and Remote Sensing,* 56, 2958-2967.

Nie, D., Kanemasu, E.T., Fritschen, L.J., Weaver, H.L., Smith, E.A., Verma, S.B., Field, R.T., Kustas, W.P., Stewart, J.B. 1992. An intercomparison of surface-energy flux measurement systems used during FIFE 1987. *Journal of Geophysical Research-Atmospheres,* 97, 18715-18724.

Nobre, C.A., Wickland, D., Kabat, P.I. (2001). Large Scale Biosphere-Atmosphere Experiment in Amazonia (LBA). In, *Global Change Newsletter* (pp. 2-4)

Odum, E.P. 1969. Strategy of ecosystem development. *Science,* 164, 262-270.

Ollinger, S.V., Richardson, A.D., Martin, M.E., Hollinger, D.Y., Frolking, S.E., Reich, P.B., Plourde, L.C., Katul, G.G., Munger, J.W., Oren, R., Smithb, M.L., U, K.T.P., Bolstad, P.V., Cook, B.D., Day, M.C., Martin, T.A., Monson, R.K., Schmid, H.P. 2008. Canopy nitrogen, carbon assimilation, and albedo in temperate and boreal forests: Functional relations and potential climate feedbacks. *Proceedings of the National Academy of Sciences of the United States of America,* 105, 19336-19341.

Palace, M., Keller, M., Asner, G.P., Hagen, S., Braswell, B. 2008. Amazon forest structure from IKONOS satellite data and the automated characterization of forest canopy properties. *Biotropica,* 40, 141-150.

Pan, Y., Chen, J.M., Birdsey, R., McCullough, K., He, L., Deng, F. 2011. Age structure and disturbance legacy of North American forests. *Biogeosciences,* 8, 715-732.

Pandit, S., Tsuyuki, S., Dube, T. 2018. Estimating above-ground biomass in sub-tropical buffer zone community forests, Nepal, using Sentinel 2 data. *Remote Sensing,* 10(4), 601; https://doi.org/10.3390/rs10040601.

Pang, Y., Lefsky, M., Andersen, H.E., Miller, M.E., Sherrill, K. 2008. Validation of the ICEsat vegetation product using crown-area-weighted mean height derived using crown

delineation with discrete return lidar data. *Canadian Journal of Remote Sensing,* 34, S471-S484.

Pang, Y., Li, Z.-Y. 2012. Inversion of biomass components of the temperate forest using airborne Lidar technology in Xiaoxing'an Mountains, Northeastern of China. *Chinese Journal of Plant Ecology,* 36, 1095-1105.

Pang, Y., Li, Z.Y., Ju, H.B., Lu, H., Jia, W., Si, L., Guo, Y., Liu, Q.W., Li, S.M., Liu, L.X., Xie, B.B., Tan, B.X., Dian, Y.Y. 2016. LiCHy: The CAF's LiDAR, CCD and hyperspectral integrated airborne observation system. *Remote Sensing,* 8, 398; doi:10.3390/rs8050398.

Papale, D., Black, T.A., Carvalhais, N., Cescatti, A., Chen, J.Q., Jung, M., Kiely, G., Lasslop, G., Mahecha, M.D., Margolis, H., Merbold, L., Montagnani, L., Moors, E., Olesen, J.E., Reichstein, M., Tramontana, G., van Gorsel, E., Wohlfahrt, G., Raduly, B. 2015. Effect of spatial sampling from European flux towers for estimating carbon and water fluxes with artificial neural networks. *Journal of Geophysical Research-Biogeosciences,* 120, 1941-1957.

Papale, D., Valentini, A. 2003. A new assessment of European forests carbon exchanges by eddy fluxes and artificial neural network spatialization. *Global Change Biology,* 9, 525-535.

Parazoo, N.C., Bowman, K., Fisher, J.B., Frankenberg, C., Jones, D.B.A., Cescatti, A., Perez-Priego, O., Wohlfahrt, G., Montagnani, L. 2014. Terrestrial gross primary production inferred from satellite fluorescence and vegetation models. *Global Change Biology,* 20, 3103-3121.

Parazoo, N.C., Bowman, K., Frankenberg, C., Lee, J.E., Fisher, J.B., Worden, J., Jones, D.B.A., Berry, J., Collatz, G.J., Baker, I.T., Jung, M., Liu, J.J., Osterman, G., O'Dell, C., Sparks, A., Butz, A., Guerlet, S., Yoshida, Y., Chen, H.L., Gerbig, C. 2013. Interpreting seasonal changes in the carbon balance of southern Amazonia using measurements of XCO2 and chlorophyll fluorescence from GOSAT. *Geophysical Research Letters,* 40, 2829-2833.

Pastor, J., Aber, J.D., Melillo, J.M. 1984. Biomass prediction using generalized allometric regressions for some Northeast tree species. *Forest Ecology and Management,* 7, 265-274.

Pedelty, J., Devadiga, S., Masuoka, E., Brown, M., Pinzon, J., Tucker, C., Roy, D., Ju, J.C., Vermote, E., Prince, S., Nagol, J., Justice, C., Schaaf, C., Liu, J.C., Privette, J., Pinheiro, A., Ieee (2007). Generating a Long-term Land Data Record from the AVHRR and MODIS instruments. *Igarss: 2007 IEEE International Geoscience and Remote Sensing Symposium, Vols 1-12: Sensing and Understanding Our Planet* (pp. 1021-1024). New York: Ieee.

Peylin, P., Bacour, C., MacBean, N., Leonard, S., Rayner, P., Kuppel, S., Koffi, E., Kane, A., Maignan, F., Chevallier, F., Ciais, P., Prunet, P. 2016. A new stepwise carbon cycle data assimilation system using multiple data streams to constrain the simulated land surface carbon cycle. *Geoscientific Model Development,* 9, 3321-3346.

Peylin, P., Law, R.M., Gurney, K.R., Chevallier, F., Jacobson, A.R., Maki, T., Niwa, Y., Patra, P.K., Peters, W., Rayner, P.J., Rodenbeck, C., van der Laan-Luijkx, I.T., Zhang, X. 2013. Global atmospheric carbon budget: results from an ensemble of atmospheric CO2 inversions. *Biogeosciences,* 10, 6699-6720.

Pinty, B., Janssens-Maenhout, G., Dowell, M., Zunker, H., Brunhes, T., Ciais, P., Dee, D., Denier van der Gon, H., Dolman, H., Drinkwater, M., Engelen, R., Heimann, M., Holmlund, K., Husband, R., Kentarchos, A., Meijer, Y., Palmer, P., Scholze, M. (2017). An Operational Anthropogenic CO_2 Emissions Monitoring Verification Support capacity

- Baseline Requirements. Model Components and Functional Architecture. In E.E. European Commission Joint Research Centre (Ed.)
Pinzon, J.E., Tucker, C.J. 2014. A non-stationary 1981-2012 AVHRR NDVI3g time series. *Remote Sensing,* 6, 6929-6960.
Ploton, P., Barbier, N., Couteron, P., Antin, C.M., Ayyappan, N., Balachandran, N., Barathan, N., Bastin, J.F., Chuyong, G., Dauby, G., Droissart, V., Gastellu-Etchegorry, J.P., Kamdem, N.G., Kenfack, D., Libalah, M., Mofack, G., Momo, S.T., Pargal, S., Petronelli, P., Proisy, C., Rejou-Mechain, M., Sonke, B., Texier, N., Thomas, D., Verley, P., Dongmo, D.Z., Berger, U., Pelissier, R. 2017. Toward a general tropical forest biomass prediction model from very high resolution optical satellite images. *Remote Sensing of Environment,* 200, 140-153.
Polonsky, I.N., O'Brien, D.M., Kumer, J.B., O'Dell, C.W., Geo, C.T. 2014. Performance of a geostationary mission, geoCARB, to measure CO2, CH4 and CO column-averaged concentrations. *Atmospheric Measurement Techniques,* 7, 959-981.
Ponce-Campos, G.E., Moran, M.S., Huete, A., Zhang, Y.G., Bresloff, C., Huxman, T.E., Eamus, D., Bosch, D.D., Buda, A.R., Gunter, S.A., Scalley, T.H., Kitchen, S.G., McClaran, M.P., McNab, W.H., Montoya, D.S., Morgan, J.A., Peters, D.P.C., Sadler, E.J., Seyfried, M.S., Starks, P.J. 2013. Ecosystem resilience despite large-scale altered hydroclimatic conditions. *Nature,* 494, 349-352.
Popescu, S.C. 2007. Estimating biomass of individual pine trees using airborne lidar. *Biomass & Bioenergy,* 31, 646-655.
Popescu, S.C., Zhou, T., Nelson, R., Neuenschwande, A., Sheridan, R., Narine, L., Walsh, K.M. 2018. Photon counting LiDAR: An adaptive ground and canopy height retrieval algorithm for ICESat-2 data. *Remote Sensing of Environment,* 208, 154-170.
Porcar-Castell, A., Tyystjarvi, E., Atherton, J., van der Tol, C., Flexas, J., Pfundel, E.E., Moreno, J., Frankenberg, C., Berry, J.A. 2014. Linking chlorophyll a fluorescence to photosynthesis for remote sensing applications: mechanisms and challenges. *Journal of Experimental Botany,* 65, 4065-4095.
Potter, C.S., Randerson, J.T., Field, C.B., Matson, P.A., Vitousek, P.M., Mooney, H.A., Klooster, S.A. 1993. Terrestrial ecosystem production: A process model based on global satellite and surface data. *Global Biogeochemical Cycles,* 7, 811-841.
Powell, S.L., Cohen, W.B., Healey, S.P., Kennedy, R.E., Moisen, G.G., Pierce, K.B., Ohmann, J.L. 2010. Quantification of live aboveground forest biomass dynamics with Landsat time-series and field inventory data: A comparison of empirical modeling approaches. *Remote Sensing of Environment,* 114, 1053-1068.
Price, B., Gomez, A., Mathys, L., Gardi, O., Schellenberger, A., Ginzler, C., Thurig, E. 2017. Tree biomass in the Swiss landscape: nationwide modelling for improved accounting for forest and non-forest trees. *Environmental Monitoring and Assessment,* 189: 106, DOI 10.1007/s10661-017-5816-7.
Pulliainen, J.T., Mikkela, P.J., Hallikainen, M.T., Ikonen, J.P. 1996. Seasonal dynamics of C-band backscatter of boreal forests with applications to biomass and soil moisture estimation. *IEEE Transactions on Geoscience and Remote Sensing,* 34, 758-770.
Qi, W.L., Dubayah, R.O. 2016. Combining Tandem-X InSAR and simulated GEDI lidar observations for forest structure mapping. *Remote Sensing of Environment,* 187, 253-266.

Quaife, T., Quegan, S., Disney, M., Lewis, P., Lomas, M., Woodward, F.I. 2008. Impact of land cover uncertainties on estimates of biospheric carbon fluxes. *Global Biogeochemical Cycles,* 22, GB4016, doi:10.1029/2007GB003097.

Quegan, S., Toan, L.T., Chave, J., Dall, J., Exbrayat, J.F., Minh, D.H.T., Lomas, M., D'Alessandro, M.M., Paillou, P., Papathanassiou, K., Rocca, F., Saatchi, S., Scipal, K., Shugart, H., Smallman, T.L., Soja, M.J., Tebaldini, S., Ulander, L., Villard, L., Williams, M. 2019. The European Space Agency BIOMASS mission: Measuring forest above-ground biomass from space. *Remote Sensing of Environment,* 227, 44-60.

Raczka, B.M., Davis, K.J., Huntzinger, D., Neilson, R.P., Poulter, B., Richardson, A.D., Xiao, J.F., Baker, I., Ciais, P., Keenan, T.F., Law, B., Post, W.M., Ricciuto, D., Schaefer, K., Tian, H.Q., Tomelleri, E., Verbeeck, H., Viovy, N. 2013. Evaluation of continental carbon cycle simulations with North American flux tower observations. *Ecological Monographs,* 83, 531-556.

Rahman, A.F., Sims, D.A., Cordova, V.D., El-Masri, B.Z. 2005. Potential of MODIS EVI and surface temperature for directly estimating per-pixel ecosystem C fluxes. *Geophysical Research Letters,* 32, L19404, doi:10.1029/2005GL024127.

Rahman, M.Z., Abu Bakar, M.A., Razak, K.A., Rasib, A., Kanniah, K.D., Kadir, W.H.W., Omar, H., Faidi, A., Kassim, A., Latif, Z. 2017. Non-destructive, laser-based individual tree aboveground biomass estimation in a tropical rainforest. *Forests,* 8(3), 86; https://doi.org/10.3390/f8030086.

Raich, J.W., Schlesinger, W.H. 1992. The global carbon-dioxide flux in soil respiration and its relationship to vegetation and climate. *Tellus Series B-Chemical and Physical Meteorology,* 44, 81-99.

Randerson, J.T., Hoffman, F.M., Thornton, P.E., Mahowald, N.M., Lindsay, K., Lee, Y.H., Nevison, C.D., Doney, S.C., Bonan, G., Stockli, R., Covey, C., Running, S.W., Fung, I.Y. 2009. Systematic assessment of terrestrial biogeochemistry in coupled climate-carbon models. *Global Change Biology,* 15, 2462-2484.

Ranson, K.J., Sun, G. 2000. Effects of environmental conditions on boreal forest classification and biomass estimates with SAR. *IEEE Transactions on Geoscience and Remote Sensing,* 38, 1242-1252.

Ranson, K.J., Sun, G., Weishampel, J.F., Knox, R.G. 1997. Forest biomass from combined ecosystem and radar backscatter modeling. *Remote Sensing of Environment,* 59, 118-133.

Rascher, U., Agati, G., Alonso, L., Cecchi, G., Champagne, S., Colombo, R., Damm, A., Daumard, F., de Miguel, E., Fernandez, G., Franch, B., Franke, J., Gerbig, C., Gioli, B., Gomez, J.A., Goulas, Y., Guanter, L., Gutierrez-de-la-Camara, O., Hamdi, K., Hostert, P., Jimenez, M., Kosvancova, M., Lognoli, D., Meroni, M., Miglietta, F., Moersch, A., Moreno, J., Moya, I., Neininger, B., Okujeni, A., Ounis, A., Palombi, L., Raimondi, V., Schickling, A., Sobrino, J.A., Stellmes, M., Toci, G., Toscano, P., Udelhoven, T., van der Linden, S., Zaldei, A. 2009. CEFLES2: the remote sensing component to quantify photosynthetic efficiency from the leaf to the region by measuring sun-induced fluorescence in the oxygen absorption bands. *Biogeosciences,* 6, 1181-1198.

Rascher, U., Alonso, L., Burkart, A., Cilia, C., Cogliati, S., Colombo, R., Damm, A., Drusch, M., Guanter, L., Hanus, J., Hyvarinen, T., Julitta, T., Jussila, J., Kataja, K., Kokkalis, P., Kraft, S., Kraska, T., Matveeva, M., Moreno, J., Muller, O., Panigada, C., Pikl, M., Pinto, F., Prey, L., Pude, R., Rossini, M., Schickling, A., Schurr, U., Schuttemeyer, D., Verrelst,

J., Zemek, F. 2015. Sun-induced fluorescence - a new probe of photosynthesis: First maps from the imaging spectrometer HyPlant. *Global Change Biology,* 21, 4673-4684.
Rasmussen, M.O., Gottsche, F.M., Diop, D., Mbow, C., Olesen, F.S., Fensholt, R., Sandholt, I. 2011. Tree survey and allometric models for tiger bush in northern Senegal and comparison with tree parameters derived from high resolution satellite data. *International Journal of Applied Earth Observation and Geoinformation,* 13, 517-527.
Ratnayakea, R.R., Karunaratneb, S.B., Lesselsc, J.S., Yogenthirand, N., Rajapakshaa, R.P.S.K., Gnanavelrajahd, N. 2016. Digital soil mapping of organic carbon concentration in paddy growing soils of Northern Sri Lanka. *Geoderma Regional,* 7, 167-176.
Rayner, P.J., O'Brien, D.M. 2001. The utility of remotely sensed CO2 concentration data in surface source inversions. *Geophysical Research Letters,* 28, 175-178.
Restrepo-Coupe, N., Huete, A., Davies, K., Cleverly, J., Beringer, J., Eamus, D., van Gorsel, E., Hutley, L.B., Meyer, W.S. 2016. MODIS vegetation products as proxies of photosynthetic potential along a gradient of meteorologically and biologically driven ecosystem productivity. *Biogeosciences,* 13, 5587-5608.
Reuter, M., Buchwitz, M., Hilker, M., Heymann, J., Bovensmann, H., Burrrrows, J.P., Houweling, S., Liu, Y.Y., Nassar, R., Chevallier, F., Ciais, P., Marshall, J., Reichstein, M. 2017. How much CO2 is taken up by the European terrestrial biosphere? *Bulletin of the American Meteorological Society,* 98, 665-671.
Reuter, M., Buchwitz, M., Hilker, M., Heymann, J., Schneising, O., Pillai, D., Bovensmann, H., Burrows, J.P., Bosch, H., Parker, R., Butz, A., Hasekamp, O., O'Dell, C.W., Yoshida, Y., Gerbig, C., Nehrkorn, T., Deutscher, N.M., Warneke, T., Notholt, J., Hase, F., Kivi, R., Sussmann, R., Machida, T., Matsueda, H., Sawa, Y. 2014. Satellite-inferred European carbon sink larger than expected. *Atmospheric Chemistry and Physics,* 14, 13739-13753.
Richardson, A.D., Hufkens, K., Milliman, T., Frolking, S. 2018. Intercomparison of phenological transition dates derived from the PhenoCam Dataset V1.0 and MOD.IS satellite remote sensing. *Scientific Reports,* 8:5679 | DOI:10.1038/s41598-018-23804-6
Richardson, A.J., Wiegand, C.L. 1977. Distinguishing vegetation from soil background information. *Photogrammetric Engineering and Remote Sensing,* 43, 1541-1552.
Rignot, E., Way, J.B., Williams, C., Viereck, L. 1994. Radar estimates of aboveground biomass in boreal forests of interior Alaska. *IEEE Transactions on Geoscience and Remote Sensing,* 32, 1117-1124.
Romero, J.M., Cordon, G.B., Lagorio, M.G. 2018. Modeling re-absorption of fluorescence from the leaf to the canopy level. *Remote Sensing of Environment,* 204, 138-146.
Rosen, P., Hensley, S., Shaffer, S., Edelstein, W., Kim, Y., Kumar, R., Misra, T., Bhan, R., Satish, R., Sagi, R., Ieee (2016). AN UPDATE ON THE NASA-ISRO DUAL-FREQUENCY DBF SAR (NISAR) MISSION. *2016 IEEE International Geoscience and Remote Sensing Symposium* (pp. 2106-2108). New York: Ieee.
Rosen, P.A., Hensley, S., Joughin, I.R., Li, F.K., Madsen, S.N., Rodriguez, E., Goldstein, R.M. 2000. Synthetic aperture radar interferometry. *Proceedings of the IEEE,* 88, 333-382.
Rossel, R.A.V., Hicks, W.S. 2015. Soil organic carbon and its fractions estimated by visible-near infrared transfer functions. *European Journal of Soil Science,* 66, 438-450.
Rossel, R.A.V., Walvoort, D.J.J., McBratney, A.B., Janik, L.J., Skjemstad, J.O. 2006. Visible, near infrared, mid infrared or combined diffuse reflectance spectroscopy for simultaneous assessment of various soil properties. *Geoderma,* 131, 59-75.

Rossini, M., Nedbal, L., Guanter, L., Ac, A., Alonso, L., Burkart, A., Cogliati, S., Colombo, R., Damm, A., Drusch, M., Hanus, J., Janoutova, R., Julitta, T., Kokkalis, P., Moreno, J., Novotny, J., Panigada, C., Pinto, F., Schickling, A., Schuttemeyer, D., Zemek, F., Rascher, U. 2015. Red and far red Sun-induced chlorophyll fluorescence as a measure of plant photosynthesis. *Geophysical Research Letters,* 42, 1632-1639.

Roughgarden, J., Running, S.W., Matson, P.A. 1991. What does remote sensing do for ecology? *Ecology,* 72, 1918-1922.

Rouse, J.W., Haas, R.H., Schell, J.A., Deering, D.W. (1974). Monitoring vegetation systems in the Great Plains with ERTS. In, *Paper presented at the 3rd ERTS-1 Symposium, Greenbelt, Maryland.*

Roy, P.S., Ravan, S.A. 1996. Biomass estimation using satellite remote sensing data - An investigation on possible approaches for natural forest. *Journal of Biosciences,* 21, 535-561.

Ruimy, A., Jarvis, P., Baldocchi, D., Saugier, B. 1995. CO_2 fluxes over plant canopies and solar radiation: A review. *Advances in Ecological Research,* 26, 1-68.

Running, S.W., Nemani, R.R., Heinsch, F.A., Zhao, M.S., Reeves, M., Hashimoto, H. 2004. A continuous satellite-derived measure of global terrestrial primary production. *Bioscience,* 54, 547-560.

Ryu, Y., Baldocchi, D.D., Kobayashi, H., van Ingen, C., Li, J., Black, T.A., Beringer, J., van Gorsel, E., Knohl, A., Law, B.E., Roupsard, O. 2011. Integration of MODIS land and atmosphere products with a coupled-process model to estimate gross primary productivity and evapotranspiration from 1 km to global scales. *Global Biogeochemical Cycles,* 25, GB4017,doi:10.1029/2011GB004053.

Ryu, Y., Berry, J.A., Baldocchi, D.D. 2019. What is global photosynthesis? History, uncertainties and opportunities. *Remote Sensing of Environment,* 223, 95-114.

Saatchi, S., Yu, Y., Fore, A., Nuemann, M., Chapman, B., Nguyen, M., Nemani, R., Ganguly, S., Zhang, G., Votava, P., Masek, J., Tucker, C., Hall, F., Nelson, R., Cook, B., Birdsey, R., Healey, S., Johnson, K., Dubayah, R., Lefsky, M. (2012). CMS US Forest Biomass Map. In. https://nacp-files.nacarbon.org/biomass_pilot/JPL_ARC_Maps/Continental_US/.

Saatchi, S.S., Harris, N.L., Brown, S., Lefsky, M., Mitchard, E.T.A., Salas, W., Zutta, B.R., Buermann, W., Lewis, S.L., Hagen, S., Petrova, S., White, L., Silman, M., Morel, A. 2011. Benchmark map of forest carbon stocks in tropical regions across three continents. *Proceedings of the National Academy of Sciences of the United States of America,* 108, 9899-9904.

Saatchi, S.S., Houghton, R.A., Alvala, R., Soares, J.V., Yu, Y. 2007. Distribution of aboveground live biomass in the Amazon basin. *Global Change Biology,* 13, 816-837.

Saleska, S.R., Wu, J., Guan, K.Y., Araujo, A.C., Huete, A., Nobre, A.D., Restrepo-Coupe, N. 2016. Dry-season greening of Amazon forests. *Nature,* 531, E4-E5.

Santoro, M., Askne, J., Smith, G., Fransson, J.E. 2002. Stem volume retrieval in boreal forests from ERS-1/2 interferometry. *Remote Sensing of Environment,* 81, 19-35.

Santoro, M., Shvidenko, A., McCallum, I., Askne, J., Schmullius, C. 2007. Properties of ERS-1/2 coherence in the Siberian boreal forest and implications for stem volume retrieval. *Remote Sensing of Environment,* 106, 154-172.

Sarker, L.R., Nichol, J.E. 2011. Improved forest biomass estimates using ALOS AVNIR-2 texture indices. *Remote Sensing of Environment,* 115, 968-977.

Sasai, T., Ichii, K., Yamaguchi, Y., Nemani, R. 2005. Simulating terrestrial carbon fluxes using the new biosphere model "biosphere model integrating eco-physiological and mechanistic approaches using satellite data" (BEAMS). *Journal of Geophysical Research-Biogeosciences,* 110, G02014, doi:10.1029/2005JG000045.

Schanda, E. 1985. A Radargrammetry Experiment in a Mountain Region. *International Journal of Remote Sensing,* 6, 1113-1124.

Schillaci, C., Acutis, M., Lombardo, L., Lipani, A., Fantappie, M., Marker, M., Saia, S. 2017. Spatio-temporal topsoil organic carbon mapping of a semi-arid Mediterranean region: The role of land use, soil texture, topographic indices and the influence of remote sensing data to modelling. *Science of the Total Environment,* 601, 821-832.

Schimel, D., Pavlick, R., Fisher, J.B., Asner, G.P., Saatchi, S., Townsend, P., Miller, C., Frankenberg, C., Hibbard, K., Cox, P. 2015. Observing terrestrial ecosystems and the carbon cycle from space. *Global Change Biology,* 21, 1762-1776.

Schimel, D.S. 1995. Terrestrial ecosystems and the carbon cycle. *Global Change Biology,* 1, 77-91.

Scholze, M., Buchwitz, M., Dorigo, W., Guanter, L., Shaun, Q.G. 2017. Reviews and syntheses: Systematic Earth observations for use in terrestrial carbon cycle data assimilation systems. *Biogeosciences,* 14, 3401-3429.

Schubert, P., Eklundh, L., Lund, M., Nilsson, M. 2010. Estimating northern peatland CO2 exchange from MODIS time series data. *Remote Sensing of Environment,* 114, 1178-1189.

Schwalm, C.R., Williams, C.A., Schaefer, K., Baldocchi, D., Black, T.A., Goldstein, A.H., Law, B.E., Oechel, W.C., Kyaw, T.P.U., Scott, R.L. 2012. Reduction in carbon uptake during turn of the century drought in western North America. *Nature Geoscience,* 5, 551-556.

Selige, T., Bohner, J., Schmidhalter, U. 2006. High resolution topsoil mapping using hyperspectral image and field data in multivariate regression modeling procedures. *Geoderma,* 136, 235-244.

Sellers, P., Hall, F., Margolis, H., Kelly, B., Baldocchi, D., Denhartog, G., Cihlar, J., Ryan, M.G., Goodison, B., Crill, P., Ranson, K.J., Lettenmaier, D., Wickland, D.E. 1995. The boreal ecosystem-atmosphere study (BOREAS) – an overview and early results from the 1994 field year. *Bulletin of the American Meteorological Society,* 76, 1549-1577.

Sellers, P.J. 1985. Canopy reflectance, photosynthesis and transpiration. *International Journal of Remote Sensing,* 6, 1335-1372.

Sellers, P.J., Hall, F.G., Asrar, G., Strebel, D.E., Murphy, R.E. 1988. The first ISLSCP Field Experiment (FIFE). *Bulletin of the American Meteorological Society,* 69, 22-27.

Sellers, P.J., Randall, D.A., Collatz, G.J., Berry, J.A., Field, C.B., Dazlich, D.A., Zhang, C., Collelo, G.D., Bounoua, L. 1996. A revised land surface parameterization (SiB2) for atmospheric GCMs .1. Model formulation. *Journal of Climate,* 9, 676-705.

Senf, C., Seidl, R., Hostert, P. 2017. Remote sensing of forest insect disturbances: Current state and future directions. *International Journal of Applied Earth Observation and Geoinformation,* 60, 49-60.

Shepherd, K.D., Walsh, M.G. 2002. Development of reflectance spectral libraries for characterization of soil properties. *Soil Science Society of America Journal,* 66, 988-998.

Shi, J.C., Du, Y., Du, J.Y., Jiang, L.M., Chai, L.N., Mao, K.B., Xu, P., Ni, W.J., Xiong, C., Liu, Q., Liu, C.Z., Guo, P., Cui, Q., Li, Y.Q., Chen, J., Wang, A.Q., Luo, H.J., Wang, Y.H.

2012. Progresses on microwave remote sensing of land surface parameters. *Science China-Earth Sciences,* 55, 1052-1078.

Shi, Z., Wang, Q.L., Peng, J., Ji, W.J., Liu, H.J., Li, X., Viscarra Rossel, R.A. 2014. Development of a national VNIR soil-spectral library for soil classification and prediction of organic matter concentrations. *Science China-Earth Sciences,* 57, 1671-1680.

Shoshany, M., Karnibad, L. 2011. Mapping shrubland biomass along Mediterranean climatic gradients: The synergy of rainfall-based and NDVI-based models. *International Journal of Remote Sensing,* 32, 9497-9508.

Sibanda, M., Mutanga, O., Rouget, M. 2015. Examining the potential of Sentinel-2 MSI spectral resolution in quantifying above ground biomass across different fertilizer treatments. *ISPRS Journal of Photogrammetry and Remote Sensing,* 110, 55-65.

Sibanda, M., Mutanga, O., Rouget, M., Kumar, L. 2017. Estimating biomass of native grass grown under complex management treatments using WorldView-3 spectral derivatives. *Remote Sensing,* 9(1), 55; https://doi.org/10.3390/rs9010055.

Simard, M., Pinto, N., Fisher, J.B., Baccini, A. 2011. Mapping forest canopy height globally with spaceborne lidar. *Journal of Geophysical Research-Biogeosciences,* 116, G04021, doi:10.1029/2011JG001708.

Sims, D.A., Rahman, A.F., Cordova, V.D., El-Masri, B.Z., Baldocchi, D.D., Bolstad, P.V., Flanagan, L.B., Goldstein, A.H., Hollinger, D.Y., Misson, L., Monson, R.K., Oechel, W.C., Schmid, H.P., Wofsy, S.C., Xu, L. 2008. A new model of gross primary productivity for North American ecosystems based solely on the enhanced vegetation index and land surface temperature from MODIS. *Remote Sensing of Environment,* 112, 1633-1646.

Sitch, S., Smith, B., Prentice, I.C., Arneth, A., Bondeau, A., Cramer, W., Kaplan, J.O., Levis, S., Lucht, W., Sykes, M.T., Thonicke, K., Venevsky, S. 2003. Evaluation of ecosystem dynamics, plant geography and terrestrial carbon cycling in the LPJ dynamic global vegetation model. *Global Change Biology,* 9, 161-185.

Sjostrom, M., Ardo, J., Arneth, A., Boulain, N., Cappelaere, B., Eklundh, L., de Grandcourt, A., Kutsch, W.L., Merbold, L., Nouvellon, Y., Scholes, R.J., Schubert, P., Seaquist, J., Veenendaal, E.M. 2011. Exploring the potential of MODIS EVI for modeling gross primary production across African ecosystems. *Remote Sensing of Environment,* 115, 1081-1089.

Smith, M.L., Ollinger, S.V., Martin, M.E., Aber, J.D., Hallett, R.A., Goodale, C.L. 2002. Direct estimation of aboveground forest productivity through hyperspectral remote sensing of canopy nitrogen. *Ecological Applications,* 12, 1286-1302.

Smith, W.K., Biederman, J.A., Scott, R.L., Moore, D.J.P., He, M., Kimball, J.S., Yan, D., Hudson, A., Barnes, M.L., MacBean, N., Fox, A.M., Litvak, M.E. 2018. Chlorophyll fluorescence better captures seasonal and interannual gross primary productivity dynamics across dryland ecosystems of southwestern North America. *Geophysical Research Letters,* 45, 748-757.

Smith, W.K., Reed, S.C., Cleveland, C.C., Ballantyne, A.P., Anderegg, W.R.L., Wieder, W.R., Liu, Y.Y., Running, S.W. 2016. Large divergence of satellite and Earth system model estimates of global terrestrial CO2 fertilization. *Nature Climate Change,* 6, 306-310.

Soenen, S.A., Peddle, D.R., Hall, R.J., Coburn, C.A., Hall, F.G. 2010. Estimating aboveground forest biomass from canopy reflectance model inversion in mountainous terrain. *Remote Sensing of Environment,* 114, 1325-1337.

Somarathna, P.D.S.N., Malone, B.P., Minasny, B. 2016. Mapping soil organic carbon content over New South Wales, Australia using local regression kriging. *Geoderma Regional,* 7, 38-48.

Song, L., Guanter, L., Guan, K.Y., You, L.Z., Huete, A., Ju, W.M., Zhang, Y.G. 2018. Satellite sun-induced chlorophyll fluorescence detects early response of winter wheat to heat stress in the Indian Indo-Gangetic Plains. *Global Change Biology,* 24, 4023-4037.

Stavros, E.N., Schimel, D., Pavlick, R., Serbin, S., Swann, A., Duncanson, L., Fisher, J.B., Fassnacht, F., Ustin, S., Dubayah, R., Schweiger, A., Wennberg, P. 2017. ISS observations offer insights into plant function. *Nature Ecology & Evolution,* 1, 0194, DOI: 10.1038/s41559-017-0194.

Stefano, P., Angelo, P., Simone, P., Filomena, R., Federico, S., Tiziana, S., Umberto, A., Vincenzo, C., Raffaele, C., Roberto, D.B., Giovanni, L., Acito, N., Marco, D., Stefania, M., Giovalmi, C., Cristina, A., Ieee (2013). The PRISMA hyperspectral mission: science activities and opportunities for agriculture and land monitoring. *2013 Ieee International Geoscience and Remote Sensing Symposium* (pp. 4558-4561). New York: Ieee.

Stevens, A., Udelhoven, T., Denis, A., Tychon, B., Lioy, R., Hoffmann, L., van Wesemael, B. 2010. Measuring soil organic carbon in croplands at regional scale using airborne imaging spectroscopy. *Geoderma,* 158, 32-45.

Stocker, B.D., Zscheischler, J., Keenan, T.F., Prentice, I.C., Penuelas, J., Seneviratne, S.I. 2018. Quantifying soil moisture impacts on light use efficiency across biomes. *New Phytologist,* 218, 1430-1449.

Stockli, R., Rutishauser, T., Dragoni, D., O'Keefe, J., Thornton, P.E., Jolly, M., Lu, L., Denning, A.S. 2008. Remote sensing data assimilation for a prognostic phenology model. *Journal of Geophysical Research-Biogeosciences,* 113, G04021, doi:10.1029/2008JG000781.

Stone, T.A., Houghton, R.A., Melillo, J.M., Woodwell, G.M. 1983. Deforestation in the Amazon basin measured by satellite – a release of CO2 to the atmosphere. *Biological Bulletin,* 165, 511-511.

Stovall, A.E.L., Vorster, A.G., Anderson, R.S., Evangelista, P.H., Shugart, H.H. 2017. Non-destructive aboveground biomass estimation of coniferous trees using terrestrial LiDAR. *Remote Sensing of Environment,* 200, 31-42.

Stuffler, T., Kaufmann, C., Hofer, S., Forster, K.P., Schreier, G., Mueller, A., Eckardt, A., Bach, H., Penne, B., Benz, U., Haydn, R. 2007. The EnMAP hyperspectral imager- An advanced optical payload for future applications in Earth observation programmes. *Acta Astronautica,* 61, 115-120.

Sturrock, R.N., Frankel, S.J., Brown, A.V., Hennon, P.E., Kliejunas, J.T., Lewis, K.J., Worrall, J.J., Woods, A.J. 2011. Climate change and forest diseases. *Plant Pathology,* 60, 133-149.

Sun, G., Ranson, K.J., Kharuk, V.I. 2002. Radiometric slope correction for forest biomass estimation from SAR data in the Western Sayani Mountains, Siberia. *Remote Sensing of Environment,* 79, 279-287.

Sun, G.Q., Ranson, K.J., Guo, Z., Zhang, Z., Montesano, P., Kimes, D. 2011. Forest biomass mapping from lidar and radar synergies. *Remote Sensing of Environment, 115*, 2906-2916.

Sun, Y., Frankenberg, C., Jung, M., Joiner, J., Guanter, L., Kohler, P., Magney, T. 2018. Overview of Solar-Induced chlorophyll Fluorescence (SIF) from the Orbiting Carbon

Observatory-2: Retrieval, cross-mission comparison, and global monitoring for GPP. *Remote Sensing of Environment,* 209, 808-823.

Sun, Y., Frankenberg, C., Wood, J.D., Schimel, D.S., Jung, M., Guanter, L., Drewry, D.T., Verma, M., Porcar-Castell, A., Griffis, T.J., Gu, L., Magney, T.S., Kohler, P., Evans, B., Yuen, K. 2017. OCO-2 advances photosynthesis observation from space via solar-induced chlorophyll fluorescence. *Science,* 358, eaam5747, DOI: 10.1126/science.aam5747.

Sun, Y., Fu, R., Dickinson, R., Joiner, J., Frankenberg, C., Gu, L.H., Xia, Y.L., Fernando, N. 2015. Drought onset mechanisms revealed by satellite solar-induced chlorophyll fluorescence: Insights from two contrasting extreme events. *Journal of Geophysical Research-Biogeosciences,* 120, 2427-2440.

Tang, X.G., Liu, D.W., Song, K.S., Munger, J.W., Zhang, B., Wang, Z.M. 2011. A new model of net ecosystem carbon exchange for the deciduous-dominated forest by integrating MODIS and flux data. *Ecological Engineering,* 37, 1567-1571.

Tans, P.P. 1997. The CO2 lifetime concept should be banished - Comment. *Climatic Change,* 37, 487-490.

Tao, S.L., Guo, Q.H., Li, L., Xue, B.L., Kelly, M., Li, W.K., Xu, G.C., Su, Y.J. 2014. Airborne Lidar-derived volume metrics for aboveground biomass estimation: A comparative assessment for conifer stands. *Agricultural and Forest Meteorology,* 198, 24-32.

TerMikaelian, M.T., Korzukhin, M.D. 1997. Biomass equations for sixty-five North American tree species. *Forest Ecology and Management,* 97, 1-24.

Thum, T., Zaehle, S., Kohler, P., Aalto, T., Aurela, M., Guanter, L., Kolari, P., Laurila, T., Lohila, A., Magnani, F., Van der Tol, C., Markkanen, T. 2017. Modelling sun-induced fluorescence and photosynthesis with a land surface model at local and regional scales in northern Europe. *Biogeosciences,* 14, 1969-1987.

Tramontana, G., Jung, M., Schwalm, C.R., Ichii, K., Camps-Valls, G., Raduly, B., Reichstein, M., Arain, M.A., Cescatti, A., Kiely, G., Merbold, L., Serrano-Ortiz, P., Sickert, S., Wolf, S., Papale, D. 2016. Predicting carbon dioxide and energy fluxes across global FLUXNET sites with regression algorithms. *Biogeosciences,* 13, 4291-4313.

Tucker, C.J., Fung, I.Y., Keeling, C.D., Gammon, R.H. 1986. Relationship between atmospheric CO_2 variations and a satellite-derived vegetation index. *Nature,* 319, 195-199.

Tucker, C.J., Pinzon, J.E., Brown, M.E., Slayback, D.A., Pak, E.W., Mahoney, R., Vermote, E.F., El Saleous, N. 2005. An extended AVHRR 8-km NDVI dataset compatible with MODIS and SPOT vegetation NDVI data. *International Journal of Remote Sensing,* 26, 4485-4498.

Tucker, C.J., Slayback, D.A., Pinzon, J.E., Los, S.O., Myneni, R.B., Taylor, M.G. 2001. Higher northern latitude normalized difference vegetation index and growing season trends from 1982 to 1999. *International Journal of Biometeorology,* 45, 184-190.

Turner, D.P., Ollinger, S.V., Kimball, J.S. 2004. Integrating remote sensing and ecosystem process models for landscape- to regional-scale analysis of the carbon cycle. *Bioscience,* 54, 573-584.

Turner, D.P., Ritts, W.D., Cohen, W.B., Gower, S.T., Running, S.W., Zhao, M.S., Costa, M.H., Kirschbaum, A.A., Ham, J.M., Saleska, S.R., Ahl, D.E. 2006. Evaluation of MODIS NPP and GPP products across multiple biomes. *Remote Sensing of Environment,* 102, 282-292.

Turner, M.G., Hargrove, W.W., Gardner, R.H., Romme, W.H. 1994. Effects of fire on landscape heterogeneity in Yellowstone-National-Park, Wyoming. *Journal of Vegetation Science,* 5, 731-742.

van der Tol, C., Verhoef, W., Timmermans, J., Verhoef, A., Su, Z. 2009. An integrated model of soil-canopy spectral radiances, photosynthesis, fluorescence, temperature and energy balance. *Biogeosciences,* 6, 3109-3129.

van der Werf, G.R., Randerson, J.T., Giglio, L., van Leeuwen, T.T., Chen, Y., Rogers, B.M., Mu, M.Q., van Marle, M.J.E., Morton, D.C., Collatz, G.J., Yokelson, R.J., Kasibhatla, P.S. 2017. Global fire emissions estimates during 1997-2016. *Earth System Science Data,* 9, 697-720.

van Leeuwen, W.J.D., Orr, B.J., Marsh, S.E., Herrmann, S.M. 2006. Multi-sensor NDVI data continuity: Uncertainties and implications for vegetation monitoring applications. *Remote Sensing of Environment,* 100, 67-81.

van Mantgem, P.J., Stephenson, N.L., Byrne, J.C., Daniels, L.D., Franklin, J.F., Fule, P.Z., Harmon, M.E., Larson, A.J., Smith, J.M., Taylor, A.H., Veblen, T.T. 2009. Widespread increase of tree mortality rates in the western United States. *Science,* 323, 521-524.

Vastaranta, M., Holopainen, M., Karjalainen, M., Kankare, V., Hyyppa, J., Kaasalainen, S. 2014. TerraSAR-X stereo radargrammetry and airborne scanning LiDAR height metrics in imputation of forest aboveground biomass and stem volume. *IEEE Transactions on Geoscience and Remote Sensing,* 52, 1197-1204.

Vastaranta, M., Holopainen, M., Karjalainen, M., Kankare, V., Hyyppa, J., Kaasalainen, S., Hyyppa, H. 2012. SAR Radargrammetry and Scanning Lidar in Predicting Forest Canopy Height. *2012 IEEE International Geoscience and Remote Sensing Symposium*, 6515-6518.

Verma, M., Schimel, D., Evans, B., Frankenberg, C., Beringer, J., Drewry, D.T., Magney, T., Marang, I., Hutley, L., Moore, C., Eldering, A. 2017. Effect of environmental conditions on the relationship between solar-induced fluorescence and gross primary productivity at an OzFlux grassland site. *Journal of Geophysical Research-Biogeosciences,* 122, 716-733.

Veroustraete, F., Sabbe, H., Eerens, H. 2002. Estimation of carbon mass fluxes over Europe using the C-Fix model and Euroflux data. *Remote Sensing of Environment,* 83, 376-399.

Verrelst, J., Rivera, J.P., van der Tol, C., Magnani, F., Mohammed, G., Moreno, J. 2015. Global sensitivity analysis of the SCOPE model: What drives simulated canopy-leaving sun-induced fluorescence? *Remote Sensing of Environment,* 166, 8-21.

Walther, S., Voigt, M., Thum, T., Gonsamo, A., Zhang, Y.G., Kohler, P., Jung, M., Varlagin, A., Guanter, L. 2016. Satellite chlorophyll fluorescence measurements reveal large-scale decoupling of photosynthesis and greenness dynamics in boreal evergreen forests. *Global Change Biology,* 22, 2979-2996.

Wang, B., Waters, C., Orgill, S., Gray, J., Cowie, A., Clark, A., Liu, D.L. 2018. High resolution mapping of soil organic carbon stocks using remote sensing variables in the semi-arid rangelands of eastern Australia. *Science of the Total Environment,* 630, 367-378.

Wang, D.L., Xin, X.P., Shao, Q.Q., Brolly, M., Zhu, Z.L., Chen, J. 2017. Modeling aboveground biomass in Hulunber grassland ecosystem by using unmanned aerial vehicle discrete lidar. *Sensors,* 17, 180; doi:10.3390/s17010180.

Wang, J., Rich, P.M., Price, K.P., Kettle, W.D. 2004. Relations between NDVI and tree productivity in the central Great Plains. *International Journal of Remote Sensing,* 25, 3127-3138.

Wang, X.F., Xiao, J.F., Li, X., Cheng, G.D., Ma, M.G., Zhu, G.F., Arain, M.A., Black, T.A., Jassal, R.S. 2019. No trends in spring and autumn phenology during the global warming hiatus. *Nature Communications,* 10:2389, https://doi.org/10.1038/s41467-019-10235-8.

Wehr, R., Munger, J.W., McManus, J.B., Nelson, D.D., Zahniser, M.S., Davidson, E.A., Wofsy, S.C., Saleska, S.R. 2016. Seasonality of temperate forest photosynthesis and daytime respiration. *Nature,* 534, 680-+.

Were, K., Bui, D.T., Dick, O.B., Singh, B.R. 2015. A comparative assessment of support vector regression, artificial neural networks, and random forests for predicting and mapping soil organic carbon stocks across an Afromontane landscape. *Ecological Indicators,* 52, 394-403.

Wilcox, C.H., Frazier, B.E., Ball, S.T. 1994. Relationship between soil organic carbon and Landsat TM data in eastern Washington. *Photogrammetric Engineering and Remote Sensing,* 60, 777-781.

Wilson, B.T., Woodall, C.W., Griffith, D.M. 2013. Imputing forest carbon stock estimates from inventory plots to a nationally continuous coverage. *Carbon Balance and Management,* 8:1, http://www.cbmjournal.com/content/8/1/1.

Wirth, C., Schumacher, J., Schulze, E.D. 2004. Generic biomass functions for Norway spruce in Central Europe - a meta-analysis approach toward prediction and uncertainty estimation. *Tree Physiology, 24*, 121-139.

WMO/IAEA (2016). 18th WMO/ IAEA Meeting on Carbon Dioxide, Other Greenhouse Gases and Related Measurement Techniques (GGMT-2015). 13-17 September 2015; La Jolla, CA, USA.

Wofsy, S.C., Goulden, M.L., Munger, J.W., Fan, S.M., Bakwin, P.S., Daube, B.C., Bassow, S.L., Bazzaz, F.A. 1993. Net exchange of CO_2 in a midlatitude forest. *Science,* 260, 1314-1317.

Wohlfahrt, G., Gerdel, K., Migliavacca, M., Rotenberg, E., Tatarinov, F., Muller, J., Hammerle, A., Julitta, T., Spielmann, F.M., Yakir, D. 2018. Sun-induced fluorescence and gross primary productivity during a heat wave. *Scientific Reports,* 8:14169, DOI:10.1038/s41598-018-32602-z.

Wolanin, A., Rozanov, V.V., Dinter, T., Noel, S., Vountas, M., Burrows, J.P., Bracher, A. 2015. Global retrieval of marine and terrestrial chlorophyll fluorescence at its red peak using hyperspectral top of atmosphere radiance measurements: Feasibility study and first results. *Remote Sensing of Environment,* 166, 243-261.

Wood, J.D., Griffis, T.J., Baker, J.M., Frankenberg, C., Verma, M., Yuen, K. 2017. Multiscale analyses of solar-induced florescence and gross primary production. *Geophysical Research Letters,* 44, 533-541.

Woodcock, C.E., Allen, R., Anderson, M., Belward, A., Bindschadler, R., Cohen, W., Gao, F., Goward, S.N., Helder, D., Helmer, E., Nemani, R., Oreopoulos, L., Schott, J., Thenkabail, P.S., Vermote, E.F., Vogelmann, J., Wulder, M.A., Wynne, R., Landsat Sci, T. 2008. Free access to Landsat imagery. *Science,* 320, 1011-1011.

Wu, C.Y., Gaumont-Guay, D., Black, T.A., Jassal, R.S., Xu, S.G., Chen, J.M., Gonsamo, A. 2014. Soil respiration mapped by exclusively use of MODIS data for forest landscapes of Saskatchewan, Canada. *ISPRS Journal of Photogrammetry and Remote Sensing,* 94, 80-90.

Wu, J., van Aardt, J.A.N., Asner, G.P., Mathieu, R., Kennedy-Bowdoin, T., Knapp, D., Wessels, K., Erasmus, B.F.N., Smit, I., Ieee (2009). Connecting the dots between laser waveforms and herbaceous biomass for assessment of land degradation using small-footprint waveform LiDAR data. *2009 IEEE International Geoscience and Remote Sensing Symposium, Vols 1-5* (pp. 585-+). New York: Ieee.

Wu, Y.C., Strahler, A.H. 1994. Remote estimation of crown size, stand density, and biomass on the Oregon transect. *Ecological Applications,* 4, 299-312.

Wulder, M.A., Masek, J.G., Cohen, W.B., Loveland, T.R., Woodcock, C.E. 2012. Opening the archive: How free data has enabled the science and monitoring promise of Landsat. *Remote Sensing of Environment,* 122, 2-10.

Wulder, M.A., White, J.C., Loveland, T.R., Woodcock, C.E., Belward, A.S., Cohen, W.B., Fosnight, E.A., Shaw, J., Masek, J.G., Roy, D.P. 2016. The global Landsat archive: Status, consolidation, and direction. *Remote Sensing of Environment,* 185, 271-283.

Wunch, D., Toon, G.C., Wennberg, P.O., Wofsy, S.C., Stephens, B.B., Fischer, M.L., Uchino, O., Abshire, J.B., Bernath, P., Biraud, S.C., Blavier, J.F.L., Boone, C., Bowman, K.P., Browell, E.V., Campos, T., Connor, B.J., Daube, B.C., Deutscher, N.M., Diao, M., Elkins, J.W., Gerbig, C., Gottlieb, E., Griffith, D.W.T., Hurst, D.F., Jimenez, R., Keppel-Aleks, G., Kort, E.A., Macatangay, R., Machida, T., Matsueda, H., Moore, F., Morino, I., Park, S., Robinson, J., Roehl, C.M., Sawa, Y., Sherlock, V., Sweeney, C., Tanaka, T., Zondlo, M.A. 2010. Calibration of the total carbon column observing network using aircraft profile data. *Atmospheric Measurement Techniques,* 3, 1351-1362.

Wunch, D., Wennberg, P.O., Toon, G.C., Connor, B.J., Fisher, B., Osterman, G.B., Frankenberg, C., Mandrake, L., O'Dell, C., Ahonen, P., Biraud, S.C., Castano, R., Cressie, N., Crisp, D., Deutscher, N.M., Eldering, A., Fisher, M.L., Griffith, D.W.T., Gunson, M., Heikkinen, P., Keppel-Aleks, G., Kyro, E., Lindenmaier, R., Macatangay, R., Mendonca, J., Messerschmidt, J., Miller, C.E., Morino, I., Notholt, J., Oyafuso, F.A., Rettinger, M., Robinson, J., Roehl, C.M., Salawitch, R.J., Sherlock, V., Strong, K., Sussmann, R., Tanaka, T., Thompson, D.R., Uchino, O., Warneke, T., Wofsy, S.C. 2011. A method for evaluating bias in global measurements of CO2 total columns from space. *Atmospheric Chemistry and Physics,* 11, 12317-12337.

Wylie, B.K., Johnson, D.A., Laca, E., Saliendra, N.Z., Gilmanov, T.G., Reed, B.C., Tieszen, L.L., Worstell, B.B. 2003. Calibration of remotely sensed, coarse resolution NDVI to CO2 fluxes in a sagebrush-steppe ecosystem. *Remote Sensing of Environment,* 85, 243-255.

Xiao, J., Moody, A. 2005. Geographical distribution of global greening trends and their climatic correlates: 1982-1998. *International Journal of Remote Sensing, 26*, 2371-2390.

Xiao, J.F. 2014. Satellite evidence for significant biophysical consequences of the "Grain for Green" Program on the Loess Plateau in China. *Journal of Geophysical Research-Biogeosciences,* 119, 2261-2275.

Xiao, J.F., Chen, J.Q., Davis, K.J., Reichstein, M. 2012. Advances in upscaling of eddy covariance measurements of carbon and water fluxes. *Journal of Geophysical Research-Biogeosciences,* 117, G00J01, doi:10.1029/2011JG001889.

Xiao, J.F., Zhuang, Q.L., Law, B.E., Baldocchi, D.D., Chen, J.Q., Richardson, A.D., Melillo, J.M., Davis, K.J., Hollinger, D.Y., Wharton, S., Oren, R., Noormets, A., Fischer, M.L., Verma, S.B., Cook, D.R., Sun, G., McNulty, S., Wofsy, S.C., Bolstad, P.V., Burns, S.P., Curtis, P.S., Drake, B.G., Falk, M., Foster, D.R., Gu, L.H., Hadley, J.L., Katulk, G.G.,

Litvak, M., Ma, S.Y., Martinz, T.A., Matamala, R., Meyers, T.P., Monson, R.K., Munger, J.W., Oechel, W.C., Paw U, K.T., Schmid, H.P., Scott, R.L., Starr, G., Suyker, A.E., Torn, M.S. 2011b. Assessing net ecosystem carbon exchange of U.S. terrestrial ecosystems by integrating eddy covariance flux measurements and satellite observations. *Agricultural and Forest Meteorology,* 151, 60-69.

Xiao, J.F., Davis, K.J., Urban, N.M., Keller, K., Saliendra, N.Z. 2011a. Upscaling carbon fluxes from towers to the regional scale: Influence of parameter variability and land cover representation on regional flux estimates. *Journal of Geophysical Research-Biogeosciences,* 116, G00J06, doi:10.1029/2010JG001568.

Xiao, J.F., Moody, A. 2004. Photosynthetic activity of US biomes: responses to the spatial variability and seasonality of precipitation and temperature. *Global Change Biology,* 10, 437-451.

Xiao, J.F., Ollinger, S.V., Frolking, S., Hurtt, G.C., Hollinger, D.Y., Davis, K.J., Pan, Y.D., Zhang, X.Y., Deng, F., Chen, J.Q., Baldocchi, D.D., Law, B.E., Arain, M.A., Desai, A.R., Richardson, A.D., Sun, G., Amiro, B., Margolis, H., Gu, L.H., Scott, R.L., Blanken, P.D., Suyker, A.E. 2014a. Data-driven diagnostics of terrestrial carbon dynamics over North America. *Agricultural and Forest Meteorology,* 197, 142-157.

Xiao, J.F., Davis, K.J., Urban, N.M., Keller, K. 2014b. Uncertainty in model parameters and regional carbon fluxes: A model-data fusion approach. *Agricultural and Forest Meteorology,* 189, 175-186.

Xiao, J.F., Sun, G., Chen, J.Q., Chen, H., Chen, S.P., Dong, G., Gao, S.H., Guo, H.Q., Guo, J.X., Han, S.J., Kato, T., Li, Y.L., Lin, G.H., Lu, W.Z., Ma, M.G., McNulty, S., Shao, C.L., Wang, X.F., Xie, X., Zhang, X.D., Zhang, Z.Q., Zhao, B., Zhou, G.S., Zhou, J. 2013. Carbon fluxes, evapotranspiration, and water use efficiency of terrestrial ecosystems in China. *Agricultural and Forest Meteorology,* 182-183, 76-90.

Xiao, J.F., Zhou, Y., Zhang, L. 2015. Contributions of natural and human factors to increases in vegetation productivity in China. *Ecosphere,* 6(11):233. http://dx.doi.org/10.1890/ES14-00394.1.

Xiao, J.F., Zhuang, Q.L., Baldocchi, D.D., Law, B.E., Richardson, A.D., Chen, J.Q., Oren, R., Starr, G., Noormets, A., Ma, S.Y., Verma, S.B., Wharton, S., Wofsy, S.C., Bolstad, P.V., Burns, S.P., Cook, D.R., Curtis, P.S., Drake, B.G., Falk, M., Fischer, M.L., Foster, D.R., Gu, L.H., Hadley, J.L., Hollinger, D.Y., Katul, G.G., Litvak, M., Martin, T.A., Matamala, R., McNulty, S., Meyers, T.P., Monson, R.K., Munger, J.W., Oechel, W.C., Paw U, K.T., Schmid, H.P., Scott, R.L., Sun, G., Suyker, A.E., Torn, M.S. 2008. Estimation of net ecosystem carbon exchange for the conterminous United States by combining MODIS and AmeriFlux data. *Agricultural and Forest Meteorology,* 148, 1827-1847.

Xiao, J.F., Zhuang, Q.L., Law, B.E., Chen, J.Q., Baldocchi, D.D., Cook, D.R., Oren, R., Richardson, A.D., Wharton, S., Ma, S.Y., Martin, T.A., Verma, S.B., Suyker, A.E., Scott, R.L., Monson, R.K., Litvak, M., Hollinger, D.Y., Sun, G., Davis, K.J., Bolstad, P.V., Burns, S.P., Curtis, P.S., Drake, B.G., Falk, M., Fischer, M.L., Foster, D.R., Gu, L.H., Hadley, J.L., Katul, G.G., Roser, Y., McNulty, S., Meyers, T.P., Munger, J.W., Noormets, A., Oechel, W.C., Paw, K.T., Schmid, H.P., Starr, G., Torn, M.S., Wofsy, S.C. 2010. A continuous measure of gross primary production for the conterminous United States derived from MODIS and AmeriFlux data. *Remote Sensing of Environment,* 114, 576-591.

Xiao, X.M., Hollinger, D., Aber, J., Goltz, M., Davidson, E.A., Zhang, Q.Y., Moore, B. 2004. Satellite-based modeling of gross primary production in an evergreen needleleaf forest. *Remote Sensing of Environment,* 89, 519-534.

Xiao, Z.Q., Liang, S.L., Sun, R., Wang, J.D., Jiang, B. 2015. Estimating the fraction of absorbed photosynthetically active radiation from the MODIS data based GLASS leaf area index product. *Remote Sensing of Environment,* 171, 105-117.

Yang, F.H., Ichii, K., White, M.A., Hashimoto, H., Michaelis, A.R., Votava, P., Zhu, A.X., Huete, A., Running, S.W., Nemani, R.R. 2007. Developing a continental-scale measure of gross primary production by combining MODIS and AmeriFlux data through Support Vector Machine approach. *Remote Sensing of Environment,* 110, 109-122.

Yang, H.L., Yang, X., Zhang, Y.G., Heskel, M.A., Lu, X.L., Munger, J.W., Sun, S.C., Tang, J.W. 2017. Chlorophyll fluorescence tracks seasonal variations of photosynthesis from leaf to canopy in a temperate forest. *Global Change Biology,* 23, 2874-2886.

Yang, K., Ryu, Y., Dechant, B., Berry, J.A., Hwang, Y., Jiang, C., Kang, M., Min, J., Kimm, H., Kornfeld, A., Yang, X. 2018. Sun-induced chlorophyll fluorescence is more strongly related to absorbed light than to photosynthesis at half-hourly resolution in a rice paddy. *Remote Sensing of Environment,* 216, 658-673.

Yang, P.Q., van der Tol, C. 2018. Linking canopy scattering of far-red sun-induced chlorophyll fluorescence with reflectance. *Remote Sensing of Environment, 209*, 456-467.

Yang, R.M., Rossiter, D.G., Liu, F., Lu, Y.Y., Yang, F., Yang, F., Zhao, Y.G., Li, D.C., Zhang, G.L. 2015a. Predictive mapping of topsoil organic arbon in an alpine environment aided by Landsat TM. *Plos One,* 10(10): e0139042.doi:10.1371/journal.pone.0139042.

Yang, X., Tang, J.W., Mustard, J.F., Lee, J.E., Rossini, M., Joiner, J., Munger, J.W., Kornfeld, A., Richardson, A.D. 2015b. Solar-induced chlorophyll fluorescence that correlates with canopy photosynthesis on diurnal and seasonal scales in a temperate deciduous forest. *Geophysical Research Letters,* 42, 2977-2987.

Yoshida, Y., Joiner, J., Tucker, C., Berry, J., Lee, J.E., Walker, G., Reichle, R., Koster, R., Lyapustin, A., Wang, Y. 2015. The 2010 Russian drought impact on satellite measurements of solar-induced chlorophyll fluorescence: Insights from modeling and comparisons with parameters derived from satellite reflectances. *Remote Sensing of Environment,* 166, 163-177.

Yu, Y.F., Saatchi, S. 2016. Sensitivity of L-band SAR backscatter to aboveground biomass of global forests. *Remote Sensing,* 8(6), 522; https://doi.org/10.3390/rs8060522.

Yuan, W.P., Liu, S., Zhou, G.S., Zhou, G.Y., Tieszen, L.L., Baldocchi, D., Bernhofer, C., Gholz, H., Goldstein, A.H., Goulden, M.L., Hollinger, D.Y., Hu, Y., Law, B.E., Stoy, P.C., Vesala, T., Wofsy, S.C., AmeriFlux, C. 2007. Deriving a light use efficiency model from eddy covariance flux data for predicting daily gross primary production across biomes. *Agricultural and Forest Meteorology,* 143, 189-207.

Yuan, W.P., Liu, S.G., Dong, W.J., Liang, S.L., Zhao, S.Q., Chen, J.M., Xu, W.F., Li, X.L., Barr, A., Black, T.A., Yan, W.D., Goulden, M.L., Kulmala, L., Lindroth, A., Margolis, H.A., Matsuura, Y., Moors, E., van der Molen, M., Ohta, T., Pilegaard, K., Varlagin, A., Vesala, T. 2014. Differentiating moss from higher plants is critical in studying the carbon cycle of the boreal biome. *Nature Communications,* 5:4270, DOI: 10.1038/ncomms5270.

Zarco-Tejada, P.J., Morales, A., Testi, L., Villalobos, F.J. 2013. Spatio-temporal patterns of chlorophyll fluorescence and physiological and structural indices acquired from

hyperspectral imagery as compared with carbon fluxes measured with eddy covariance. *Remote Sensing of Environment,* 133, 102-115.

Zhang, C.H., Ju, W.M., Chen, J.M., Li, D.Q., Wang, X.Q., Fan, W.Y., Li, M.S., Zan, M. 2014a. Mapping forest stand age in China using remotely sensed forest height and observation data. *Journal of Geophysical Research-Biogeosciences,* 119, 1163-1179.

Zhang, L., Wylie, B., Loveland, T., Fosnight, E., Tieszen, L.L., Ji, L., Gilmanov, T. 2007. Evaluation and comparison of gross primary production estimates for the Northern Great Plains grasslands. *Remote Sensing of Environment,* 106, 173-189.

Zhang, Q.Y., Cheng, Y.B., Lyapustin, A.I., Wang, Y.J., Gao, F., Suyker, A., Verma, S., Middleton, E.M. 2014b. Estimation of crop gross primary production (GPP): fAPAR(chl) versus MOD15A2 FPAR. *Remote Sensing of Environment,* 153, 1-6.

Zhang, X.T., Liang, S.L., Zhou, G.Q., Wu, H.R., Zhao, X. 2014c. Generating Global LAnd Surface Satellite incident shortwave radiation and photosynthetically active radiation products from multiple satellite data. *Remote Sensing of Environment,* 152, 318-332.

Zhang, X.Y., Kondragunta, S. 2006. Estimating forest biomass in the USA using generalized allometric models and MODIS land products. *Geophysical Research Letters,* 33, L09402,doi:10.1029/2006GL025879.

Zhang, X.Y., Liu, L.L., Liu, Y., Jayavelu, S., Wang, J.M., Moon, M., Henebry, G.M., Friedl, M.A., Schaaf, C.B. 2018a. Generation and evaluation of the VIIRS land surface phenology product. *Remote Sensing of Environment,* 216, 212-229.

Zhang, Y., Xiao, X.M., Zhang, Y.G., Wolf, S., Zhou, S., Joiner, J., Guanter, L., Verma, M., Sun, Y., Yang, X., Paul-Limoges, E., Gough, C.M., Wohlfahrt, G., Gioli, B., van der Tol, C., Nouvellon, Y., Lund, M., de Grandcourt, A. 2018b. On the relationship between sub-daily instantaneous and daily total gross primary production: Implications for interpreting satellite-based SIF retrievals. *Remote Sensing of Environment,* 205, 276-289.

Zhang, Y.G., Guanter, L., Berry, J.A., Joiner, J., van der Tol, C., Huete, A., Gitelson, A., Voigt, M., Kohler, P. 2014d. Estimation of vegetation photosynthetic capacity from space-based measurements of chlorophyll fluorescence for terrestrial biosphere models. *Global Change Biology,* 20, 3727-3742.

Zhang, Y.G., Guanter, L., Berry, J.A., van der Tol, C., Yang, X., Tang, J.W., Zhang, F.M. 2016. Model-based analysis of the relationship between sun-induced chlorophyll fluorescence and gross primary production for remote sensing applications. *Remote Sensing of Environment,* 187, 145-155.

Zhang, Z.Y., Ni, W.J., Sun, G.Q., Huang, W.L., Ranson, K.J., Cook, B.D., Guo, Z.F. 2017. Biomass retrieval from L-band polarimetric UAVSAR backscatter and PRISM stereo imagery. *Remote Sensing of Environment,* 194, 331-346.

Zhao, F., Huang, C.Q., Goward, S.N., Schleeweis, K., Rishmawi, K., Lindsey, M.A., Denning, E., Keddell, L., Cohen, W.B., Yang, Z.Q., Dungan, J.L., Michaelis, A. 2018a. Development of Landsat-based annual US forest disturbance history maps (1986-2010) in support of the North American Carbon Program (NACP). *Remote Sensing of Environment,* 209, 312-326.

Zhao, K.G., Popescu, S., Nelson, R. 2009. Lidar remote sensing of forest biomass: A scale-invariant estimation approach using airborne lasers. *Remote Sensing of Environment,* 113, 182-196.

Zhao, K.G., Suarez, J.C., Garcia, M., Hu, T.X., Wang, C., Londo, A. 2018b. Utility of multitemporal lidar for forest and carbon monitoring: Tree growth, biomass dynamics, and carbon flux. *Remote Sensing of Environment,* 204, 883-897.

Zhao, M., Running, S.W., Nemani, R.R. 2006. Sensitivity of Moderate Resolution Imaging Spectroradiometer (MODIS) terrestrial primary production to the accuracy of meteorological reanalyses. *Journal of Geophysical Research-Biogeosciences, 111*

Zhao, M.S., Heinsch, F.A., Nemani, R.R., Running, S.W. 2005. Improvements of the MODIS terrestrial gross and net primary production global data set. *Remote Sensing of Environment,* 95, 164-176.

Zheng, D.L., Rademacher, J., Chen, J.Q., Crow, T., Bresee, M., le Moine, J., Ryu, S.R. 2004. Estimating aboveground biomass using Landsat 7 ETM+ data across a managed landscape in northern Wisconsin, USA. *Remote Sensing of Environment,* 93, 402-411.

Zheng, Y., Zhang, L., Xiao, J., Yuan, W., Yan, M., Li, T., Zhang, Z. 2018. Sources of uncertainty in gross primary productivity simulated by light use efficiency models: Model structure, parameters, input data, and spatial resolution. *Agricultural and Forest Meteorology,* 263, 242-257.

Zhou, L.M., Tucker, C.J., Kaufmann, R.K., Slayback, D., Shabanov, N.V., Myneni, R.B. 2001. Variations in northern vegetation activity inferred from satellite data of vegetation index during 1981 to 1999. *Journal of Geophysical Research-Atmospheres,* 106, 20069-20083.

Zhou, Y.L., Wu, X.C., Ju, W.M., Chen, J.M., Wang, S.Q., Wang, H.M., Yuan, W.P., Black, T.A., Jassal, R., Ibrom, A., Han, S.J., Yan, J.H., Margolis, H., Roupsard, O., Li, Y.N., Zhao, F.H., Kiely, G., Starr, G., Pavelka, M., Montagnani, L., Wohlfahrt, G., D'Odorico, P., Cook, D., Arain, M.A., Bonal, D., Beringer, J., Blanken, P.D., Loubet, B., Leclerc, M.Y., Matteucci, G., Nagy, Z., Olejnik, J., U, K.T.P., Varlagin, A. 2016. Global parameterization and validation of a two-leaf light use efficiency model for predicting gross primary production across FLUXNET sites. *Journal of Geophysical Research-Biogeosciences,* 121, 1045-1072.

Zhu, Z.C., Bi, J., Pan, Y.Z., Ganguly, S., Anav, A., Xu, L., Samanta, A., Piao, S.L., Nemani, R.R., Myneni, R.B. 2013. Global data sets of vegetation leaf area index (LAI)3g and fraction of photosynthetically active radiation (FPAR)3g derived from Global Inventory Modeling and Mapping Studies (GIMMS) normalized difference vegetation index (NDVI3g) for the period 1981 to 2011. *Remote Sensing,* 5, 927-948.